An experimental approach to measure the temperature of in-flight particles in suspension plasma spraying

Bishoy Aziz

A Thesis

In

The Department of Mechanical and Industrial Engineering

Presented in Partial Fulfillment of the Requirement for the Degree of

Master of Applied Science in Mechanical Engineering

Concordia University Montreal, Quebec, Canada

Winter 2016

Concordia University

School of Graduate Studies

This is to certify that the thesis prepared

By: Bishoy Aziz

Entitled: An experimental approach to measure the temperature of in-flight particles in suspension plasma spraying

and submitted in partial fulfillment of the requirements for the degree of

Master of Applied Science in Mechanical Engineering

Complies with the regulations of the University and meets the accepted standards with respect to originality and quality.

Signed by the final examining committee:

Dr. Nadia Bhuiyan	Chair
Dr. Mojtaba Kahrizi	Examiner
Dr. Ali Dolatabadi	Examiner
Dr. Christian Moreau	Supervisor

Approved by Dr. Martin Pugh
Chair of Department or Graduate Program Director

Dr. Amir Asif
Dean of Faculty

Date April 14th, 2016

Abstract

An experimental approach to measure the temperature of in-flight particles in suspension plasma spraying

Bishoy Aziz

The temperature of in-flight particles in suspension plasma spraying (SPS) is one of the key parameters affecting the coating microstructure. Temperature measurement has been carried out before for in-flight particles in air plasma spray (APS) and other thermal spraying processes. Suspension plasma spray (SPS) is an emerging coating deposition technology that permits the deposition of nanostructured coatings with unique structural characteristics. The particles size in SPS is smaller than the one that is commonly used is APS and other spray processes leading to specific challenges for determining its temperature.

The aim of this work is to assess the feasibility of two-color pyrometer for in-flight particles in suspension plasma spraying. To do so, spectroscopic analysis in the visible to near infrared range was carried out on the jet stream when suspension of 20 wt. % YSZ particles in pure ethanol was sprayed. The analysis takes into account the radiation scattered by the particles (Mie scattering) as well as the radiation directly detected from the plasma in the jet stream, and it was found that the effect of the scattered radiation by the particles on temperature measurement is negligible along the center axis of spraying at the melting point of Zirconia.

Moreover, the main and dominant source of error on temperature measurement is the plasma radiation, the vapors and the free electrons in the background of the continuum. One the other hand, it was found that going for a longer wavelength from 1 µm to 2.5 µm is not a promising wavelength range for temperature measurement. Finally, the measurements carried out in this thesis favors future development for the current configuration of a commercial diagnostic sensor to have a better

precision for the value of temperature measurement, as it was found that the error because of the current configuration can reach 540 ° C degrees.

Acknowledgement

I am overwhelmed with gratitude to Prof. Christian Moreau for his outstanding mentorship to my research. Also, I am grateful to Dr. Fadhel Ben Ettouil for his support during the experimental work of this thesis. I am thankful to Prof. Ali Dolatabadi and all our group members for the cooperation during my residency in Concordia. Furthermore, I acknowledge the support of Photon Control for their supply with the required equipment. Finally, I am grateful to all my family members and my fiancée for their help and encouragement during my master's.

TABLE OF CONTENTS

LIST OF TABLES

LIST OF EQUATIONS

LIST OF FIGURES

Chapter 1

Introduction and background

1 INTRODUCTION AND BACKGROUND

Thermal spray processes are used to confer specific properties to specific parts and components in production by applying coatings to the surface of the part. Thermal spray is representing a global market of 10 billion USD (in 2014); 30% of this business is European based, and 50% of this market is operated on plasma spraying, also almost 90% is operated on DC plasma. Two main issues are becoming increasingly important nowadays. Firstly, the development of new processes to achieve specific coating characteristics. Secondly, the monitoring of processing to realize constant quality and reliability. Furthermore, in the case of new process development such as suspension based plasma spraying the characterization of the working gases and in-flight particles provides good understanding and supports optimization of these processes and reproducibility of coatings.

Plasma spray is a thermal spray process in which a non-transferred arc as a source of heat ionizes the plasma forming gases like Ar, Ar–H_2, Ar–He, Ar–He–H_2, N_2 and N_2. The created thermal plasma can reach a temperature higher than 8000º - 14000 º K at atmospheric pressure. Gas flow rates are between 0.8 and 2 g/s, and the mass of the secondary gas, generally helium or hydrogen, is generally negligible compared to that of the primary gas (argon or nitrogen).

Air plasma spray (APS) is considered the conventional method of spraying, where a dry powder is injected to the plasma volume radially or axially. The particles size distribution in APS process can vary from 10 to 100 µm. The process consists of generating an energetic gas flow (hot or cold gases) with an appropriate torch or gun generally flowing into the open-air environment, or sometimes into a controlled atmosphere. Thermal spray torches are devices for feeding, accelerating, heating and directing the flow of a thermal spray material toward the substrate.

The feedstock is introduced as powder. The powders are introduced into the jet of hot gases, and are accelerated but not necessarily melted before impacting on the substrate (depending on their

size and trajectories). The molten particles are deposited on the substrate forming splats that spread into a disk-like shape, and building up the coating. In APS, solid particles in the size of 10 – 100 µm produce lamellar structure with a diameter of few tens to two hundreds micrometers in diameter with a thickness of 1 to 10 µm. The deposited coatings by the conventional plasma spraying techniques contain numerous defects such as the macro - micro cracks, pores and poor contact with the surface area with the piled splats. Figure 1-1 illustrates APS process.

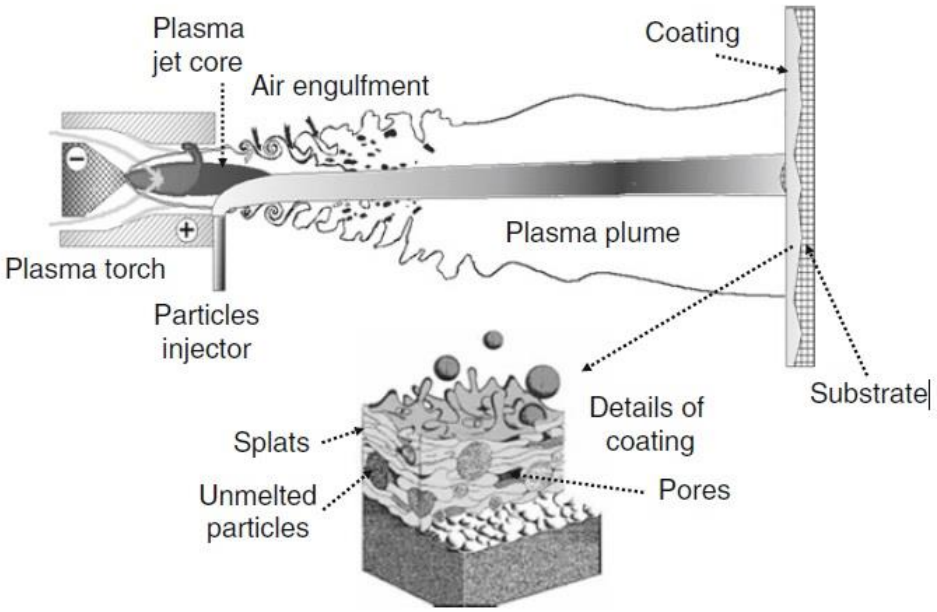

Figure 1-1: A schematic illustrates air plasma spray process (APS). [1]1

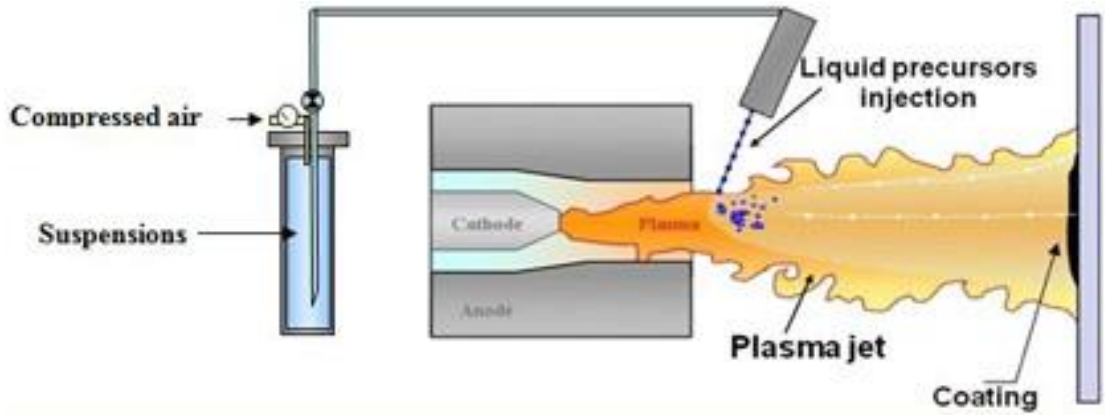

Figure 1-2: A schematic of suspension plasma spraying application (SPS).[2]

Suspension plasma spray (SPS) is a trending coating deposition technique that permits to produce nanostructured coatings with unique characteristics. The possible applications of suspension based plasma spraying are mainly in the field of energy conversion systems and aerospace, such as: [3]

1- Thermal barrier coatings TBCs.
2- Solid oxide fuel cells SOFCs.
3- Photo catalytic coatings.
4- Bio-active coatings.
5- Wear and corrosion resistant coatings.

In SPS, the sprayed material or powder is introduced to the plasma jet suspended in a liquid (water, ethanol, or a mix) because of their small size distribution. The liquid is injected radially relative to the axis of the plasma jet. The suspended powder in the carrier gas is injected into the jet axially or radially depending on the torch design via carrier gas. The particles of the powder are melted and propelled by the jet to impact on the substrate and form the coating. [4] The suspension goes through several consecutive steps as illustrated in Figure 1-2, 3. The first one is atomization to the liquid to form droplets of the injected suspension; the nanostructured coatings obtained with the suspension was probably also due to the second fragmentation or atomization of the injected droplets by the high-velocity plasma flow.

The fragmentation is named ‘bag break-up’: it corresponds to the deformation of the drop as a bag-like structure that is stretched and swept off in the flow direction. Those fine solids are then agglomerated and sintered to impact on the substrate. Those drops are deposited on a substrate creating splats that stick to the surface. The accumulation of several splats forms the required coating. Figure 1-3 shows the evolution of suspension droplet in the higher temperature flame. [1]

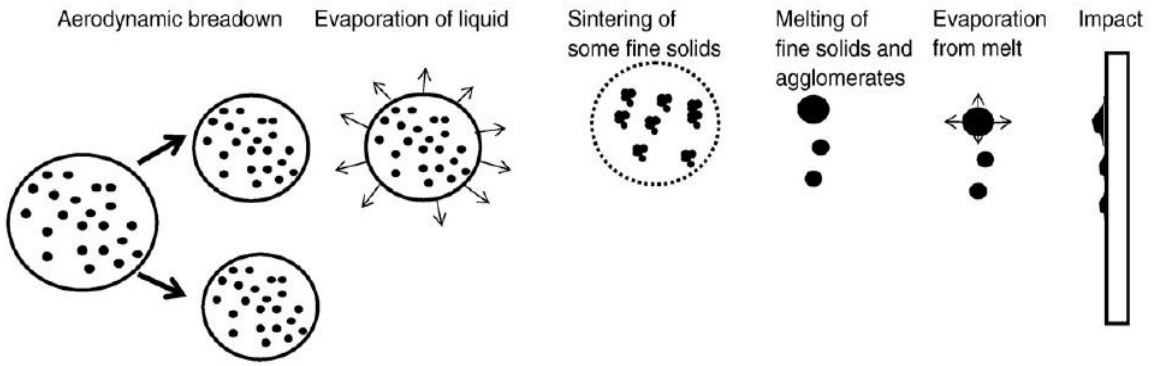

Figure 1-3: Evolution of a suspension droplet in the high temperature plasma or flame. [1]

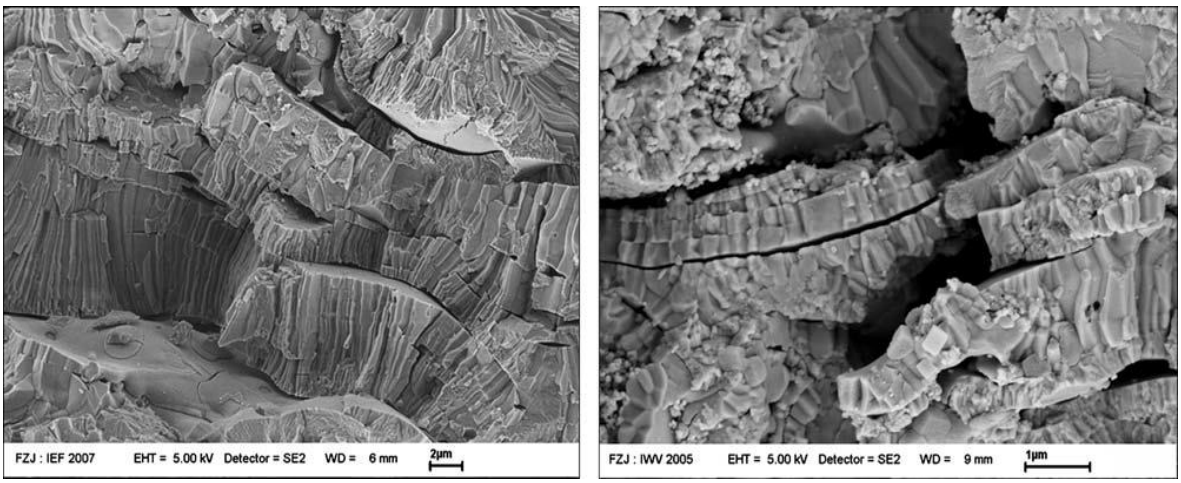

Figure 1-4: Structure of a conventional APS coating (left) and a SPS coating (right). [5]

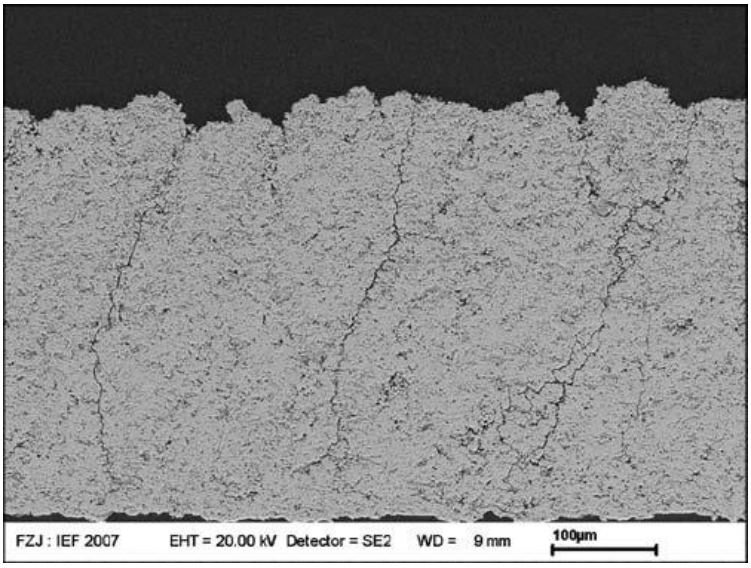

Figure 1-5: Cross section of an YSZ SPS coating with segmentation cracks. [5]

Figure 1-4 shows a comparison between the microstructure formed by conventional APS and SPS. SPS coating has an increased number of lamellas. Due to the increased cooling rate, also the trans-splat grains in the SPS splats are much higher than in an APS splat. The coating is denser in SPS with less pores. Figure 1-5 shows a cross section for the microstructure for YSZ coating using SPS process. The coating shows the segmentation cracks with less pores. [5]

For more than 25 years, research laboratories studied the spray process parameters and the coating's microstructure. Also, they tried to link the in-flight particle characteristics (temperature and velocity) to the coating microstructure. Optical sensors are considered important and feasible tools to achieve this objective based on the particle's spectral emissions. The measurement is based on the thermal radiation of the hot particles in the field of view of the optical system.

The in-flight particle characteristics are strongly linked to their trajectory in the plasma jet which depends on the particles momentum, the carrier gas flow rate, the particles size, the injector internal diameter and the injector position. However in order to achieve good coatings, the particles should be in a plastic or molten state. Sensors permit to monitor in-flight particle characteristics by modifying correspondingly the intrinsic operating parameters such as arc current intensity, primary and secondary plasma gas flow rates and feedstock injection parameters.[6, 7, 8]

Therefore, it is useful to investigate the particle's diagnostics relation to the spraying process parameters. In the meantime, it is essential to review the particle's diagnostics and microstructure relationship to achieve desired coating with functional and engineered properties. In the following section, an overview concerning the influence of the in-flight particle's temperature on both the spraying operating conditions and the deposited coating's microstructure basic features will be discussed. The aim of this section is to highlight the value of particle diagnostics, and how they could help to better understand and optimize the various thermal spray processes.

1.1 SPRAYING PARAMETERS AND PARTICLE'S BEHAVIOR RELATIONSHIP DURING SPRAYING

The thermomechanical properties of the sprayed coatings are directly linked to the plasticity and the temperature of the sprayed particles upon their impact on the substrate which control their cooling and the splat formation. The temperature and velocity of the particles upon their impact are controlled by two main dominant components. The first component is the plasma jet parameters (gas nature, velocity, distribution and the gas turbulent mixing with the surroundings). The second component is the particle's trajectory in the plasma jet.

The particle's trajectory is controlled by the injection velocity, the position where it is injected, its nature, density, size and morphology. The particle's momentum upon injection determines the heat treatment to the particles while traveling in the jet stream because the local temperature varies steeply within the plume in the hot spraying processes like APS, SPS, VPS and HVOF.

1.1.1 Influence of Particle's Injection Momentum

The particle's injection momentum has to be adjusted, so they travel through the hot zones of the plume while spraying. Along the plasma jet, very different mean particle's trajectory can be observed based on the carrier gas flow rate and the particle's size distribution, as it is illustrated in Figure 1-6, 7. When the particle's momentum is low, they don't penetrate into the plasma jet.

On the other hand, when it's too high they travel across it. The optimum particle's trajectory corresponds to the highest surface temperature which contributes relatively to higher deposition efficiency. [9]

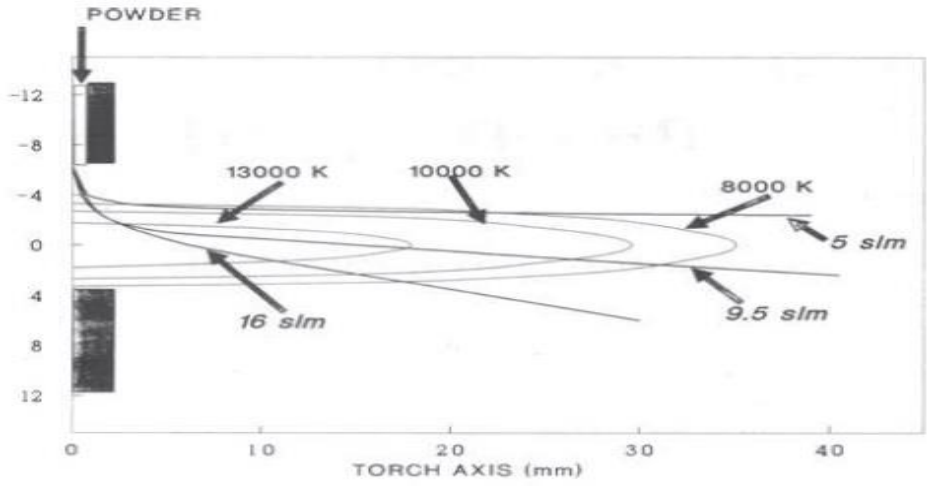

Figure 1-6: Yttria stabilized zirconia 8% wt. particles mean trajectory in Ar-H2 plasma jet. Ar 75 slm, H2 15 slm. Nozzle diameter = 8mm. I = 450 A, V = 71 V. Injector's internal diameter 1.6mm. Particle's diameter = 25 microns. [9]

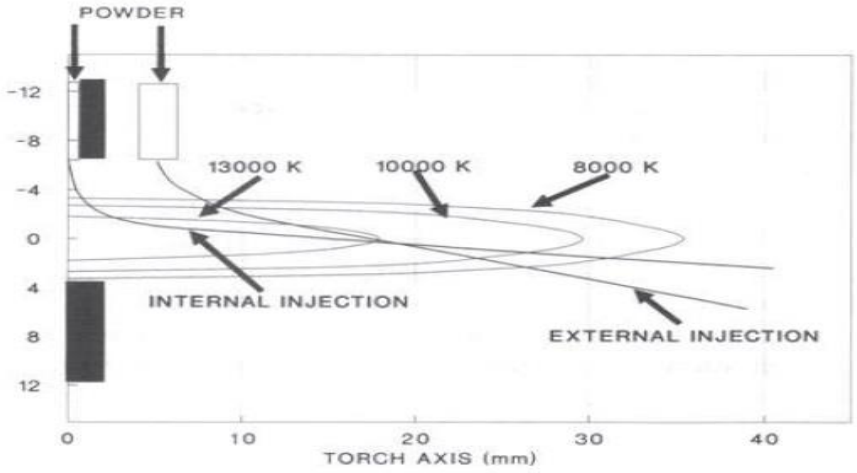

Figure 1-7: Illustration of the influence of injection position on the mean particle's trajectory. [9]

1.1.2 Influence of Injector's Tilting

Tilting the injector in a counter flow configuration to the plasma jet permits longer residence for the particle in the hot zones of the plasma, as it is shown in Figure 1-8. This tilting has a drastic influence on the mean velocity and the temperature of the particles along their mean trajectory as illustrated in Figure 1-9. The higher temperature was detected at an angle of 60° counter flow is due the longer residence of the particles in the hot zones of the plasma jet.[9]

Undoubtedly, the spraying parameters like arc current, gas flow rate, gas nature and torch design are playing such important roles on the behavior of the particles in-flight. Any parameter that tends to increase the power like the arc current or the percentage of H_2 will affect the velocity and the length of the plasma jet. Any increase in the velocity of the plasma jet enhances the thermofluid interaction.

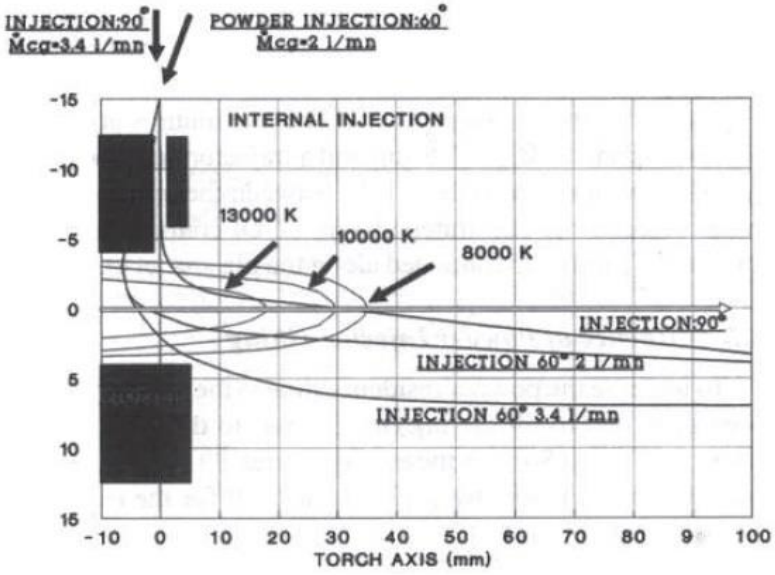

Figure 1-8: Calcia-stabilized zirconia with diameter 77 microns mean trajectory when injected orthogonal to jet axis and 60° counter flow. [9]

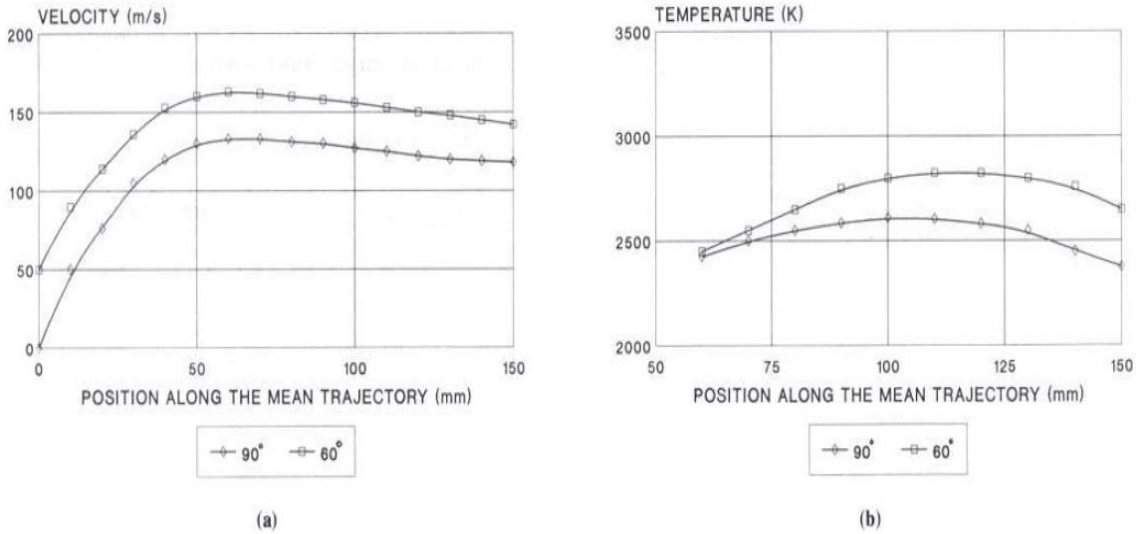

Figure 1-9: Mean particle's velocity and temperature at two different injection angles 90 ° and 60 °. [9]

On the other side, the particles heat treatment does not depend only on the enthalpy of the plasma; it also depends on the thermal conductivity of the plasma gas which is improved by including a secondary gas like hydrogen and helium. [9]

1.1.2.1 Influence of Power Level

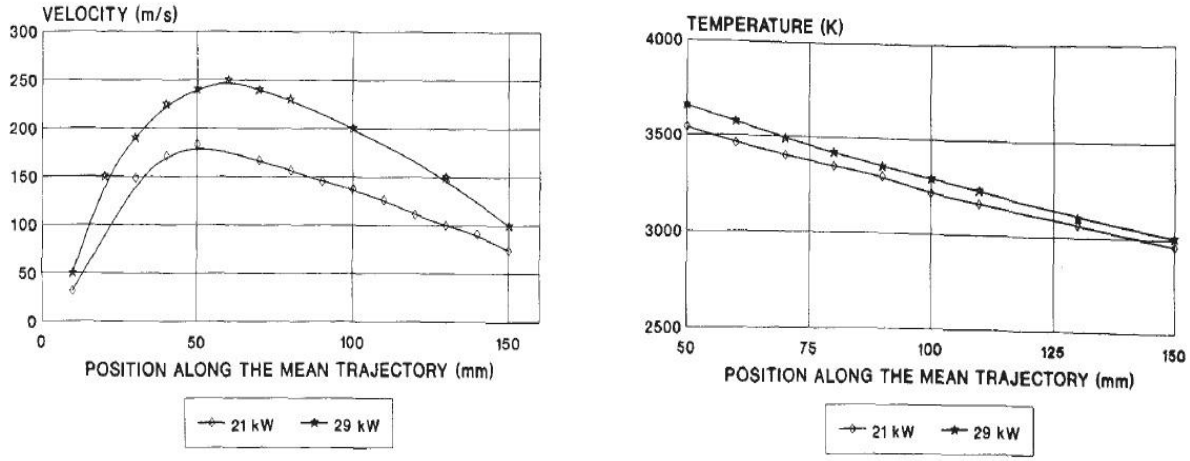

Figure 1-10: The evolution of particle's velocity and temperature at different power levels. [9]

The increase of power level by increasing the arc current leads to a significant shift of the particle's velocity. However, the increase in temperature is limited. As it's illustrated in Figure 1-10 by increasing the plasma torch power from 21 to 29 KW, the velocity was increased by 40 %, and the temperature increased only 5 %. On the other hand, the plasma length was increased only by 8 %. This will lead to a shorter particle's residence time, and an increase in the enthalpy. [9]

1.1.2.2 Influence of Plasma Fluctuations

J.F. Bisson et al investigated the influence of the arc root fluctuations on the variations of temperature and velocity. To conduct this work, an electrical circuit was integrated to DPV2000 which was triggered to function when a certain threshold of voltage is surpassed. DPV2000 is an optical sensor the measurement of the particle's velocity, diameter and temperature.[10]

In this experiment, the voltage fluctuations are depicted according to Figure 1-11. The time resolved diagnostics of this experiment showed a considerable variation of temperature and velocity as a result of the fluctuations of arc root in the core of the plasma torch as a function of time delay. Figure 1-12 illustrates these variations. [10]

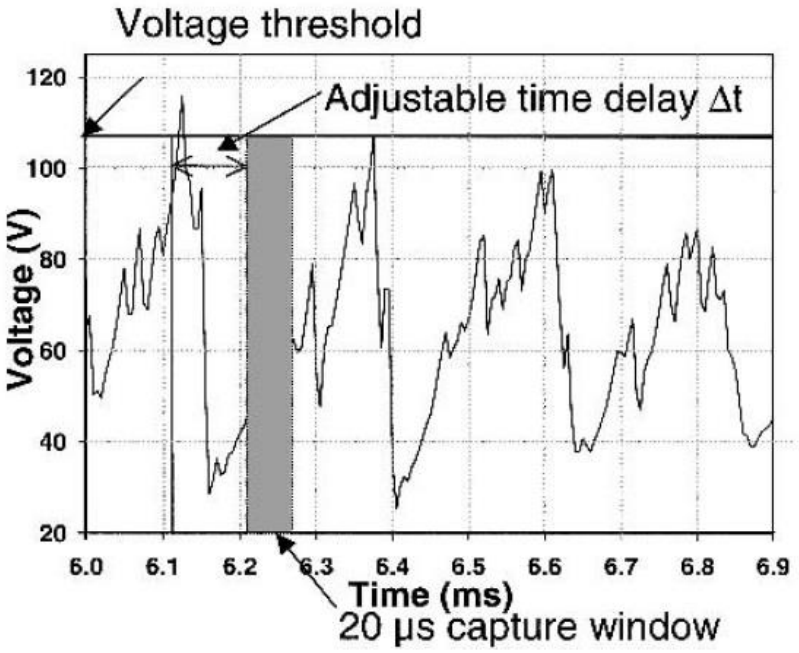

Figure 1-11: Plasma torch voltage fluctuations and the threshold. [10]

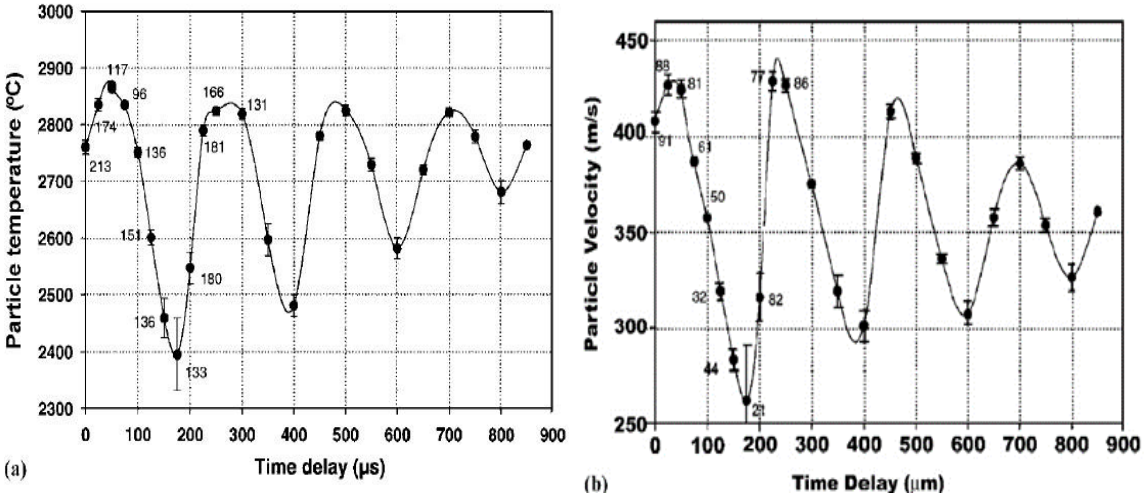

Figure 1-12: The variations of temperature and velocity as a function of time delay as a result of the fluctuation of arc root's voltage. [10]

1.1.3 Microstructure

In the following part, the influence of particle's temperature on selected coating features is going to be reviewed. M. Gaona et al investigated nano-powders (titania) deposited via High Velocity Oxygen Fuel (Oxygen and Propylene) to highlight the implications of particle's temperature on some coating's basic features like; the microstructure, phase composition and porosity. The temperature and velocity of in-flight agglomerated particles were analyzed using DPV2000 (TECNAR Automation). [11]

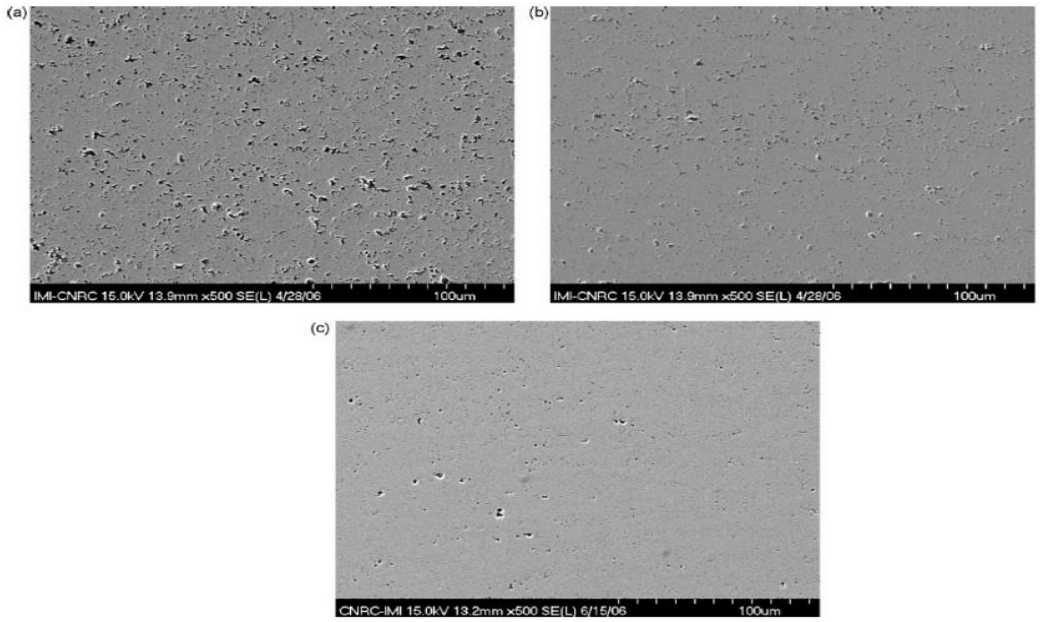

Figure 1-13: SEM microstructure images. A) Propylene 65 slm. B) Propylene 70 slm. C) Propylene 90 slm.[11]

The influence of particle's surface temperature on the microstructure is significant. Injecting different concentrations of propylene in the gas mixture led to a significant change in particle's surface temperature because the higher the propylene concentration in the mixture, the higher the temperature of the particles in-flight which affected the microstructure consequently as it's illustrated in Figure 1-13. The particles injected in higher propylene concentrations produced more dense coatings with less pores compared to the particles injected at lower propylene concentrations.

The dense coating can be attributed to the molten state of the particles before impact. In contrary, when the particles were not in a fully molten state, the deposited coating is more porous. [11]

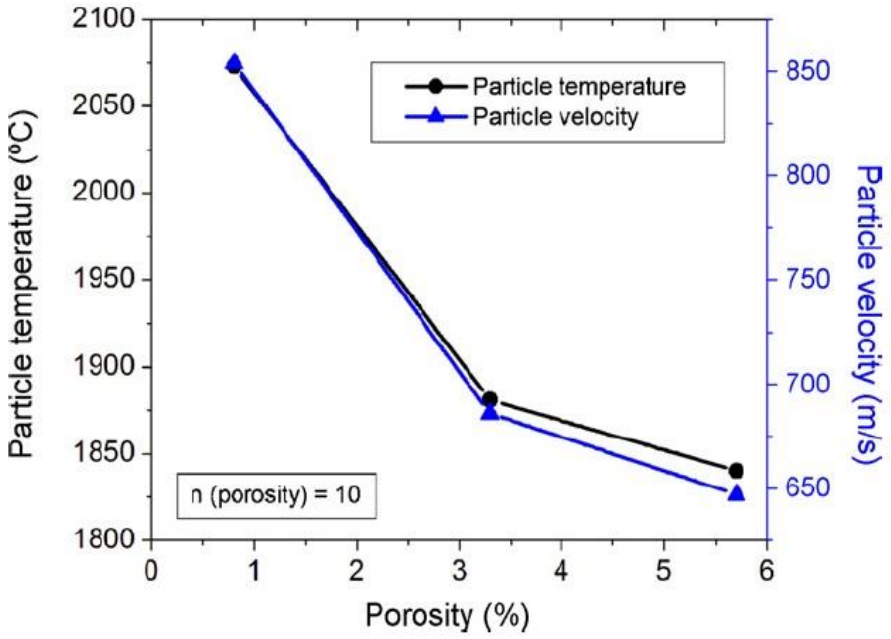

Figure 1-14: Coating's porosity as a function of particle's temperature and velocity. [5]

The dependence of the deposited coating's porosity on the average temperature of in-flight particles is essential. It can be clearly observed in Figure 1-14 that higher temperature results in lower porosity in the deposited coating. This is attributed to the higher kinetic and heat energy transferred to the particles in-flight. [5]

1.1.4 Phase Composition

Two phases of titania powder anatase and rutile were detected in the XRD pattern in the scanned samples. The feedstock of titania is initially in an anatase phase, and the XRD pattern for the deposited coating showed a major phase of rutile, and residual anatase. It was observed that the temperature of the particles is a key player in the phase composition of the deposited coating. Figure 1-15 shows anatase phase volume concentration in the deposited coating as a function of particle's temperature and velocity. The anatase phase found in these coatings was probably the result of

semi-molten feedstock particles that became embedded in the coating microstructure after thermal spraying. [5]

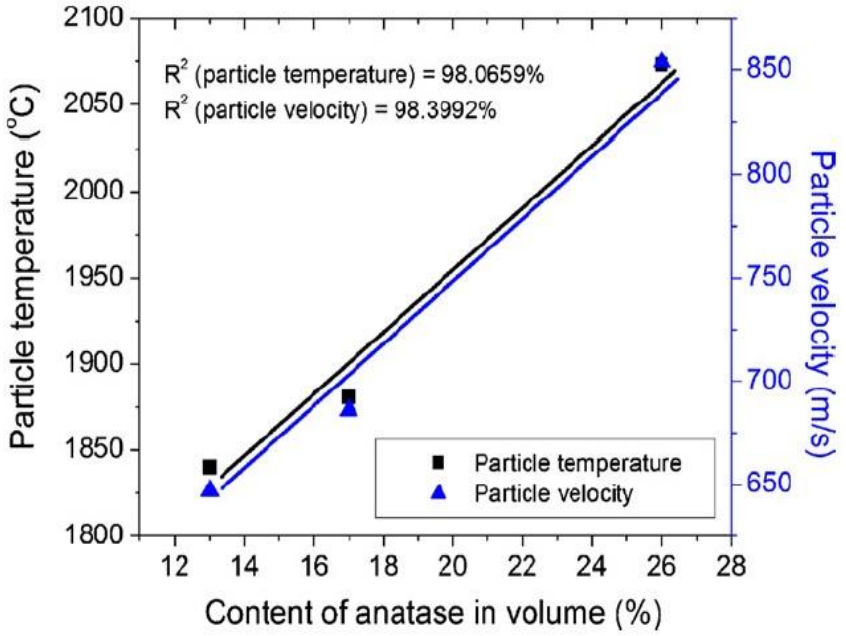

Figure 1-15: Anatase phase concentration in the total volume of coating as a function of temperature and velocity. [5]

1.2 DIAGNOSTIC SYSTEMS

Based on the previously mentioned introduction, it can be confidently concluded that by the knowledge of in-flight particle diagnostics; an overall better realization to the thermal spray processes in terms of the optimization of the operating conditions and their link to the microstructure's basic features can be obtained. Therefore, it is important to have a general understanding to the commercial diagnostic systems and the general operating theory to each one of them.

1.2.1 DPV2000 Diagnostic System [6]

This system enables the measurement of single particle's velocity, temperature and diameter. The temperature is acquired by calculating the energy ratio emitted at two different wavelengths

assuming that the particles are grey body emitters with the same emissivity at two color bands. Furthermore, the measurement volume of the sensor head is relatively small (Less than 3 mm). [7]

The measuring capabilities are described as follow: [6]

1- Temperature measurements from 1000 to 4000°C.

2- Velocity measurements from 5 to 1200 m/s.

3- Diameter measurements from 10 to 300 µm.

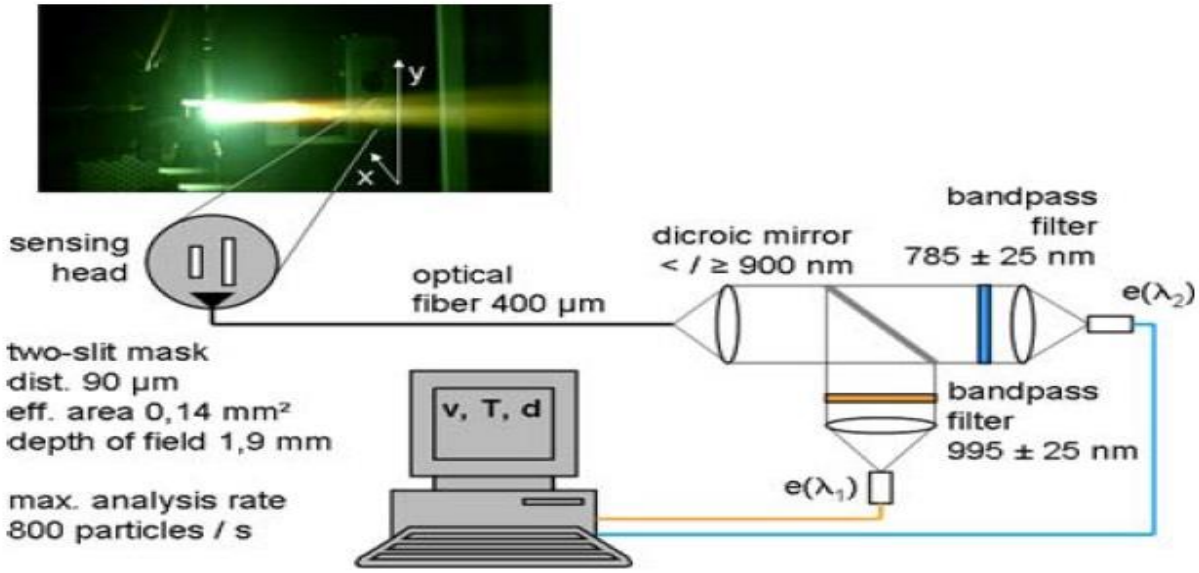

Figure 1-16: DPV2000 Diagnostic System. [6, 14]

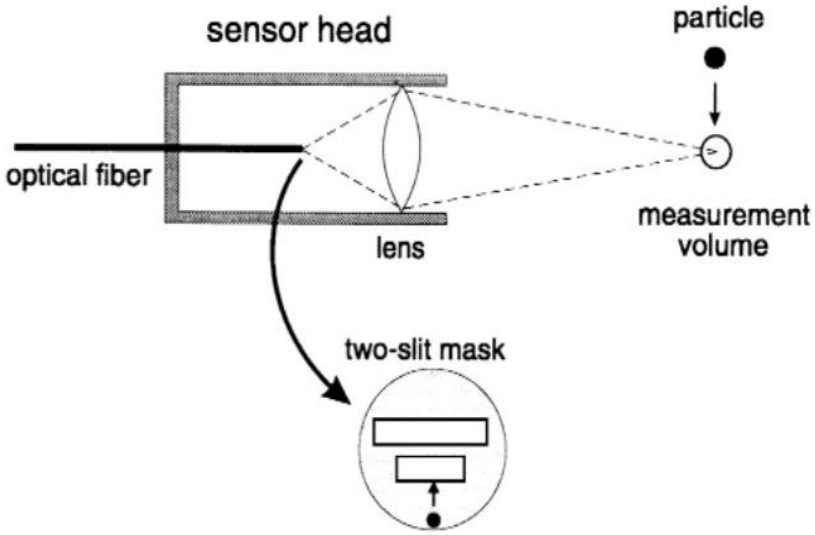

Figure 1-17: DPV2000 Basic Concept. [6, 14]

1.2.2 Accuraspray-g3 Diagnostic System [6]

Accuraspray is providing an average of ensemble particles characteristics in a relatively large measurement volume (Diameter 3 mm X 25 mm). The temperatures are determined by two-color pyrometer for a cloud of particles. The system involves a CCD camera enabling the analysis of the plume appearance (position, width, distribution, intensity) along a line in spray distance perpendicular to the particle jet. [1-3]

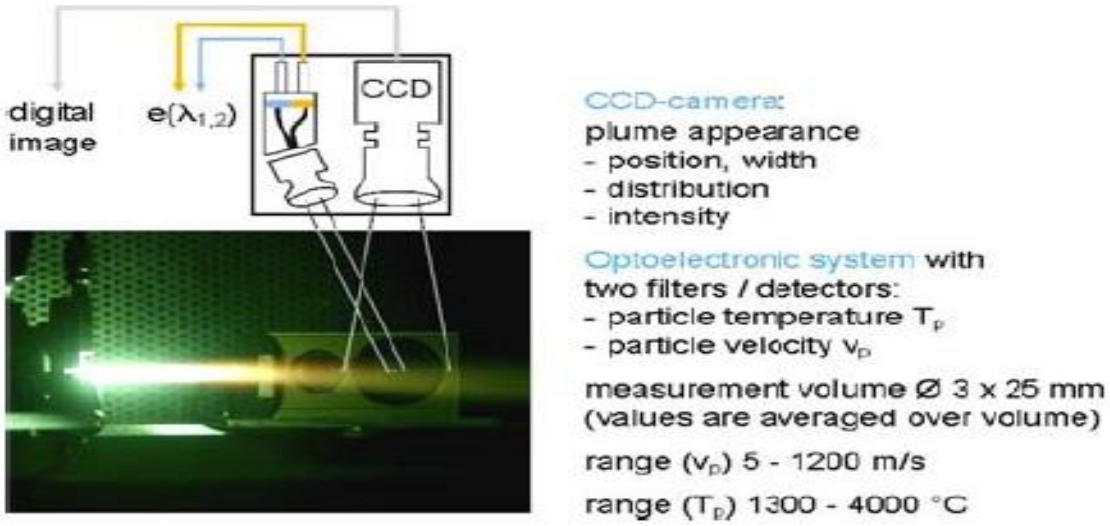

Figure 1-18: Accuraspray operating Principle. [6, 14]

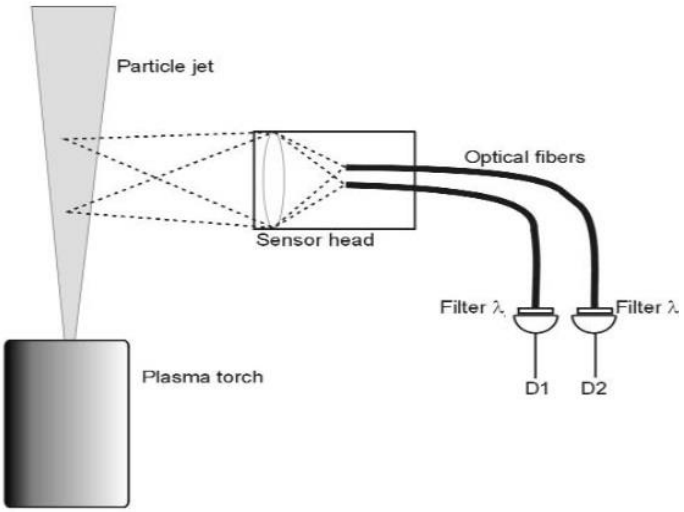

Figure 1-19: Accuraspray Basic Concept. [6, 14]

1.2.3 Spray Watch

The developments leading to the Spray Watch diagnostic systems began at the end of the 90s. [9] A fast shutter CCD camera is used to create digital images of the spray. One typical specification of the CCD array was 1280 horizontal and 1024 vertical pixels, a spectral range 290 nm to 1000 nm, and a maximum frame rate of 7 Hz. Also, the covered measurement volume is adjustable.

Digital images taken with short exposure times are processed by an algorithm identifying individual particles in the images and measuring their position, direction, and velocity. The latter images are obtained from the analysis of streak lines. Thus, the system provides a continuous measurement of particle velocities, flow velocity, spray vertical position, width, angle and divergence. Furthermore, the camera also takes images using a longer exposure time to determine the average particle temperature by two-color pyrometer.

For this purpose, an optical double-stripe filter is integrated in the camera and covers a part of the CCD detector so that the measurement volume is imaged on the CCD array in two different wavelengths.[2]

What so ever the sensor used, prior calibration is mandatory as well as regular ones after a certain time of being in service. Sprayed particle velocity measurements have a precision better than 5 %. A simple system to calibrate them is to place the detector in front of a rotating cylinder with narrow slots and containing a light source. The cylinder rotation velocity is well known, the velocity deduced from the signals given by the detector can be calibrated.

On the other hand for temperature calibration, the most conventional approach is using a tungsten ribbon lamp with a high precision pyrometer or sometimes a blackbody instead of the lamp. The main problem is that emissivity of other substances may be significantly different from those of tungsten and black body. Moreover, the calibration is valid only in the temperature range at which

the tungsten lamp is operated and for which the calibration data are available. Thus, particle temperature of high-melting point materials such as YSZ may exceed this validity range.

1.3 THEORETICAL BACKGROUND

In-flight measurement of the plasma sprayed particles is important for the correlation of particle characteristics to the coating's microstructure and features. However, temperature measurement of in-flight particles was found to be challenging because of the contribution of the non-thermal signals affecting the measurement process and perturbing the obtained signals. [10] In that context, temperature measurement for in-flight particles in suspension plasma spraying becomes even more challenging because of the small diameter of the particles, the metallic vapors and the radiation of the plasma surrounding the particles.

In order to assess the feasibility of temperature measurement for in-flight particles, two color pyrometer and spectroscopic analysis are versatile tools that have been applied before on different thermal spraying processes because they do not disturb the medium under investigation. [11]

The relation between the temperature and the thermal radiation emitted from the particles is depending on the thermal radiative properties of the particles. Planck's law for black body radiation is well describing this relation. Black-body radiation has a characteristic and continuous frequency spectrum that depends on the body's temperature and emissivity, called the Planck spectrum or Planck's law.

The spectrum is peaked at a characteristic frequency that shifts to higher frequencies with increasing the temperature. At the room temperature most of the emission is in the infrared region of the electromagnetic spectrum. As the temperature increases past about 500 ° C, black bodies start to emit significant amounts of radiation in the visible range (390 nm to 750 nm). Figure 1-20 illustrates that relation at various temperatures.

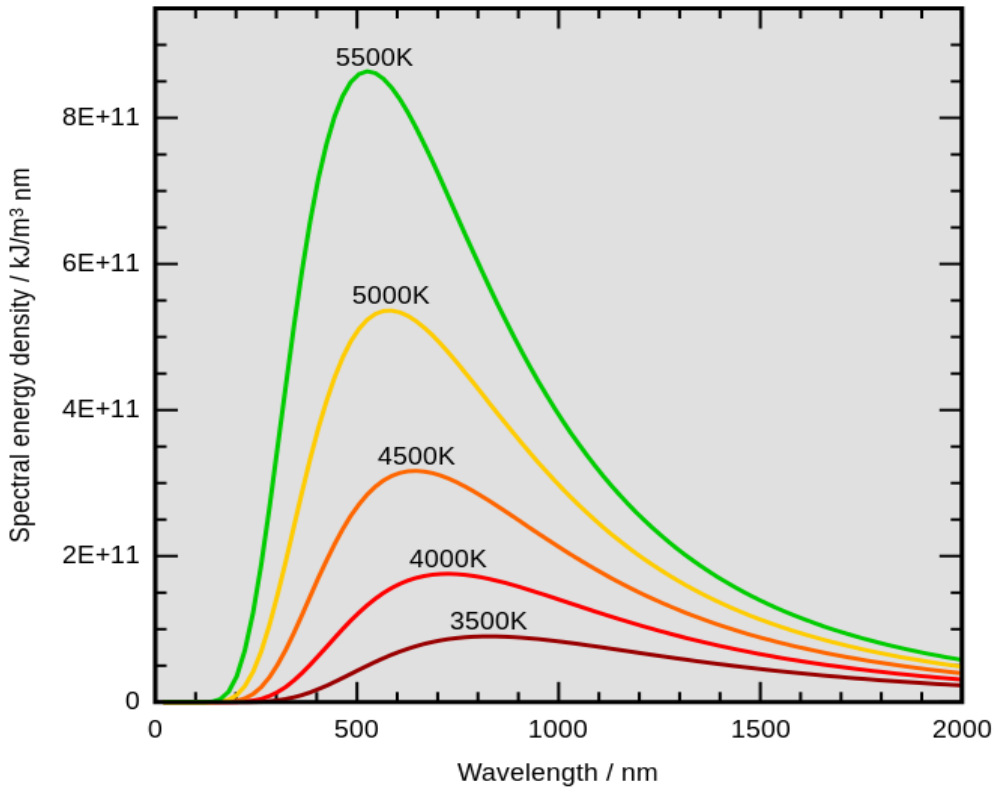

Figure 1-20: Blackbody radiation as a function of wavelength and temperature as it's explained by Planck's law.

*" **Black-body radiation** is the type of electromagnetic radiation within or surrounding a body in thermodynamic equilibrium with its environment, or emitted by a black body (an opaque and non-reflective body) held at constant, uniform temperature. The radiation has a specific spectrum and intensity that depends only on the temperature of the body"* [1]

In this thesis, Yttrium-Stabilized Zirconia (YSZ) particles were assumed to behave as grey bodies with constant emissivity as a function of wavelength. This principle was implied to avoid the complications of the change of emissivity as a result of temperature change. And realistically, the actual emissivity is not well known at all the temperatures. Therefore, considering the change in emissivity while measuring the temperature of the particles appeared to be totally impractical.

Therefore, according to Planck's law and while considering that the emissivity is constant at the wavelength range of interest the following relation can be obtained from Eq. 1-1. [14]

$$I_{em}(\lambda, T) = \varepsilon \frac{C_1}{\lambda^5} d^5 \frac{1}{\{exp\frac{C_2}{\lambda T} - 1\}} d\lambda \qquad \textit{Equation 1-1}$$

Where; I_{em} is the intensity emitted by a black body in W/Sr, λ is the wavelength in m; T is the particle's surface temperature in K; C_1 =9.352 x10^{-17} W.m^2; C_2 =1.439 x10^{-2} m.K; and d is the diameter of the particle in m; ϵ is the emissivity of YSZ was assumed to equal to 0.7. [15] The influence of the emissivity variation (±) with the particle diameter is neglected in this work.

According the two color pyrometer principle, the temperature of in-flight particles can be obtained by taking the ratio between two intensities at two different wavelengths while assuming the grey body hypothesis according to the following relation Eq 1-2.

$$T = \frac{C_2(\lambda_1 - \lambda_2)}{\lambda_1 \lambda_2} . \left[ln\, R + 5\, ln \frac{\lambda_1}{\lambda_2}\right]^{-1} \qquad \textit{Equation 1-2}$$

$$R = \frac{I_{\lambda 1}}{I_{\lambda 2}} \qquad \textit{Equation 1-3}$$

R is defined as the ratio between two intensities at two different wavelengths Eq 1-3. The closer the two wavelength to each other the more accurate the calculated temperature; however, the sensitivity is less too. This ratio is affected by the presence of none thermal signals in the collected spectra. Therefore, it can be redefined while taking into account the contribution of none thermal signals according to the following form Eq 1-4:

$$R = \frac{I_{\lambda 1}}{I_{\lambda 2}} = \frac{I_{p\lambda 1} + I_{S\lambda 1} + I_{pS\lambda 1}}{I_{p\lambda 2} + I_{S\lambda 2} + I_{pS\lambda 2}} \qquad \textit{Equation 1-4}$$

Where; $I_{p\lambda 1}$ is the thermal radiation directly emitted from the particles; $I_{S\lambda 1}$ is the plasma radiation scattered by the particles and $I_{pS\lambda 1}$ is the plasma radiation generated by the plasma torch and surrounds the particles in the volume measurement at the wavelength of interest. Figure 1-21 illustrates those components. A detailed elaboration about each component will be presented in the upcoming sections.

1.4 THERMAL AND NON-THERMAL RADIATION

There are certain sources of non-thermal radiation that can affect the temperature measurement of the particles as depicted in Figure 1-21. Those non-thermal signals can lead to significant errors, and are generated from [10]:

a) The radiation emitted directly from the plasma and surrounding the particles in the field of view of the optical pyrometer.

b) The radiation produced by the arc in the core of the plasma gun and scattered by the in-flight particles in all directions.

c) The radiation emitted by the metallic vapors of the particles themselves; or in other words, the influence of the plasma which surrounds the particles.

This latter source of radiation is one of the most important misleading sources, as it can contribute to a significant increase in the continuum background of the measured spectra when the powders are injected in the plasma. Additionally, the distance traveled by the particles from the torch exit plane, the particle's optical properties, particle's size and their surface temperature can play a significant role in the measurement error as well.

Several authors have pointed out that the primary limitation in measuring particle thermal emission is the presence of the bright plasma near the exit of the plasma torch. Sakuta and Boulos have calculated the relative intensities of plasma and particle emission in the detector field of view, in an effort to determine where the plasma signal drowns out the particle thermal emission. They concluded that below 4 cm the plasma radiation is very intense and overwhelming to any other source of radiation. Furthermore, it is important to note that their work was carried out using radio frequency plasma torch. [16]

Gougeon and Moreau have determined the influence of particle-reflected plasma light that is collected with the thermal emissions on temperature measurement. Their calculations showed that

the particle-reflected radiation can represent a significant source of error on temperature measurement. The smaller the particle size, and cooler, closer to the torch exit plan; the more significant the error is. However from a simulated particle radiation reflection measurement, Prucha and Skarda concluded that the plasma light scattered by the particles does not need to be considered for in-flight particle pyrometry. [17, 18]

Clearly, more accurate assessment of the non-thermal signals will help to better understand the limitations of in-flight particle pyrometry. Furthermore, if non-thermal signals can be subtracted from the raw collected signals, more accurate temperature measurements can be obtained.

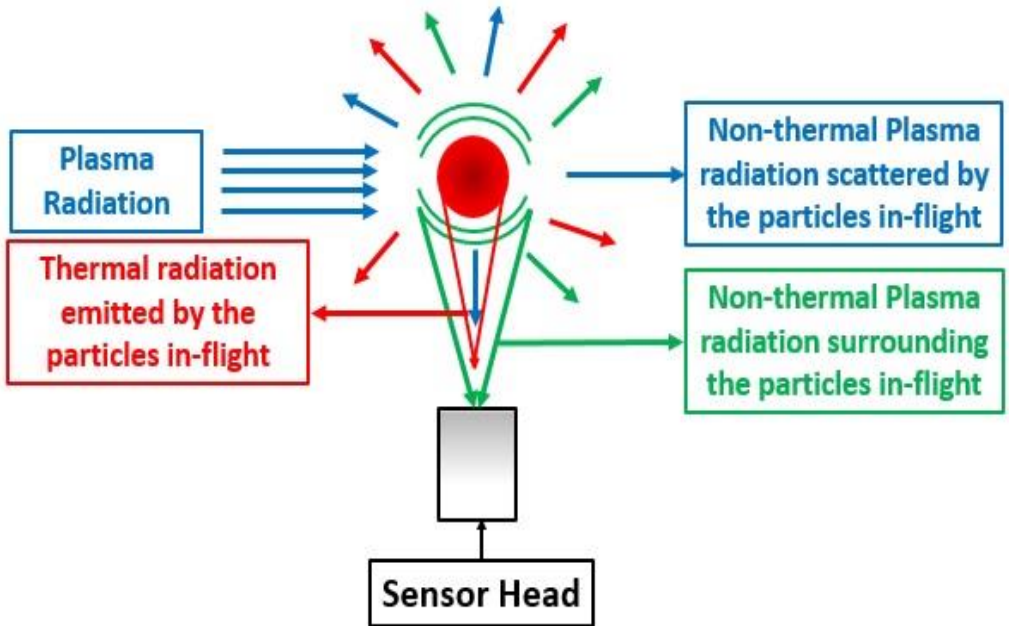

Figure 1-21: A schematic to describe the thermal and non-thermal signals detected by the sensor head.

1.4.1 Scattered Radiation

Several studies investigated spectroscopically the visible and near infra-red range for in-flight particles in Air Plasma Spray (APS) and Vacuum Plasma Spray (VPS) in order to assess the temperature of in-flight particles. In APS, Gougeon and Moreau studied the influence of plasma radiation scattered by in-flight particles in APS in the range of 650 nm up to 1050 nm while spraying 50 μm nickel particles.

This source of non-thermal signal was extensively investigated in their work by collecting the spectra from the axial direction to the plasma torch at 34 cm distance using a bare fiber optic directly connected to a spectrometer equipped with Silicon detectors. This spectrometer was radiometrically calibrated using a blackbody source with an emissivity = 0.99 at 1500 °C. Figure 1-22 is illustrating the calibration factor.

They assumed that the evolution of the power density changes as a function of distance according to the inverse square law. This assumption was used to assess the incident power on the particles at 10 cm from the plasma torch plane, as it is an essential input to calculate the plasma radiation scattered by the particles in-flight.

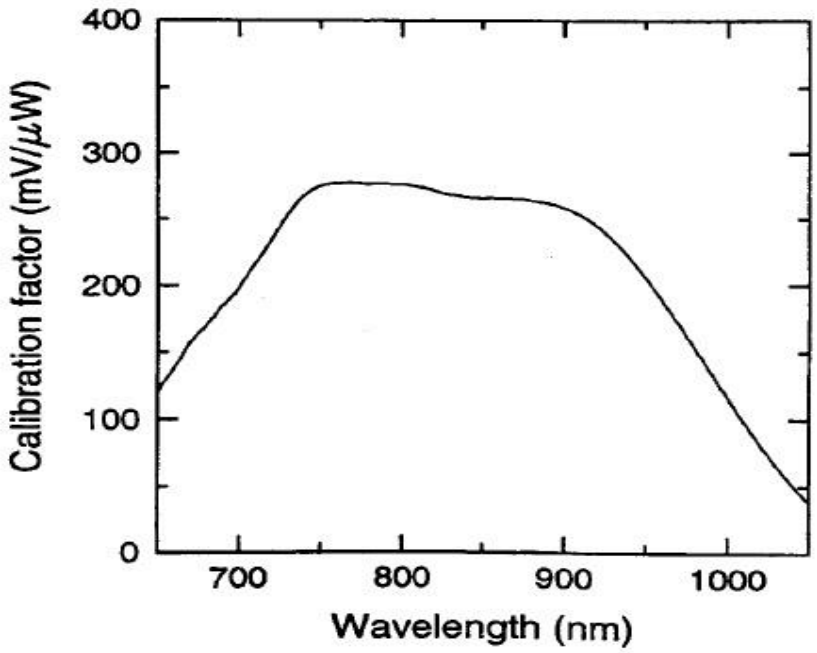

Figure 1-22: Spectrometer's calibration factor as a function of wavelength. [18]

By knowing the optical properties of the nickel particles, the particle's size distribution and the power density incident on the particles at the location of interest; the plasma intensity scattered by those particles was calculated using Mie. Scattering theory as shown in Figure 1-23. Their work demonstrated that the contribution of the plasma radiation scattered by in-flight nickel particles led

to almost 100 °C error in temperature measurement at 1550°C true particle's surface temperature, as its illustrated Figure 1-24. [18]

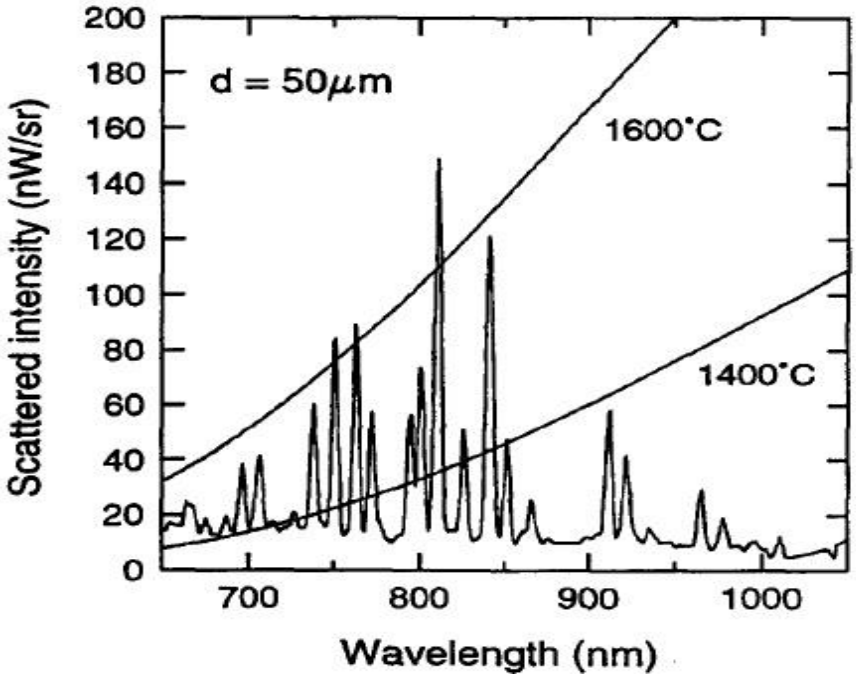

Figure 1-23: The intensity scattered by the particles as a function of wavelength. [18]

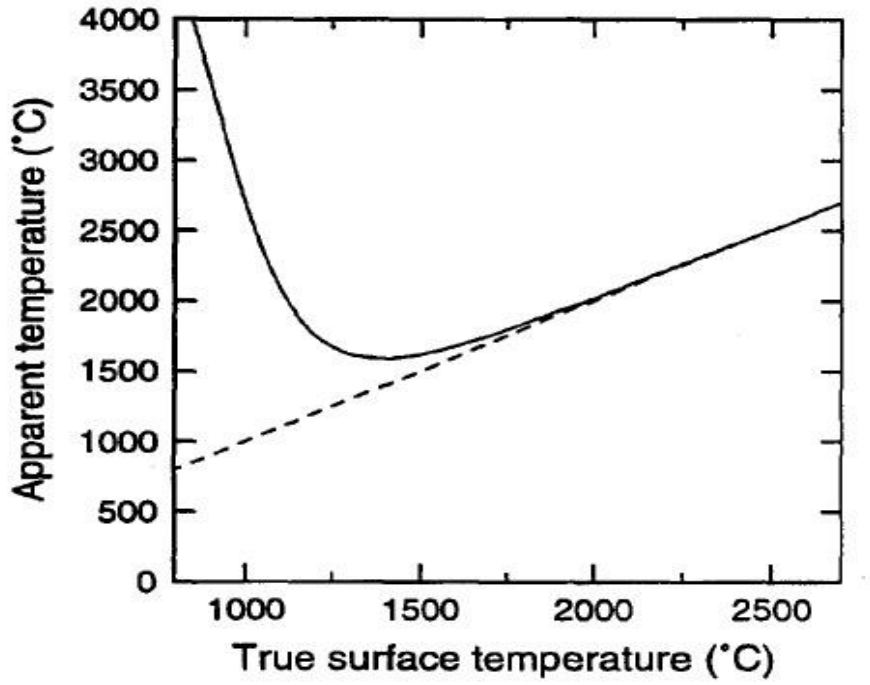

Figure 1-24: Apparent temperature Vs true particle's surface temperature. [18]

Another attempt by Salhi et al was carried out to assess the plasma light scattered by in-flight particles in the visible to near infrared range using two different techniques. They introduced a second injector to the plasma jet while injecting cold copper particles at different location from the initial point of injection. When starting the ignition of the plasma torch, the cold particles passing through the measurement volume scatter the light coming from the plasma source; this light is collected by the detection head and transmitted to the pyrometric system to give the intensity of the scattered light in the output of detector. [11]

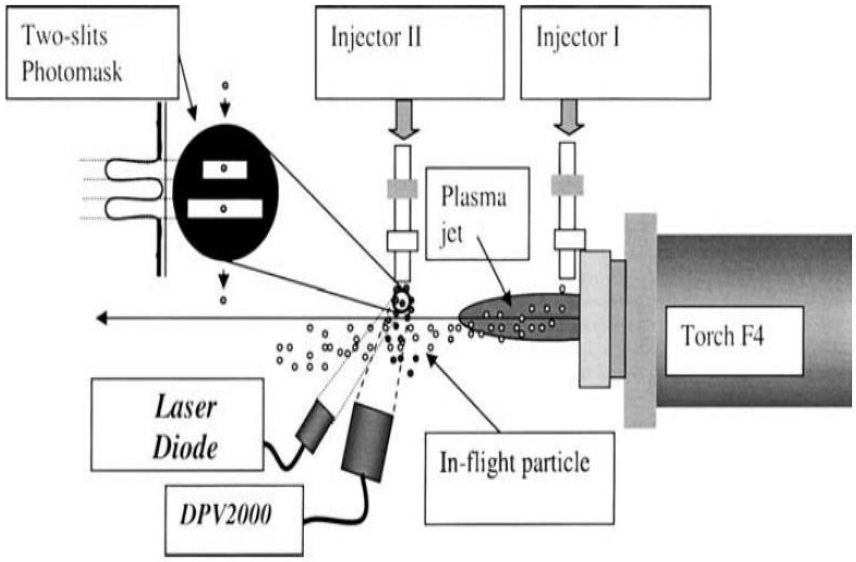

Figure 1-25: Experimental setup to measure the intensity scattered by the particles. [11]

The measurement of the in-flight particle's temperature was obtained using DPV2000 which was previously described in the introduction. Their experimental set up is depicted in Figure 1-25. Furthermore, they tried different particle's emissivity to assess the contribution of the emissivity on the temperature measurement. Their work demonstrated that the influence of the plasma light scattered by the in-flight particles while taking the particle's emissivity into consideration was not negligible and led to significant errors as it is illustrated in Figure 1-26, 27. [11]

Salhi et al also tried to measure the temperature of in-flight particles YSZ in vacuum plasma spray (VPS) using high speed pyrometer DPV2000 from TECNAR [6], and their principle conclusions

were that it was hard to measure the temperature at shorter spray distances because of the intense plasma emissions. On the other hand, measuring the temperature at longer distances becomes even more difficult because of the low mean temperature of the particles. [19]

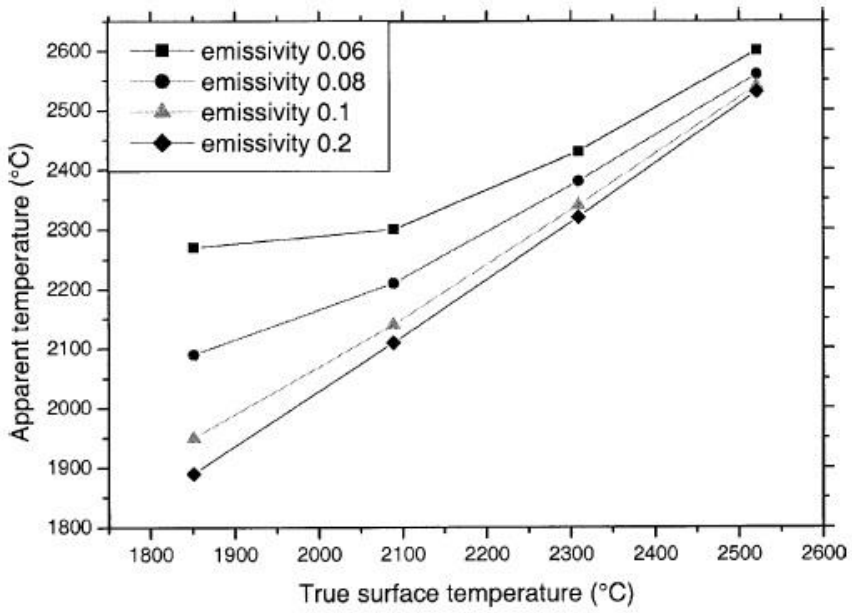

Figure 1-26: Apparent temperature Vs true particles' surface temperature. [11]

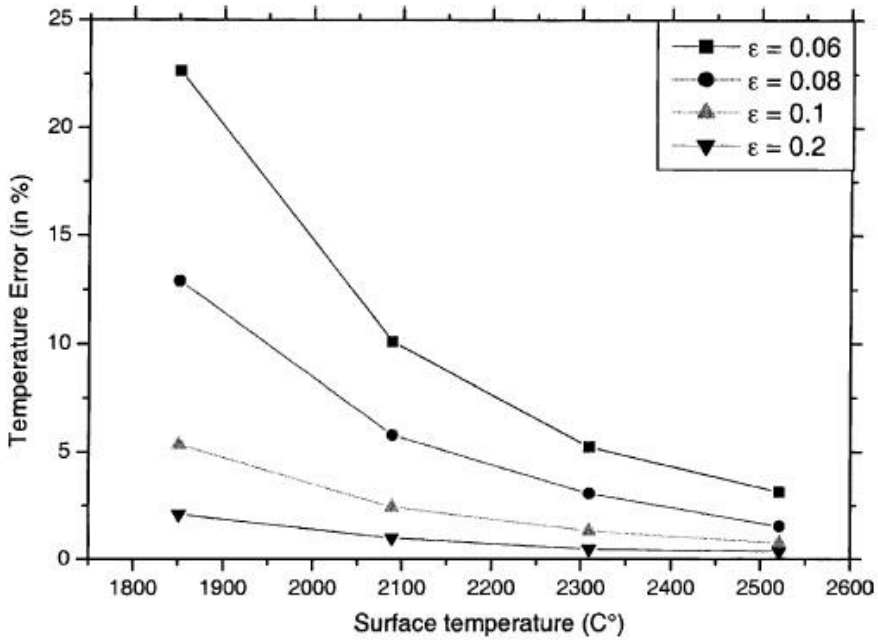

Figure 1-27: Temperature error as a function of particle's surface temperature. [11]

1.4.2 Vapors and Atomic Lines

One other source of non-thermal radiation is the vapor produced by the evaporation of the outer surface of the particles in the hot plasma due to the collisions with the hot plasma constituents. Energy is imparted to the vapor released from the particle. The atomic lines are fundamentally originated by the transitions of the electrons from higher orbital energy levels to lower energy ones. When such a transition occurs, an energy is emitted from the ions producing characteristic radiation with a specific frequency, and it is detected at a specific wavelength. The detected lines are attributed to the plasma ions and the ions of the material being fed in the plasma volume.

Hollis and Neiser acquired two spectral signals for molybdenum particles in APS from the perpendicular direction to the spray axis. The first signal was taken for the plasma only, and the second one to the plasma while injecting the particles. When particles are introduced to the plasma jet; realistically, the plasma conditions are being changed due to several reasons. One of the main reasons is the particle's evaporation.

They concluded that several atomic lines in the collected spectra were attributed to the plasma gases, molybdenum ions and the impurities existed in the powder. Furthermore, the width of vapor's signal relative to X and Y direction relative to the torch axis during scanning tends to decrease at longer axial locations for a given atomic line. This was explained as a result of the regression of the molybdenum ion's thermal emissions in the hot regions of the plasma plume.[17]

1.4.3 Particle Masking Effect

The particle's masking effect occurs when particles pass through the collection volume of the detection system. The light behind the particles, either from the thermal emissions of other particles or from none thermal emission are blocked from the detector field of view by their opacity. Therefore, the radiation signal detected is reduced in proportion to the number and size of masking

particles in the detection volume. Hollis and Neiser demonstrated statistically that the probability of having an opaque particle to block part of the radiation is very low. [17]

1.4.4 Spectral Plasma Loading Effect

The spectral plasma loading effect occurs when particles are introduced into the plasma plume. The plasma emission is decreased by two mechanisms. The first is from particles absorbing energy from the plasma by heat transfer. The decrease in plasma temperature causes a subsequent decrease in plasma emission. The second mechanism whereby the spectral plasma loading effect modifies the collected radiation spectra is vapor absorption.

The vapor which emanates from the rapidly heated particle surface absorbs some of the plasma radiation, thereby attenuating the plasma emission signal. By looking at the intense argon lines spectrum at the same axial location while collecting the spectra with and without the particles, the previously mentioned researchers found that there was an evident decrease in the relative intensity of the atomic argon lines when the particles where introduced; a part of this attenuation could be attributed to the plasma loading effect which means that part of the energy is consumed by the particles.[17]

1.5 RESEARCH MOTIVATION

The main research motivation in this work is to investigate the influence of plasma radiation scattered by in-flight particles and the plasma itself on temperature measurement for in-flight yttria-stabilized zirconia particles in suspension plasma spraying because of the industrial need for the optimization of this process by analyzing the spectroscopic emissions generated from the plasma while injecting the particles. The expected outcome is a more accurate assessment to the feasibility of two color pyrometer in order to determine the temperature of in-flight particles.

As mentioned before in the literature, the temperature of in-flight particles is a key element to optimize the operating conditions of spraying because it has a direct influence on various features of the coating.

In this work, the emission spectra in the visible/near infrared optical range (600 nm to 2500 nm) will be investigated from two different positions. Firstly, the emitted spectra will be recorded from the front direction in order to assess the influence of the plasma radiation emitted from the core of the plasma torch that is reflected by the in-flight particles in all spatial directions on the temperature measurement.

Secondly, emission spectra were collected radially relative to the torch axis at different axial locations to investigate the influence of the plasma on temperature measurement. To conduct those measurements, 20 wt. % YSZ particles in pure ethanol were sprayed. This type of powder was selected, as it is commonly used in thermal barrier coating and fuel cells applications. However in this case, 20 wt. % of powder was chosen to fit more with fuel cell application.[21]

The major previous research efforts for the same type of work were carried out in the visible and ultraviolet range for APS. However one of the main core points that highlight the value and the significance of this work are the investigations which were conducted in the NIR range up to 2500 nm. On the other hand, the thermal emissions generated from the particles at their melting point is peaked at almost 1µm; therefore, this region is favored to be studied in that work, as it increases the feasibility of two color pyrometer calculations to assess the temperature of the particles in-flight.

Chapter 2

Experimental setup

2 EXPERIMENTAL SETUP

The experimental work of this research can be summarized into two stages. The first stage, spectroscopic scanning for the visible and near infrared ranges from 600 nm to 1100 nm will be carried out using a spectrometer equipped with silicon detector; the measurements will be done from two different directions. The first one was acquired exactly from the front location relative to the plasma torch at different distances. The second stage was obtained from the radial direction only at different axial locations. The wavelength range of interest is from 1100 nm to 2500 nm. The photodetector equipped in this spectrometer is InGaAs detector.

2.1 VISIBLE AND NIR RANGES (600 NM TO 1100 NM)

2.1.1 Optical and Acquisition System

The spectroscopic measurements for the VIS/NIR range were carried out using a high sensitivity spectrometer (350 nm to 1100 nm) from Photon Control.[22] This spectrometer is equipped with 2048x64 pixel Hamamatsu S11071-1106 back-thinned CCD camera with anti-blooming technology Figure 2-1.[23] The spectrometer's entrance slit size is 50μm, which affords a reasonable resolving power of about 1.5 nm as illustrated in Figure 2-2. In addition, the grating of this spectrometer was blazed at 500 nm in order to have higher efficiency at the desired wavelength range as shown in Figure 2-3. An optical fiber with SMA 905 connectors is coupled with the spectrometer. Its core diameter is 200 μm with a 0.22 numerical aperture.

The fiber optic was coupled via SMA 905 connector with the optical head which contains rotating optical adjustment from Thorlabs. [24] The diameter of this tube was 1 inch. The optical components were fixed inside using retaining rings and spanner wrenches. Figure 2-4 illustrates the schematic of the optical head.

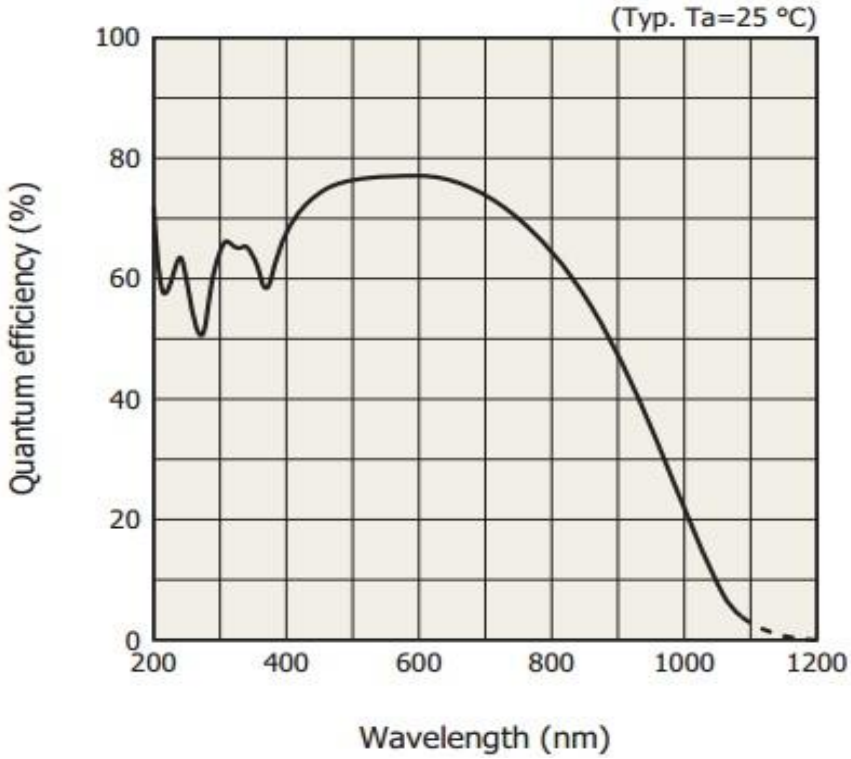

Figure 2-1: CCD quantum Efficiency as a function of wavelength. [23]

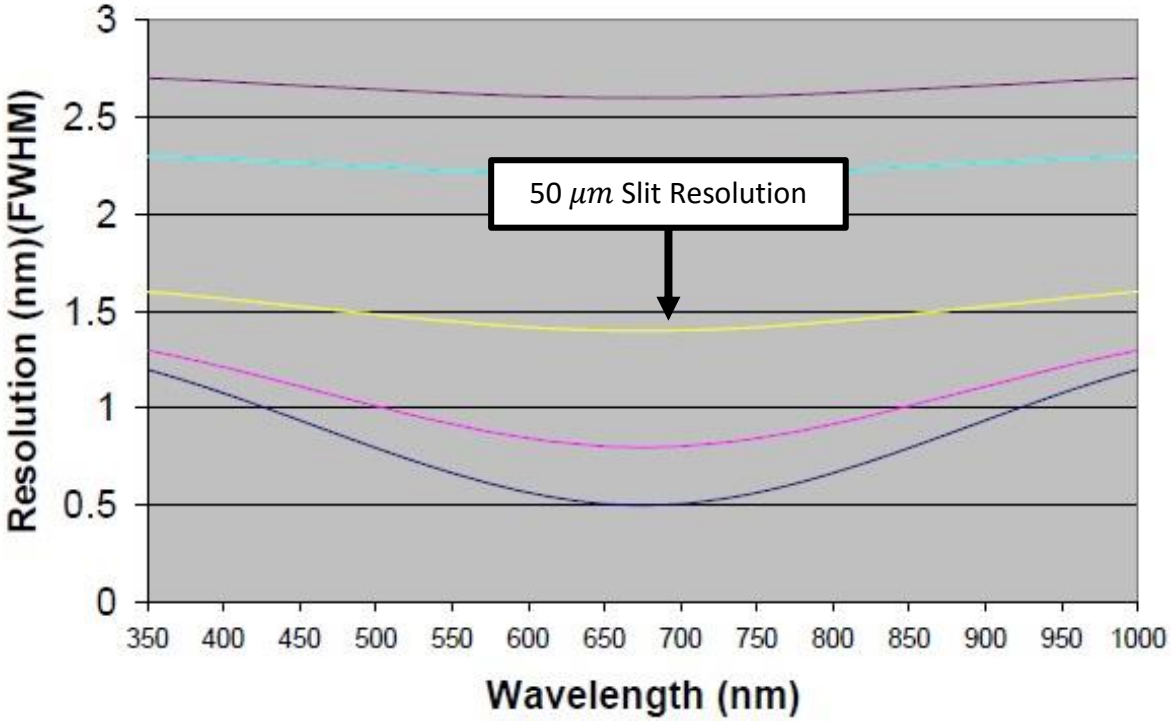

Figure 2-2: 50 μm slit resolution as a function of wavelength. [22]

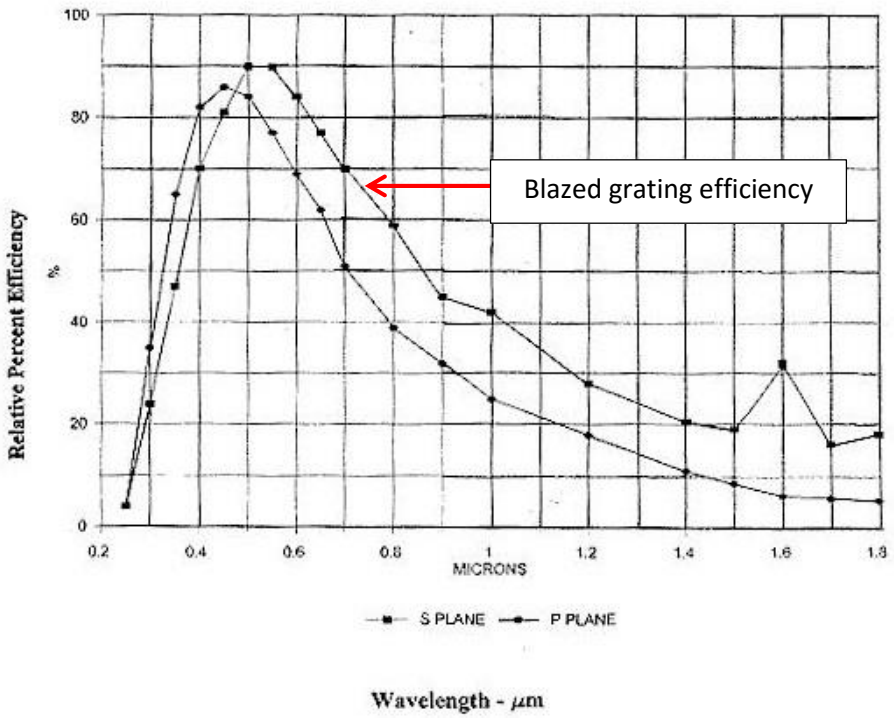

Figure 2-3: Blazed Grating efficiency as a function of Wavelength. [22]

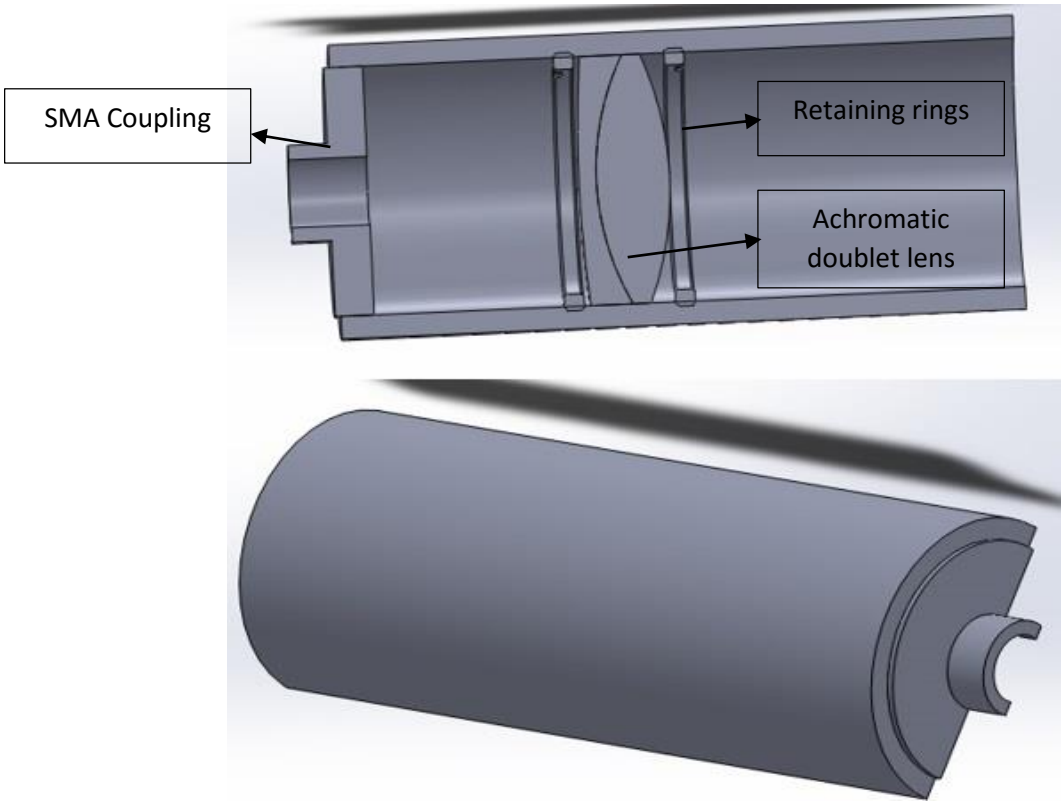

Figure 2-4: Optical head schematic.

2.1.2 Front Measurement

To calculate the power incident on the particles, the emitted spectra were collected on 3 consecutive stages:

1- For the plasma only.

2- The plasma while injecting the ethanol and the surfactant.

3- Finally to the plasma while injecting the suspension.

Those measurements were carried out using a bare fiber optic. The numerical aperture of the fiber is large enough to collect the radiation from the whole plasma volume. The experimental setup for this step is illustrated in the schematic of Figure 2-5.

The spectra were collected at 80 cm axial distance from the torch because at very short distance such as 10 cm; there is a significant heat load that can damage the optical head. Therefore to overcome this problem, the plasma torch had to be placed at the longest possible distance from the collection optics. And in that case, the optical density filters had to be installed in front of the fiber tip as well in the lens tube to attenuate the intense radiation of the plasma.

The optical densities of the installed filters were 1.3 and 1.5 which provided an optical transmission of approximately 3 % and 5 % respectively. The blocking wavelength range was perfectly selected to be adequate to the responsivity of the CCD, and it was also consistent with the whole operating optical wavelength range of the detection system. All the elements in the system like the fiber optic, lenses, different filters, photodetectors and windows have been cautiously selected to provide a consistent optical transmission at the wavelength range of interest for this measurement.

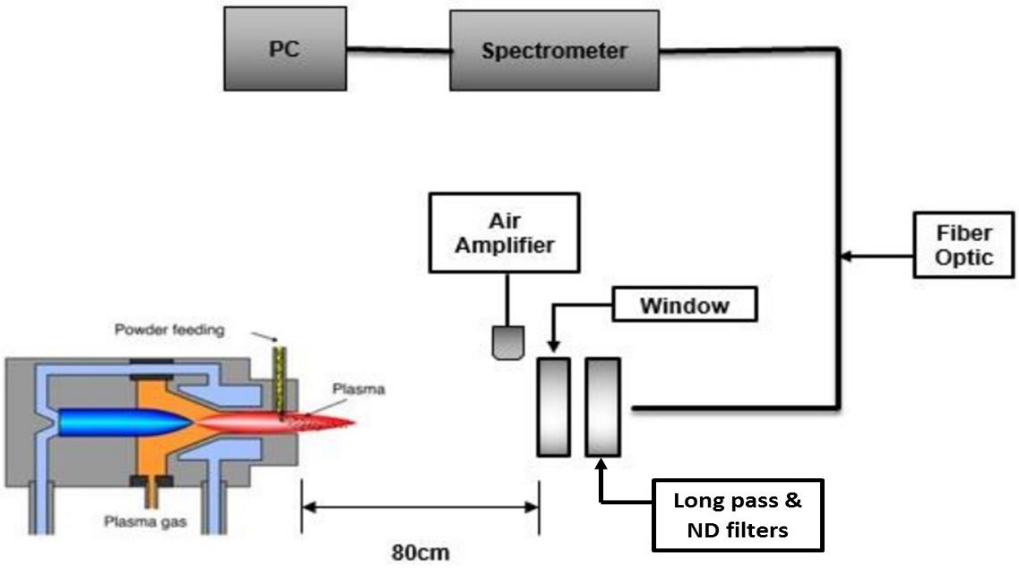

Figure 2-5: A schematic for the experimental setup of the front measurement.

Long pass filters at 500 nm and 600 nm were installed in front of the neutral density filters in the lens tube to block the second order diffracted wavelengths which might generate a misleading increase in the spectra and leads to an error in the measurement while collecting the spectra. Moreover, it was also necessary to avoid the intense radiation of the plasma in the UV range.

Finally, a BK7 glass window was fixed in front of the lens tube which contained the whole optical components to prevent any YSZ particles from sticking on the optical system. Additionally, a transverse air jet was used in front of the window to sweep any particles from sticking on the window and consequently blocking the field of view of the optical system. The presence of the window was taken into consideration in the calibration factor of the front and radial measurements.

2.1.3 Radial Measurement

A radial scanning at specific locations was carried out to the plasma jet while having the particles fed, and without feeding any particles as shown in Figure 2-6. Then, the spectra were collected to be analyzed. In order to have relatively good image to be projected on the fiber tip to be transmitted through the fiber to the spectrometer, an achromatic doublet lens AR coated with 40 mm focal

length to avoid the achromatic aberrations as much as possible was used. The optical transmission of the lens is from 650 nm to 1050 nm. The optical head was illustrated previously in Figure 2-4.

Another set of radial measurements were carried out according to the previously mentioned configuration. However, at this measurement the tackled axial distance was at 4 cm and 6 cm which are commonly used as stand-off distance in real applications. Moreover, only one optical component was changed in this setup which is the cut-off filter. This filter was used in addition to the same achromatic lens which was mentioned previously. The optical transmission of this filter was calibrated according to Figure 2-9.

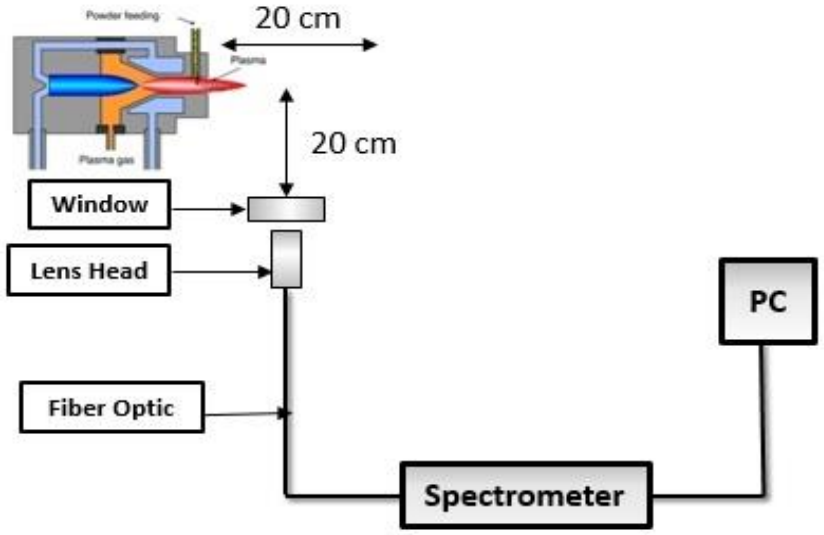

Figure 2-6: A schematic for the experimental setup for the radial measurement.

Figures 2-7 and 2-8 are illustrating the real configuration used in the lab during the experimental work. Very minor modifications were implemented that may diverge those photos to the real applied configuration.

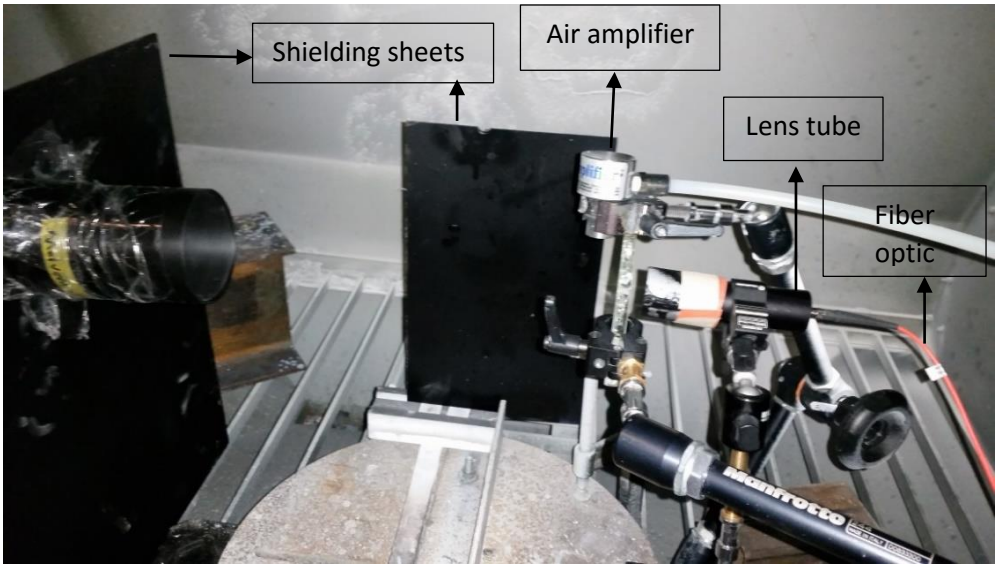

Figure 2-7: Real experimental set-up for radial measurements.

Figure 2-8 : Optical head configuration.

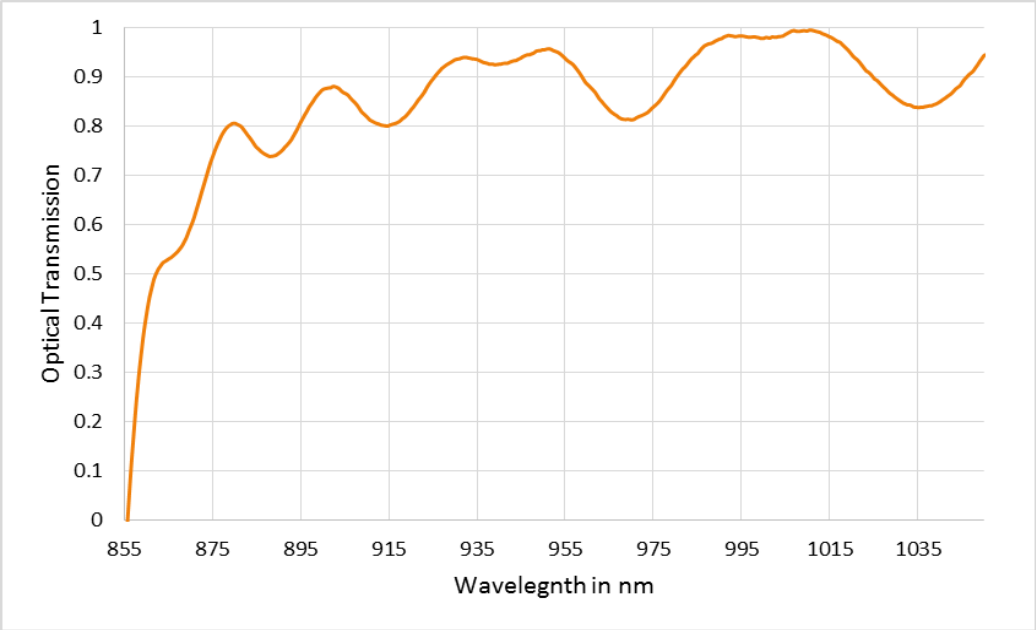

Figure 2-9: Optical transmission of 850 nm long pass filter as a function of wavelength.

The rest of the optical set up is similar to the front measurement. The same neutral density and long pass filters were used, in addition to the BK7 window. A transverse air jet from an air amplifier was used to prevent any particles from sticking on the window and blocking the field of view of the optical system. The axial distance scanned was from 20 cm to 4 cm from the plasma torch plan on measurement each 2 centimeters.

2.1.4 Radiometric Calibration for VIS/NIR range from 600 nm to 1100 nm

2.1.4.1 Radiometric calibration for the axial measurements

The spectrometer was radiometrically calibrated using a precalibrated light source with known emission at each wavelength associated with the responsivity of the Hamamatsu CCD camera (350 nm to 1100 nm). To do so, a Tungsten-Halogen calibration lamp equipped with the appropriate SMA connectors was used (AvaLight-HAL-CAL, Avantes). [25] The calibration is traceable to the National Institute of Standards and Technology. Figure 2-10 is illustrating the spectral irradiance of the lamp as a function of wavelength. [25]

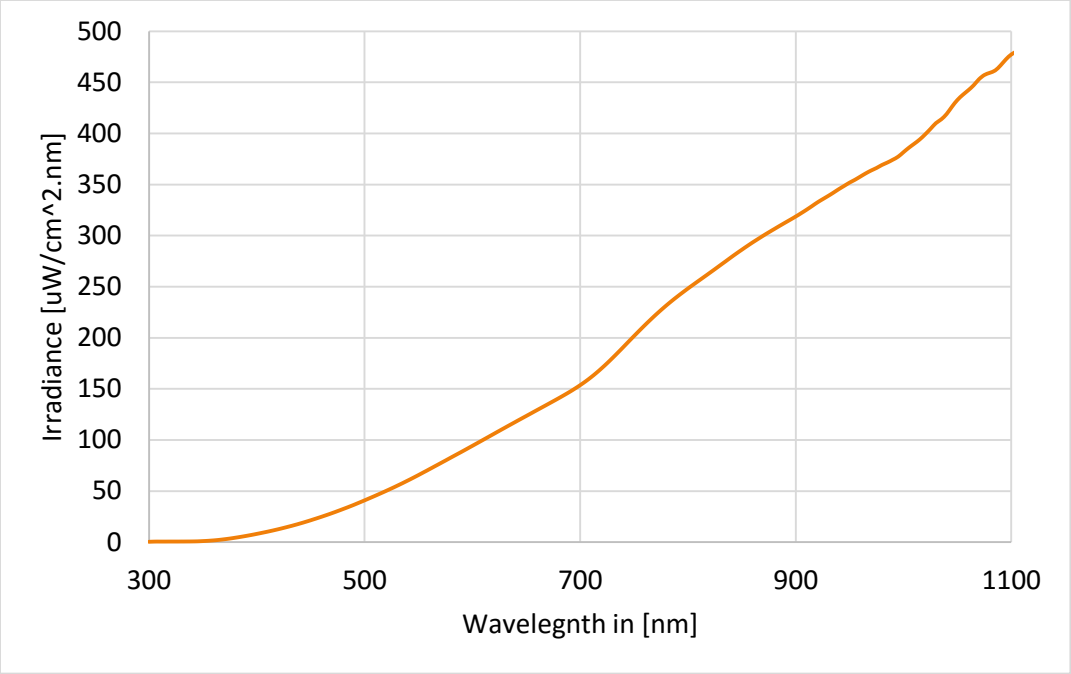

Figure 2-10: Irradiance of the calibration as a function of wavelength.

The calibration factor correlating the CCD counts of the spectrometer and the lamp intensity over the wavelength range was obtained as shown in Figure 2-11. In that calibration, the presence of the neutral density and the cut-off filters which have been used during the front measurements was taken into account. A detailed discussion about the purpose of using those filters during the front and radial measurements will be discussed in the following section.

The curve in Figure 2-11 shows that the acquisition system used during the measurement is having the lowest response in the interval of 850 nm to 1100 nm. To eliminate the effect of the second order diffracted wavelengths in the calibration factor; two cut-off filters were used to have a complete shut down below 600 nm. The cut-off wavelengths were 600 nm and 500 nm, and the reason to use two filters instead of one is because the 600 nm cut-off filter did not provide a complete shut down below 600 nm as depicted in Figure 2-12. Therefore, another 500 nm long pass filter was used to block all the radiation below 600 nm. Its optical transmission is illustrated in Figure 2-13. In addition, the neutral density filters were used to attenuate the signal during the

measurements from the front of the plasma torch. The optical transmission of those two filters is shown in Figure 2-14, 15 as a function of wavelength.

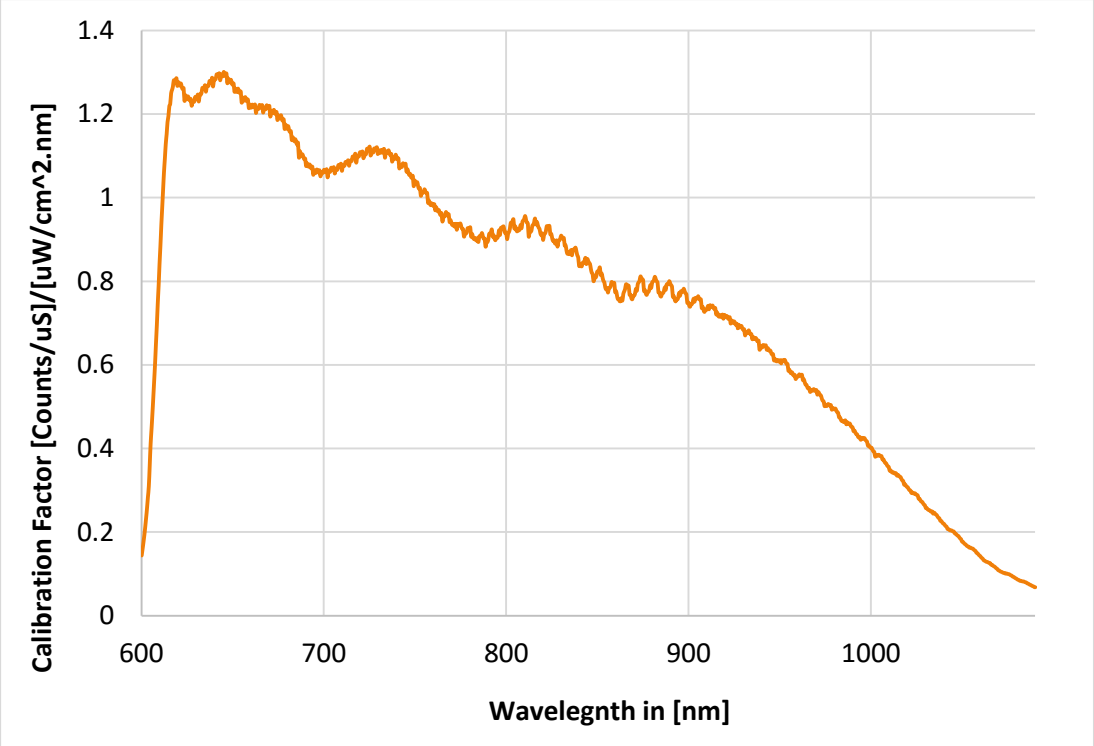

Figure 2-11: Silicon detector spectrometer's calibration factor as a function of wavelength.

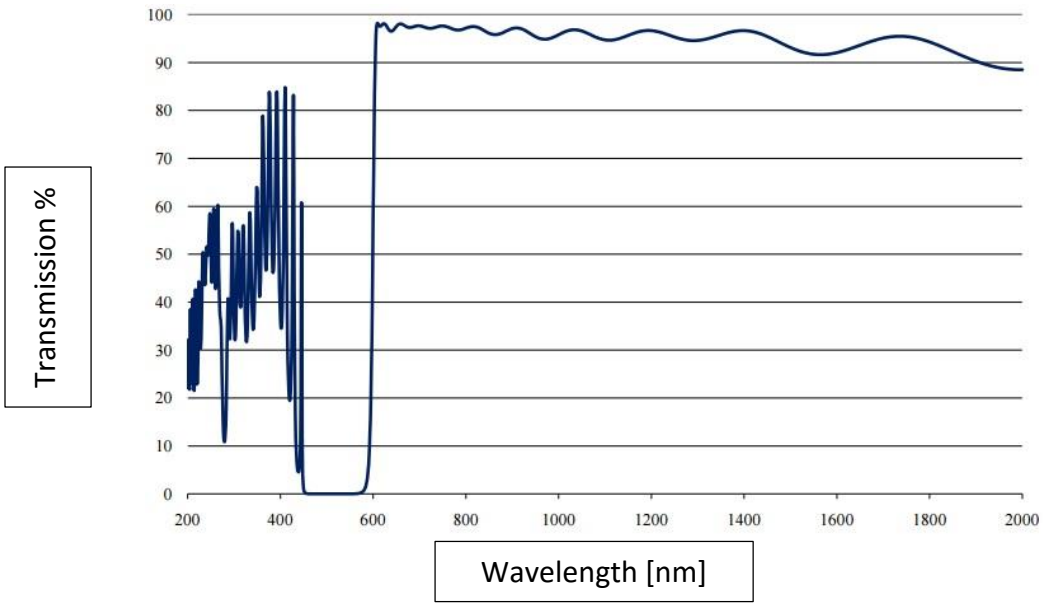

Figure 2-12: Optical transmission of 600 nm long pass filter as a function of wavelength.

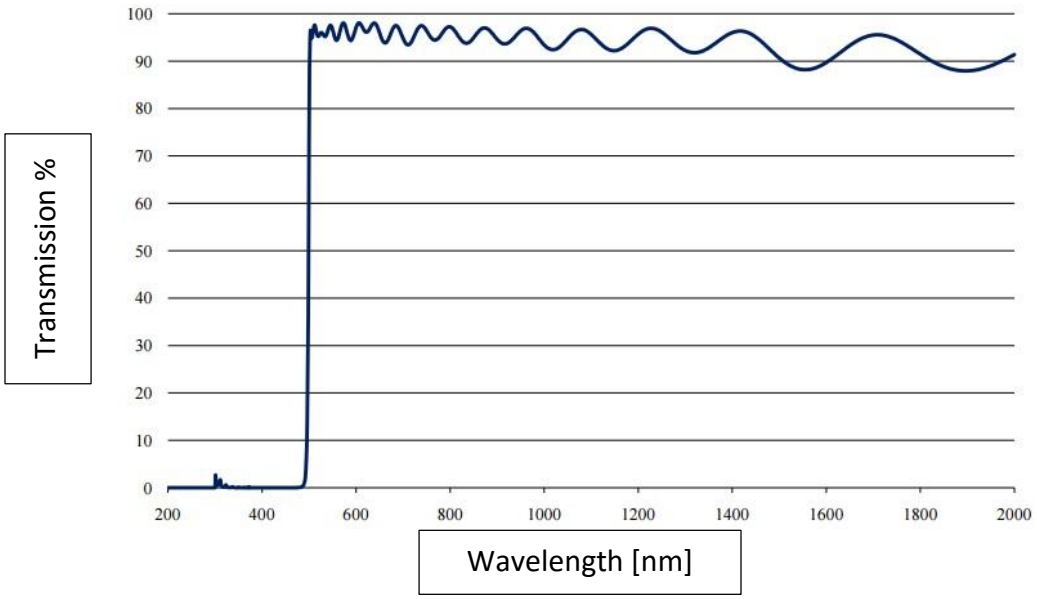

Figure 2-13: Optical transmission of 500 nm long pass filter as a function of wavelength.

Moreover, this calibration was carried out at 1000 acquisitions to obtain a reliable mean value of the spectrometer's output, and an exposure time of 6.06 ms in order to avoid any saturation for the CCD camera. Then, the collected data is transferred via FireWire/USB cable to a computer to be analyzed and treated.

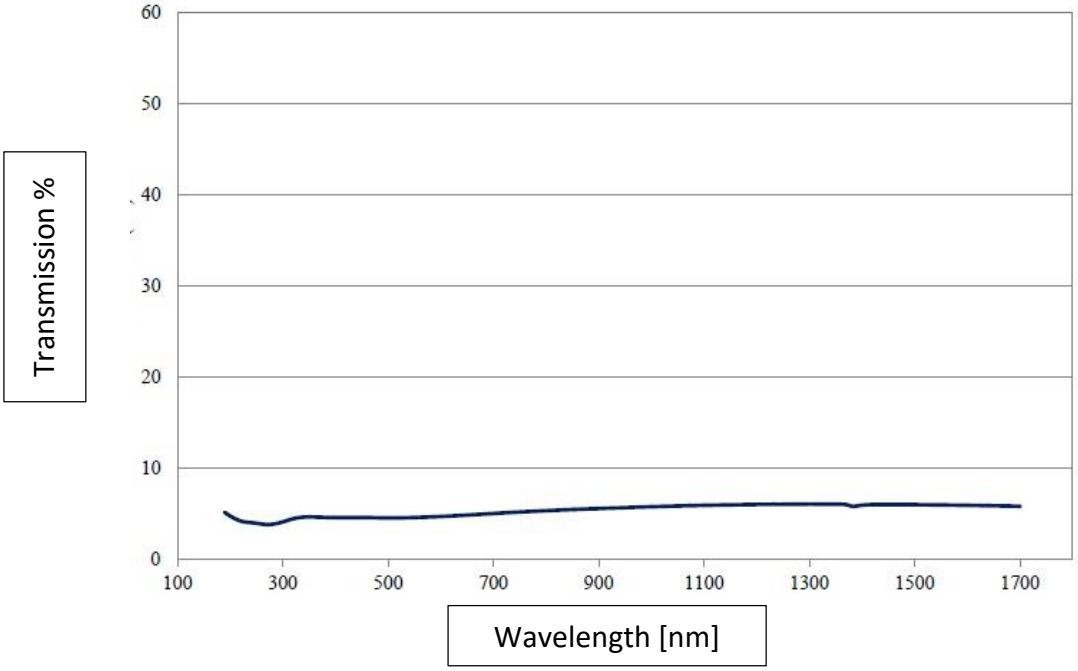

Figure 2-14: Optical transmission of OD 1.3 ND filter as a function of wavelength.

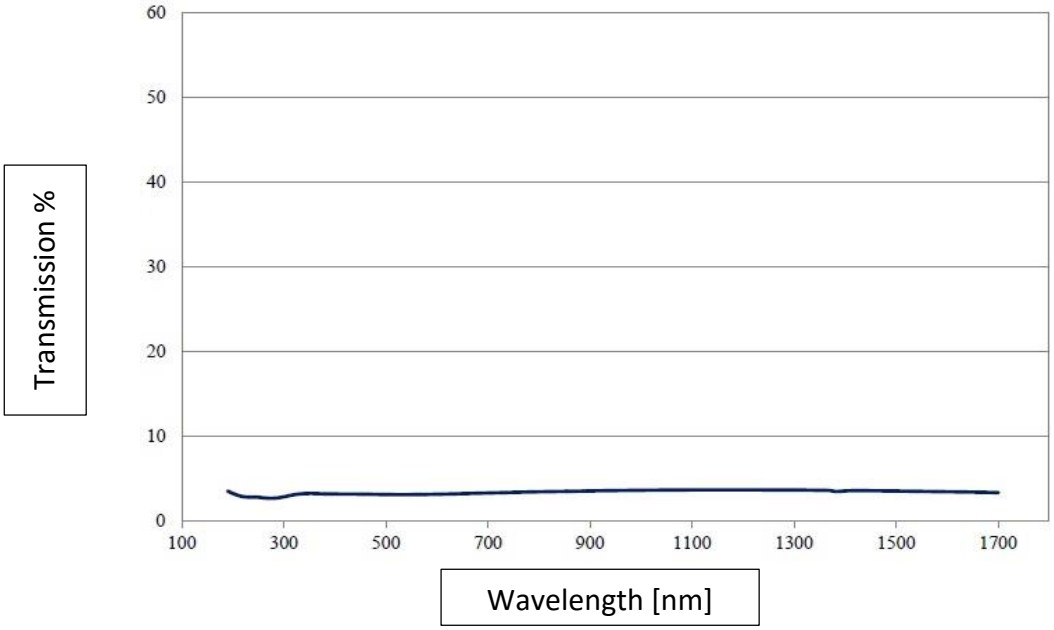

Figure 2-15: Optical transmission of OD 1.5 ND filter as a function of wavelength.

2.1.4.2 Radiometric calibration for the radial measurements

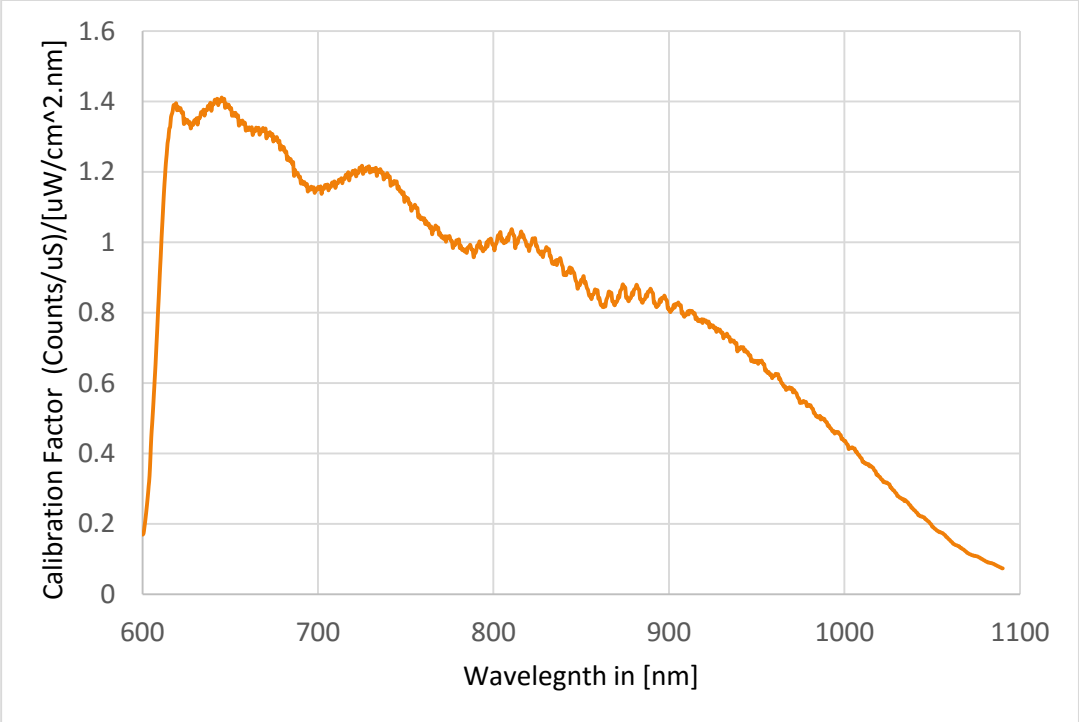

Figure 2-16: Silicon detector spectrometer's calibration factor as a function of wavelength.

In that calibration, the same source and methodology of the previous step were applied. However, the only one step signifies this measurement is the achromatic lens which was used during the radial measurement, and it was taken into account in order to have a precise calibration and close to the real measurement conditions. Figure 2-16 is illustrating this calibration factor as a function of wavelength.

2.2 NIR RANGE (1000 NM TO 2500 NM)

2.2.1 Optical and Acquisition System From 1000 nm to 2500 nm

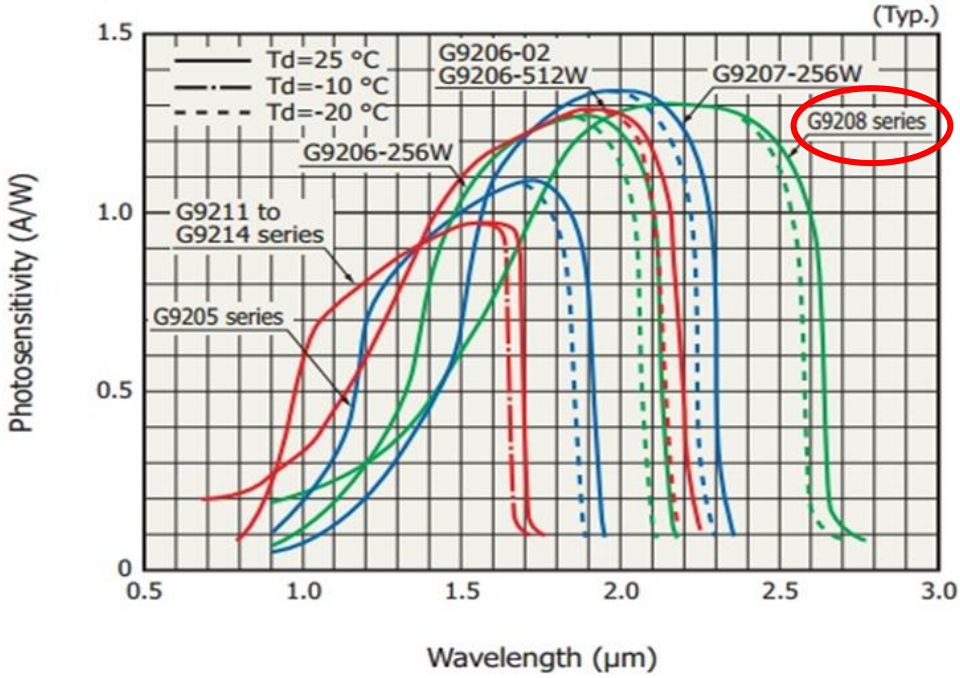

Figure 2-17: The photosensitivity of G9208-512-W Hamamatsu photodetector as a function of wavelength. .[23]

The measurements at this wavelength range were carried out using NIR Photon Control spectrometer equipped with InGaAs G9208-512-W Hamamatsu photodetectors. The spectrometer is coupled with SMA connectors to a fiber optic that has a numerical aperture of 0.22, and a core diameter 400 μm. The optical transmission of this fiber optic is adequate to the wavelength range of interest. The optical head design is schematically similar to the one illustrated previously in Figure 2-4.

The optical head used in this detection system contained a coated achromatic lens with optical transmission from 1050 nm to 2500 nm, and a cut-off filter at 850 nm to eliminate the second order diffracted wavelengths. In the same context in order to eliminate the second order diffracted wavelengths at the range from 1650 nm to 2500 nm, a cut-off filter at 1700 nm was mounted in front of the lens in the lens tube.

2.2.2 Radial Measurement for NIR Range From 1000 nm to 2500 nm

The plasma jet was radially scanned at that range with and without suspension at 4 cm and 6 cm. This axial distance was chosen because it is commonly as a stand-off distance for real spraying conditions in SPS. In addition, it is the minimum distance of possible detection to the thermal radiation of the particles as mentioned in the literature. The volume of measurement of the optical head is 1 mm. The signals were acquired two times. The first one was implemented while using 850 nm cut-off filter, and the second one was carried out while using 1700 nm cut-off filter. Figure 2-18, 19 are illustrating the configuration of this step.

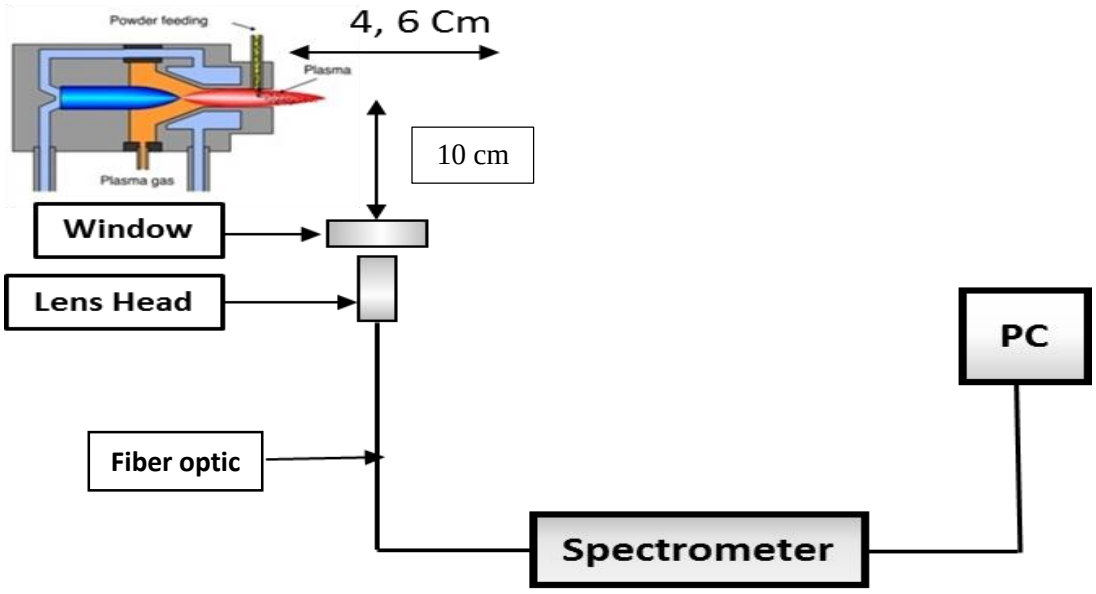

Figure 2-18: NIR range experimental setup schematic.

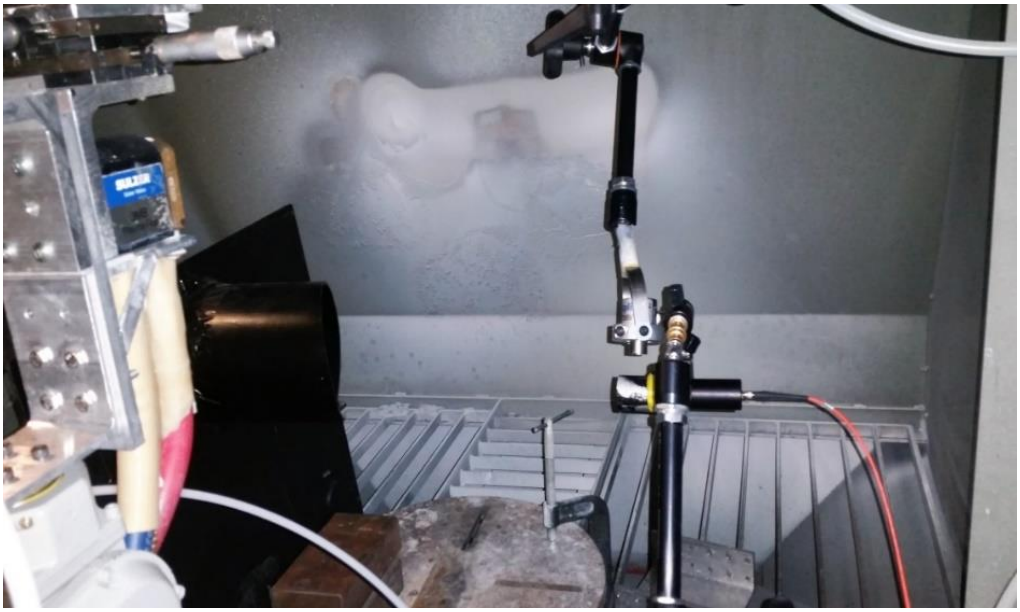

Figure 2-19: Radial measurement for NIR range from 1100 nm to 2500 nm.

2.2.3 Radiometric Calibration For 1000 nm to 2500 nm

The complete acquisition system was calibrated using Tungsten Halogen lamp from Avantes radiating at the wavelength range of interest. [25] The calibration lamp irradiance as a function of wavelength is shown in Figure 2-20.

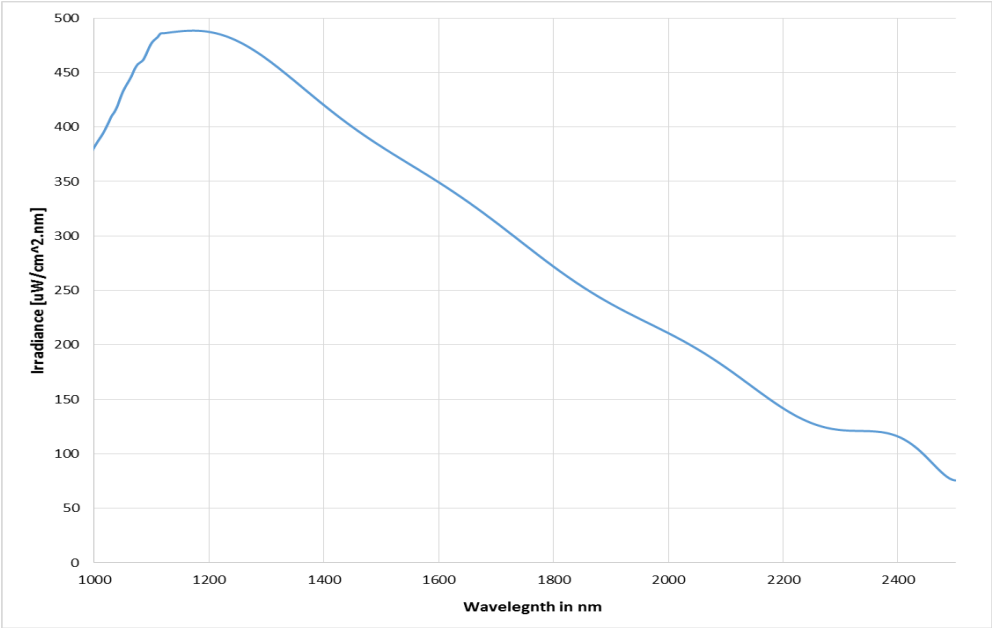

Figure 2-20: Irradiance of the calibration lamp as a function of wavelength in NIR range.

The calibration step was knocked down to two steps. Each one was carried out while using the appropriate filter. In other words, the first calibration was done while using the 850 nm cut-off filter, and the second one was carried out while using the 1700 nm cut-off filter. The calibration factor implied from 900 nm to 1600 nm is shown in Figure 2-21, and Figure 2-22 is illustrating the calibration factor used from 1600 nm to 2500 nm.

Generally, the calibration factors show a relatively low response at the range of 1 µm and below. This is attributed to the low detectivity of InGaAs G9208-512-W Hamamatsu photodetectors at that range. The response of this photodetector is peaked at the range from 1.9 µm to 2.5 µm as depicted in Figure 2-22.

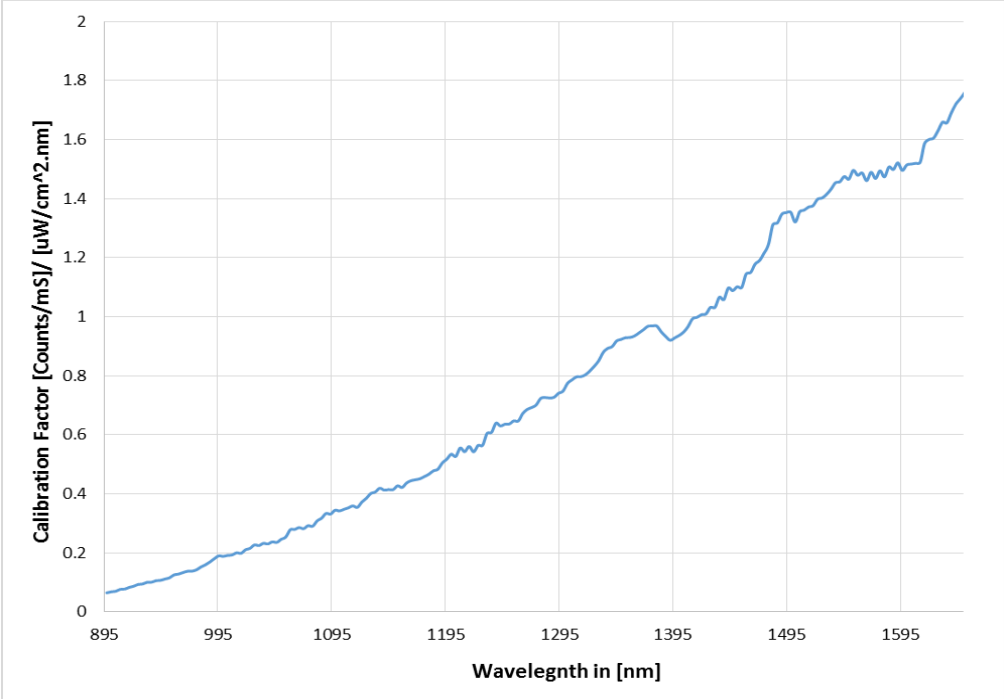

Figure 2-21: InGaAs detector spectrometer's calibration factor as a function of wavelength from 900 nm to 1600 nm.

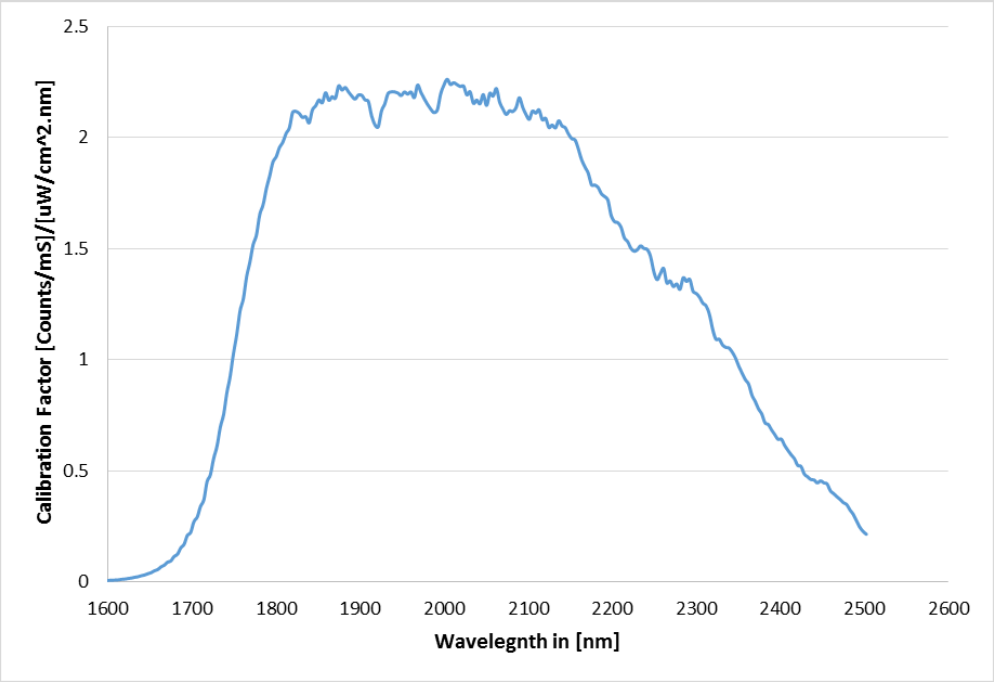

Figure 2-22: InGaAs detector spectrometer's calibration factor as a function of wavelength from 1600 nm to 2500 nm.

2.3 SPRAYING CONDITIONS

Table 2-1: Spraying conditions.

Argon Flow Rate	**30 NLM**
Helium Flow Rate	30 NLM
Suspension Flow Rate	10 g/min
Power	24 kW
Powder	YSZ
Powder Concentration	20 % wt.
Particle's Size	200 nm to 300 nm
Injector Diameter	200 um

The plasma torch used for this experiment is a 3MB Sulzer Metco. The suspension was injected radially at the exit of the plasma torch and the distance from the injecting point to the torch exit was adjusted to be at 25 mm. The spraying conditions were set to be according to Table 2-1.

The injection conditions of the YSZ suspension were adjusted to align the spray particle stream along the torch axis using Accuraspray G3C sensor (TECNAR Automation Ltd, Canada) [6], as it gives a very clear indication of the angle between the particles mean trajectory and plasma jet centerline.

Chapter 3

Results

3 RESULTS

The spectra were acquired from two different locations as mentioned earlier in the experimental setup. One measurement from the front is illustrated in Figure 2-5. The plasma was scanned with and without the particles at several axial locations 40, 60 and 80 cm from the plasma torch plane from the front direction. The other one was scanned radially with and without the particles at different points, as it was depicted Figure 2-6 with two different spectrometers.

3.1 AXIAL SPECTRA (600 NM : 1100 NM)

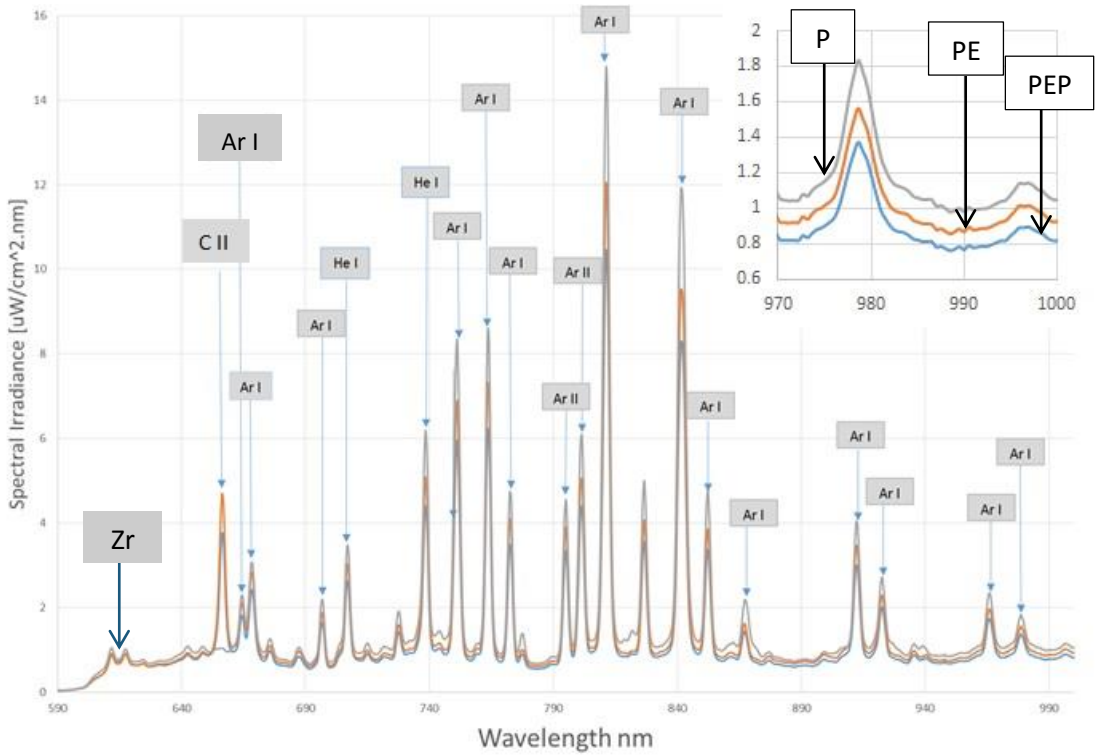

Figure 3-1: Spectra collected from the front at 80 cm from the plasma torch by the silicon detector spectrometer.

Figure 3-1 shows the spectra acquired from the front direction at 80 cm. This measurement was carried out using a bare fiber optic aligned directly in front of the plasma torch with a numerical aperture relatively large to collect all the generated radiation (NA = 0.22).

Cut-off filters at 500 nm and 600 nm were interposed at the optical head to block all the intense plasma radiation at the UV range and the second order diffracted waves as mentioned earlier. On the other hand, the number of acquisitions taken by the system at this distance was 1000.

Those acquisitions were averaged after subtracting the dark signal, and multiplied by the calibration factor. The UV range is not a matter of study because the thermal radiation generated from YSZ particles - if it was assumed that they are at the melting point (2700 °C) - is very weak at that range. The basic motivation to acquire the plasma radiation from the front is to assess the plasma radiation power density incident on the particles in order to calculate the plasma radiation scattered by those particles, and thus to investigate its influence on temperature measurement. The latter point will be presented explicitly in the next chapter.

In Figure 3-1, the spectra were acquired once for the plasma only (P), then for the plasma with ethanol (PE) and finally for the plasma with the ethanol and the particles (PEP). The atomic lines were identified, and they are traceable to NIST. [26] Most of the atomic lines in the three spectra detected by the system are generated from the plasma gases. They are attributed to the first and the second ionization states to Argon and Helium. After introducing the ethanol to the plasma jet, a carbon peak is detected at 656 nm. This peak is generated by the second ionization state of the carbon atoms. Furthermore, at 600 nm and 610 nm there are two new peaks seen in the PEP spectrum when the YSZ particles were introduced. Those peaks are emitted by *Zr* ions.

Globally, it can be realized that the atomic lines peaks are decreasing when the plasma is loaded with new elements, and the explanation formed for this observation is that when the suspension is fed to the plasma, it consumes a portion of its energy which leads to a decrease in its temperature. Consequently, the peaks are higher at the plasma only spectrum; it continuously decreases when ethanol is injected, and a final decrease when the suspension is fed. Figure 3-1 illustrates this observation.

Moreover, it reflects a drop in the number density of the different plasma ions, as their energy is transferred by collisions to the new constituents continuously added to the plasma jet.

In the same context, one can see that the continuum emission of the plasma decreases when the ethanol and ethanol/particles are injected into the plasma stream. This decrease in the radiation intensity can be attributed to a local decrease of the plasma bulk temperature when the ethanol and the suspension are injected, as these new constituents added to the stream consume a significant portion of the kinetic energy of the plasma during the collisions. Such an effect is commonly named as *the loading effect*.

Additionally, the suspension's streaks injected into the plasma jet at the exit of the torch may shadow a portion of the intense plasma emission regions located in the torch upstream the suspension injection location. Such a shadow effect would attenuate the plasma emissions as observed in Figure 3-1.

Figure 3-2 is illustrating an example for the bands generated by the molecular vibrations of the different constituents exist in the plasma volume. Those bands are repeated successively at different wavelengths in the continuum.

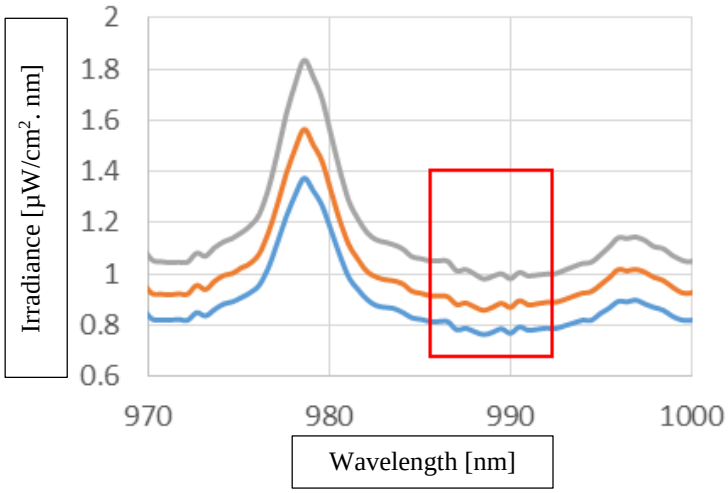

Figure 3-2: Molecular vibration bands as a function of wavelength.

Finally, the thermal radiation generated by the particles is not evident from this location of detection because of the dominant plasma radiation in the core of the plasma torch which is overwhelmingly intense and radiant compared to any other source of radiation in the field of view of the fiber optic.

3.2 RADIAL SPECTRA (600 NM : 1100 NM)

These set of measurements were carried out in order to detect the thermal radiation generated by the particles, and afterwards to calculate their temperature. As previously mentioned, the measurement sequence was knocked down to three stages. The first one was for the plasma only, secondly for the plasma with ethanol, and finally to the plasma stream after introducing the suspension. The axial locations which were investigated radially by the detection system were from 20 cm to 4 cm. The signal was acquired once each 2 cm. The number of acquisitions at each location was 1000. Those acquisitions were averaged after subtracting the dark signal, and multiplied by the calibration factor. Figure 2-11 is depicting the experimental set-up used at this step.

3.2.1 Spectra Acquired For The Plasma Only

Figure 3-3, 4 show the plasma radiation reflected in the booth and acquired by the system. A slight increase in the overall pattern of the spectra is observed when moving the torch from 20 cm to 8 cm. This is attributed to two reason. The first reason, when the torch is moving to a closer distance to the detection head, it was also close to the walls of the booth which will increase the power density of the radiation reflected by the booth walls and collected by the detection head.

This measurement is introducing a new non-thermal signal may affect the temperature measurement in small spraying booths. Though, a lot of cautious considerations were taken into account to decrease the influence of reflections by implying the required shielding and absorbing elements, the influence of reflections were inevitable. The second reason is that another portion of

the detected signal is attributed to the plasma radiation scattered by the particles at longer distance and collected by the optical head.

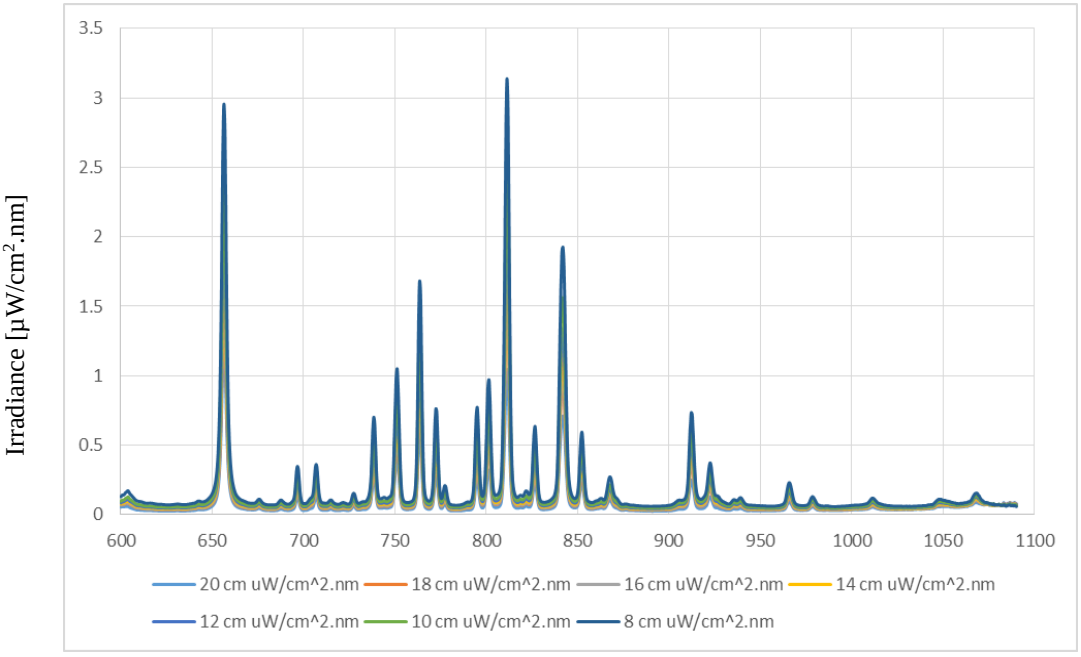

Figure 3-3: Plasma only spectra acquired radially by the silicon detector spectrometer at different locations as a function of wavelength.

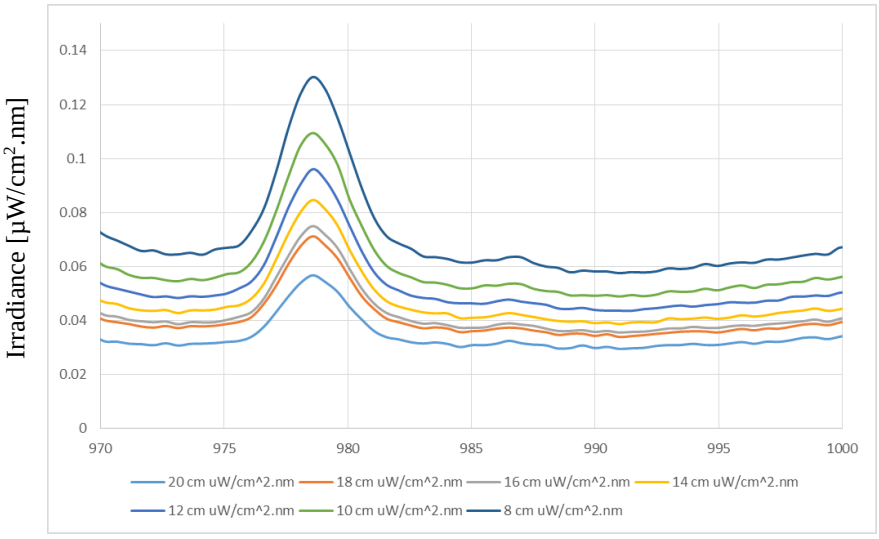

Figure 3-4: Plasma only spectra with different scaling as a function of wavelength.

3.2.2 Spectra Acquired for the Plasma with Ethanol

Similar to the previous discussion, the overall pattern of the spectra of the plasma with ethanol acquired at different locations and depicted below in Figure 3-5, 6 is increasing while moving the torch to a closer distance from the optical head and closer to the booth's walls as well. However, there is a slight difference compared to the plasma only spectra mentioned before in Figure 3-3.

At the NIR range from 1000 nm to 1100 nm illustrated below in Figure 3-6, the spectrum starts to increase at 1000 nm contrary to the plasma only reflections detected by the optical head. This increase is traced to the molecular vibration modes radiation bands of the ethanol which is evident at the NIR range. The vibration modes observed at that range is more likely to be stretching and bending modes as it was explained by Workman and Weyer. [27] Those vibrating molecules radiate photons at that range.

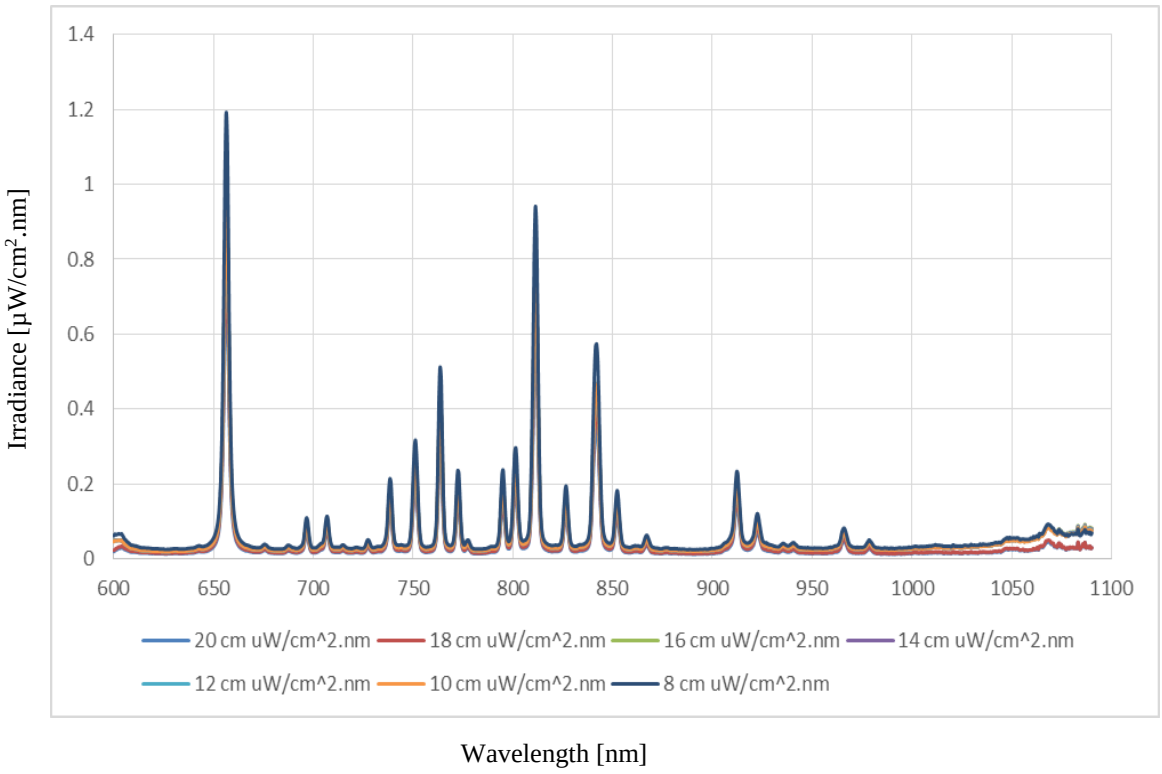

Figure 3-5: Plasma with ethanol spectra acquired radially by the silicon detector spectrometer as a function of wavelength at different locations.

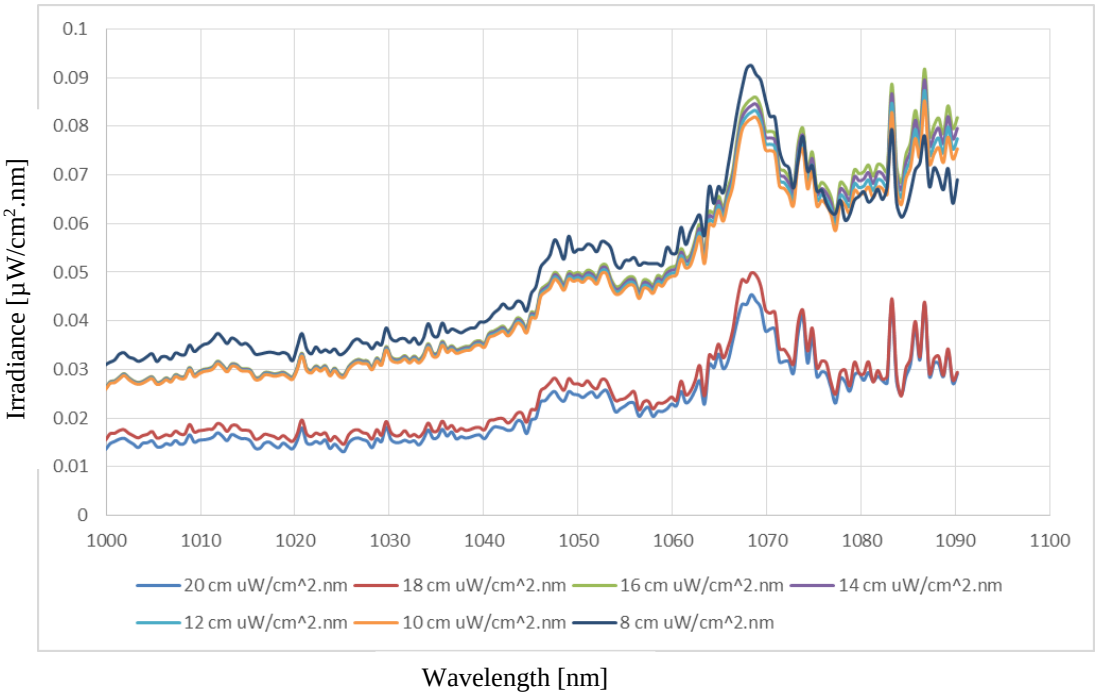

Figure 3-6: Plasma with ethanol spectra with different scaling as a function of wavelength.

3.2.3 Spectra Acquired from the Plasma with Suspension

When the suspension is introduced to the plasma jet, the thermal radiation of the particles started to be detected. At longer distances such as 20 cm and 18 cm, the thermal radiation generated by the particles is relatively low, as the particles are solidified and their temperature is decreased. The more the torch is moving closer to the optical head of detection, the more the radiation of the particles started to be detectable as illustrated in Figure 3-7.

The acquired spectra are significantly increasing while decreasing the distance between the optical head and the torch. From 20 cm to 12 cm, the detected signal is attributed partially to the reflections in the plasma booth, the radiation scattered by the particles, in addition to the thermal signal from the particles, and the increase in the continuum from one axial distance to another is relatively limited, also the thermal radiation generated by the particles at those distances are very low because they started to be relatively cold.

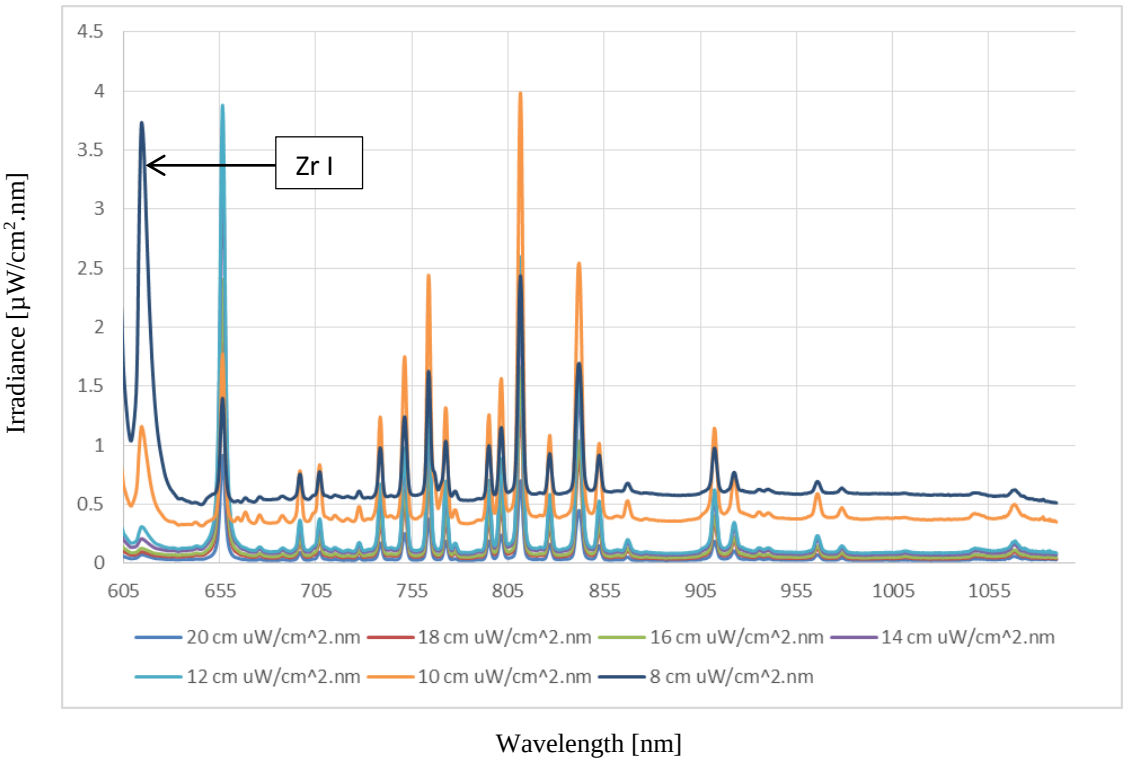

Figure 3-7: Plasma with suspension spectra acquired radially by the silicon detector spectrometer at different locations as a function of wavelength.

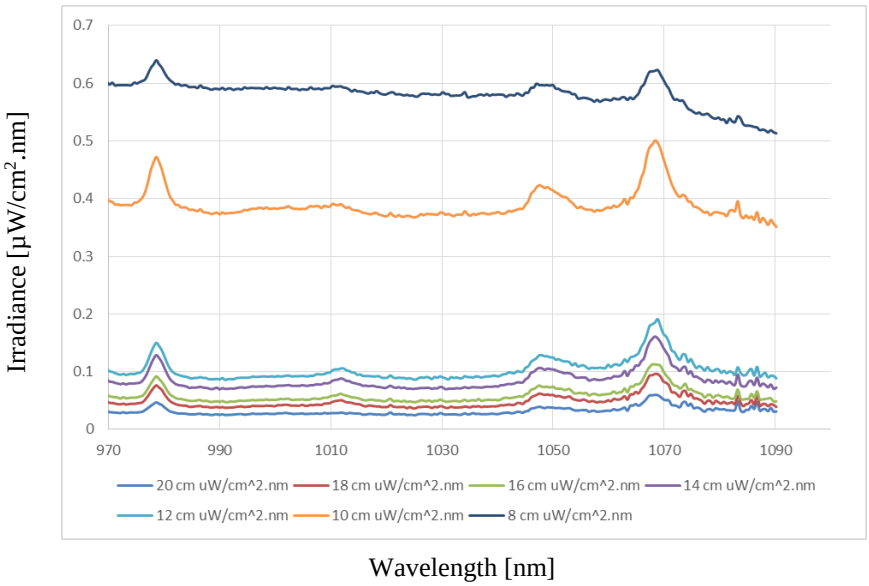

Figure 3-8: Plasma with suspension spectra with different scaling as a function of wavelength.

Moreover, the peaks and continuum tend to increase globally at closer distances. Figure 3-8 is depicting this understanding, as the spectra collected from 20 cm to 12 cm have close values in terms of the magnitude of the peaks and the continuum both tend to increase.

On the other side, the spectra collected at 10 cm and 8 cm have a significant increase in the continuum. The thermal signal at this region was more detectable compared the longer distances. Therefore, it was important to focus on those two spectra acquired at closer distances 10 cm and 8 cm.

Figure 3-9 illustrates a decrease in the zirconium peak as a function of distance from 10 cm to 8 cm. Also, the width of the peak is decreasing at while the distance increases, and this is attributed to the regression of lines at longer axial locations.

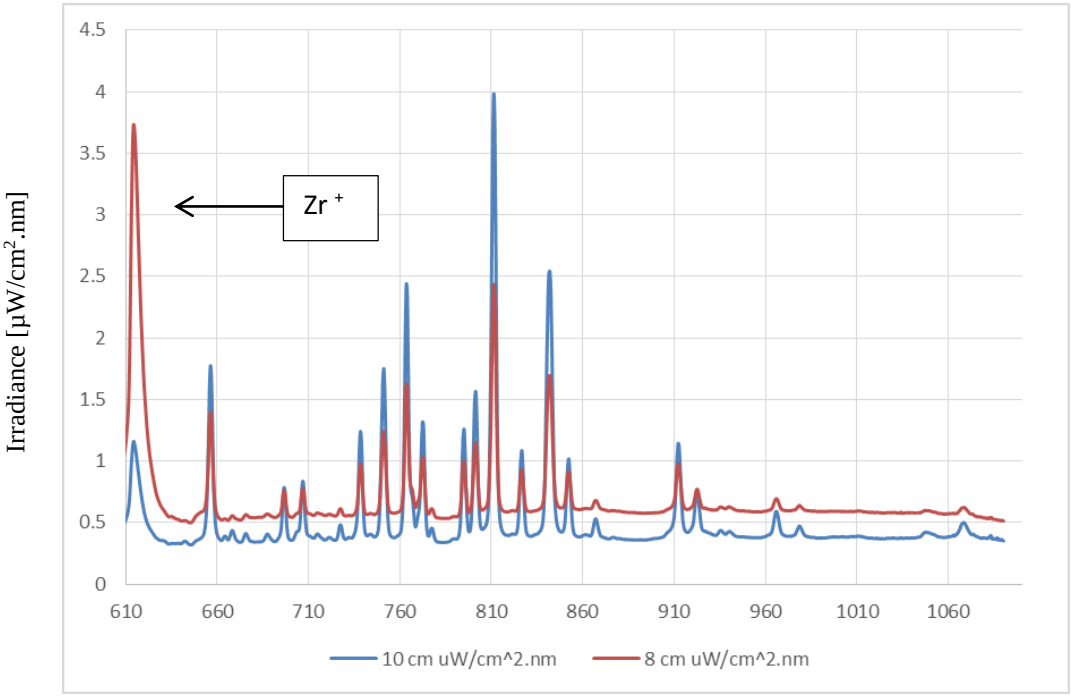

Figure 3-9: Spectra acquired at 10 cm and 8 cm by the silicon detector spectrometer as a function of wavelength.

3.2.4 Spectra Comparison at 8 cm and 10 cm

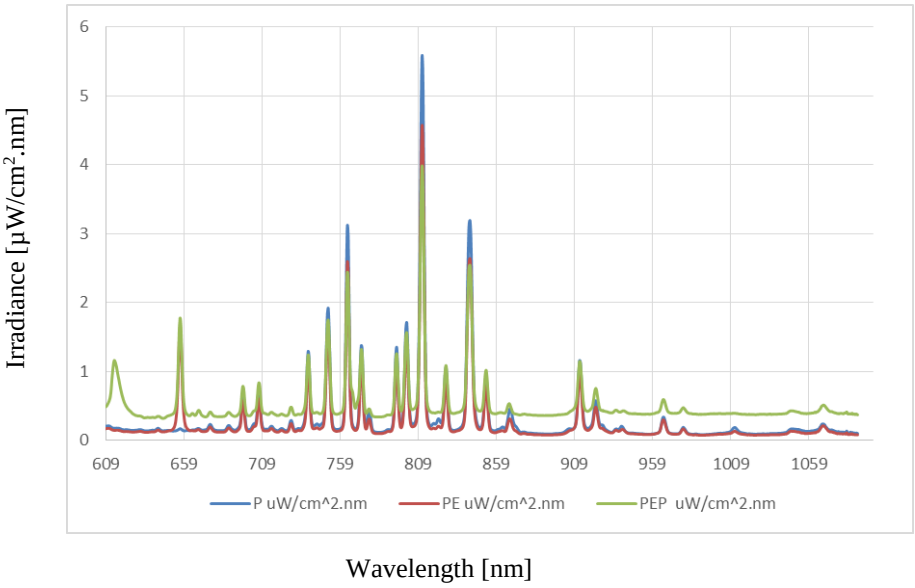

Figure 3-10: Total spectra comparison at 10 cm as a function of wavelength.

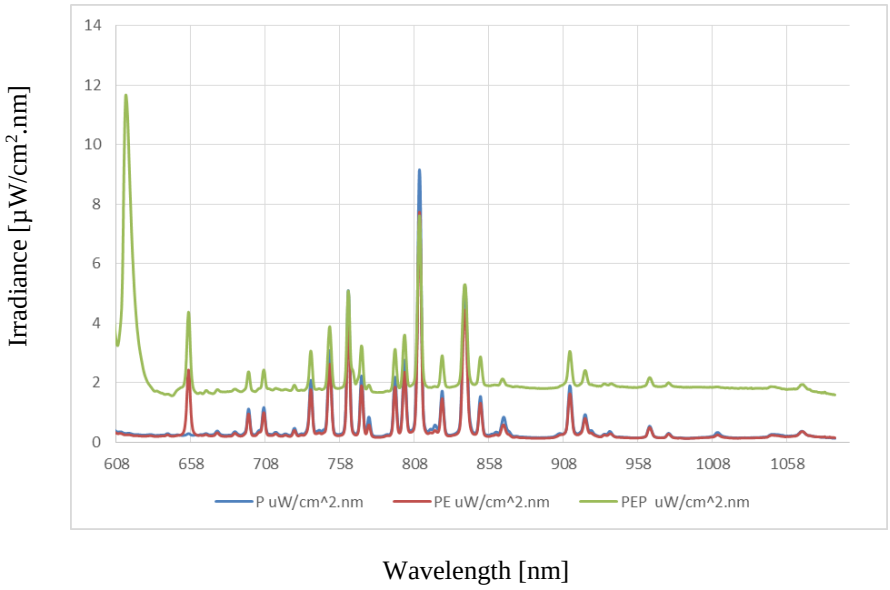

Figure 3-11: Total spectra comparison at 8 cm as a function of wavelength.

Figures 3-10, 11 represent a comparison between the two spectra acquired with and without the particles at 8 cm and 10 cm. When the ethanol was injected to the plasma volume, a carbon peak was detected at the spectrum at 658 nm; in addition to the *Zr* ions peaks at 614 nm.

The *Zr I* peak is increasing from 10 cm to 8 cm for the reasons advanced before. Indeed, as the required energy to ionize metallic atoms is relatively low as compared to plasma gases, the density of free electrons increases in presence of such metallic atoms that leads to an increase in the continuum background emission intensity.

3.2.5 Spectra Acquired at 4 cm and 6 cm

Figure 3-12, 13 illustrated the whole spectra from 600 nm to 1100 nm. The regions from 850 nm up to 1100 nm as shown in those spectra were quiet zones with minimal effect of the atomic lines. Therefore, the cut-off filter used at those measurements was positioned at 850 nm. Figures 3-12, 13 are illustrating those results, and they are showing very promising wavelength range of detection for the diagnostic sensors. The gain after introducing the particles is significant, while comparing the two spectra for the plasma with ethanol and the plasma with suspension.

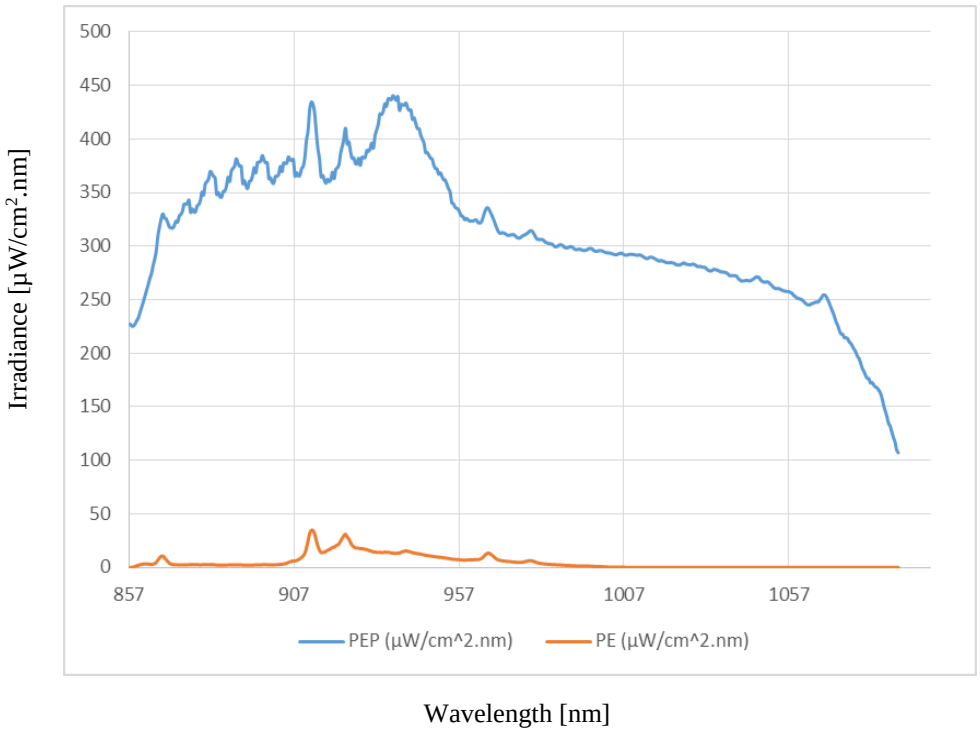

Figure 3-12: Spectra acquired at 4 cm by the silicon detector spectrometer as a function of wavelength.

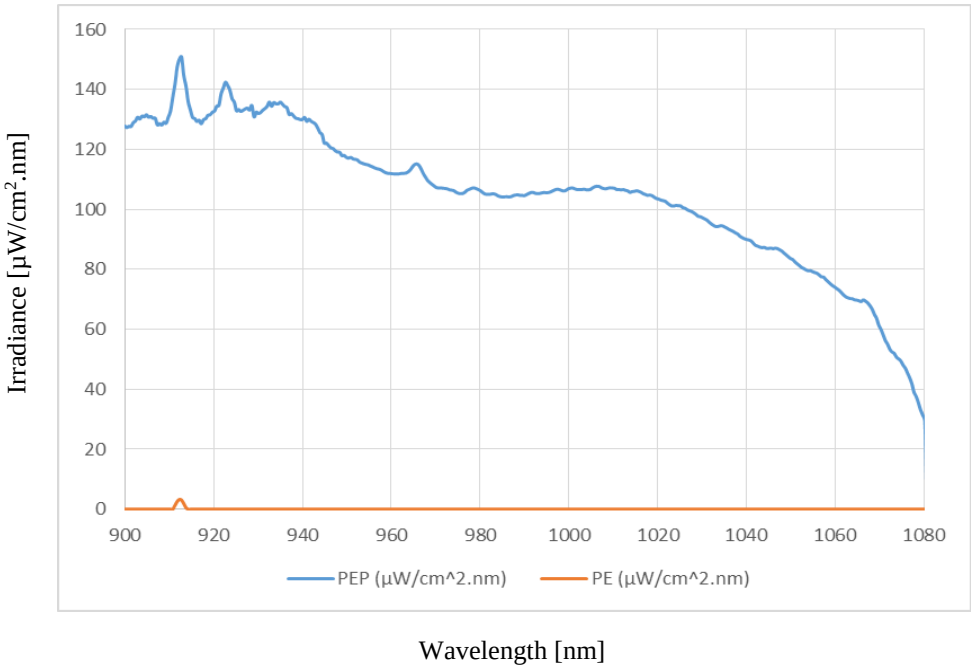

Figure 3-13: Spectra acquired at 6 cm by the silicon detector spectrometer as a function of wavelength.

3.2.6 *Zr* Vapors Presence as a Function of Distance

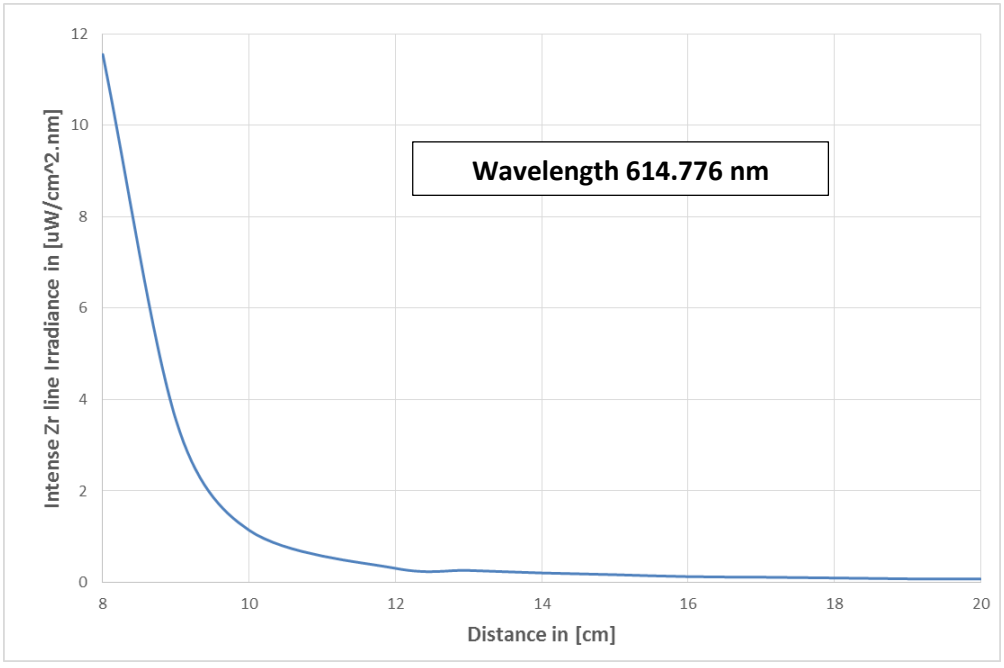

Figure 3-14: Zr vapor presence as a function of distance.

Zr emission lines appearing in the spectra resulted from the zirconium ionic vapors that existed around the center axe of spraying. By looking at the Zr^+ peak detected at different locations, it can be concluded that the presence of *Zr* vapors is increasing rapidly as a function of distance, while the torch is moving from 20 cm to 8 cm in front of the optical head. Figure 3-14 is depicting this behavior.

3.3 NIR RADIAL SPECTRA (900 NM: 2500 NM)

3.3.1 Spectrum Collected Using the First Cut-off Filter (850 nm)

Figure 3-15, 16 illustrate the spectra collected by Photon Control NIR spectrometer at 4 cm and 6 cm. The wavelength range of detection was from 1.1 µm to 1.7 µm. The field of view of the detection system was 1 mm. The optical transmission of the achromatic lens was from 1050 nm to 1700 nm, and a cut-off filter at 850 nm was interposed in front of lens to block the second order waves. In order to minimize the variation in sensitivity from one pixel to another the counts were averaged on two pixels to smoothen the curve. This precaution is advised by the manufacturer.

The detected signal decreased as a function of distance. The gain in the continuum with and without the particles is not significant compared to the spectra detected by the spectrometer equipped with silicon detector.

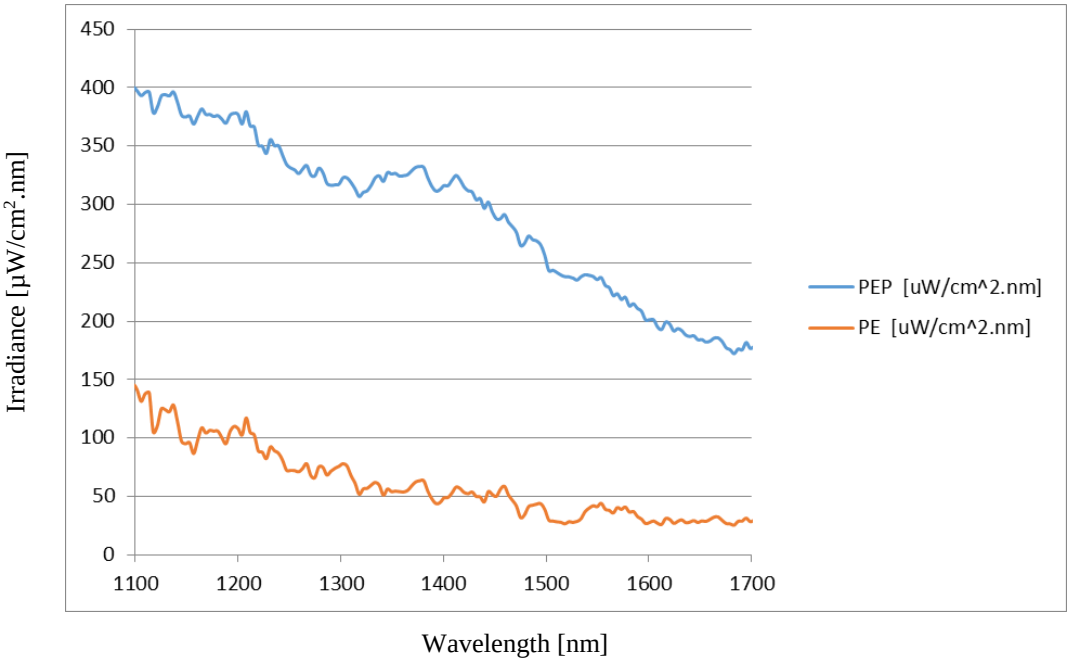

Figure 3-15: Spectra collected at 4 cm by InGaAs detector spectrometer as a function of wavelength.

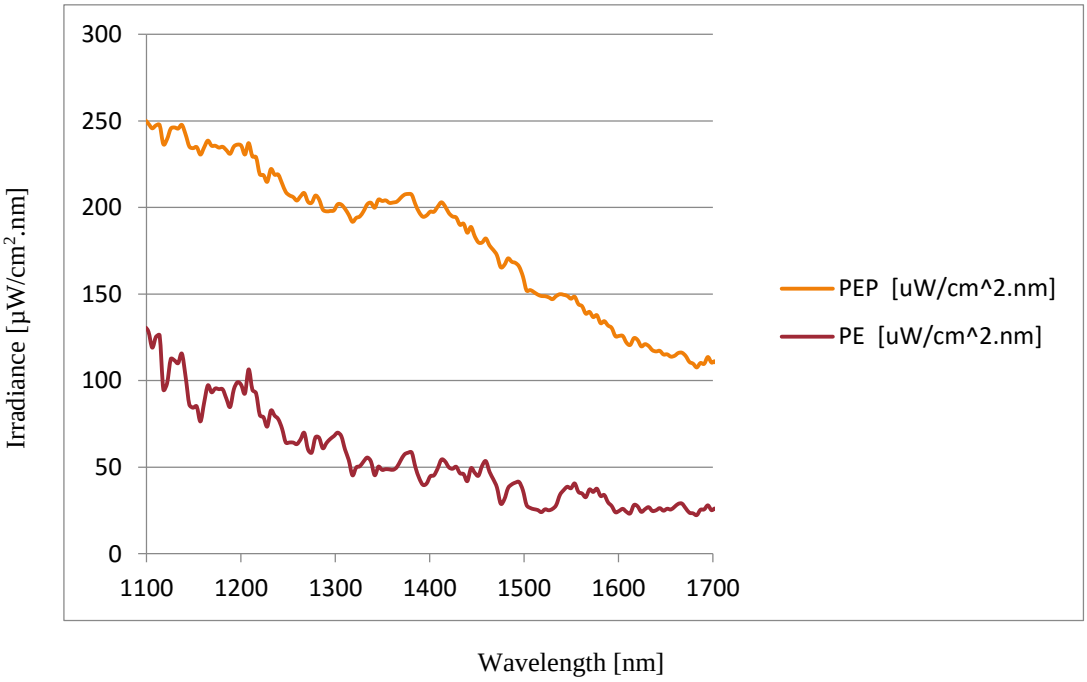

Figure 3-16: Spectra collected at 6 cm by InGaAs detector spectrometer as a function of wavelength.

3.3.2 Spectrum Collected Using the Second Cut-off Filter (1650 nm)

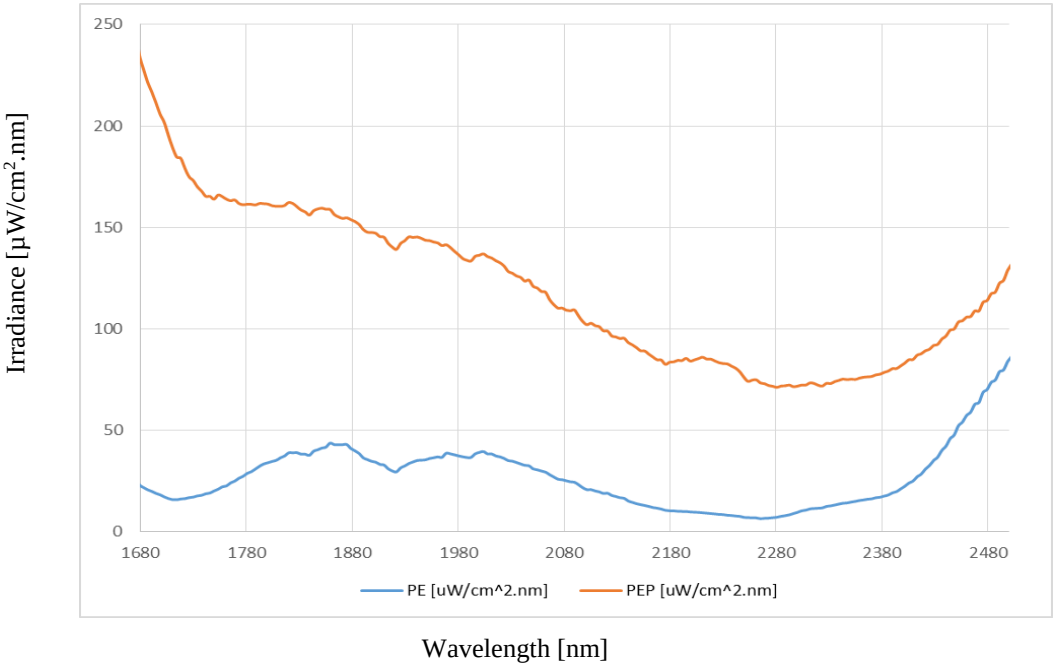

Figure 3-17: Spectra collected at 4 cm by InGaAs detector spectrometer as a function of wavelength.

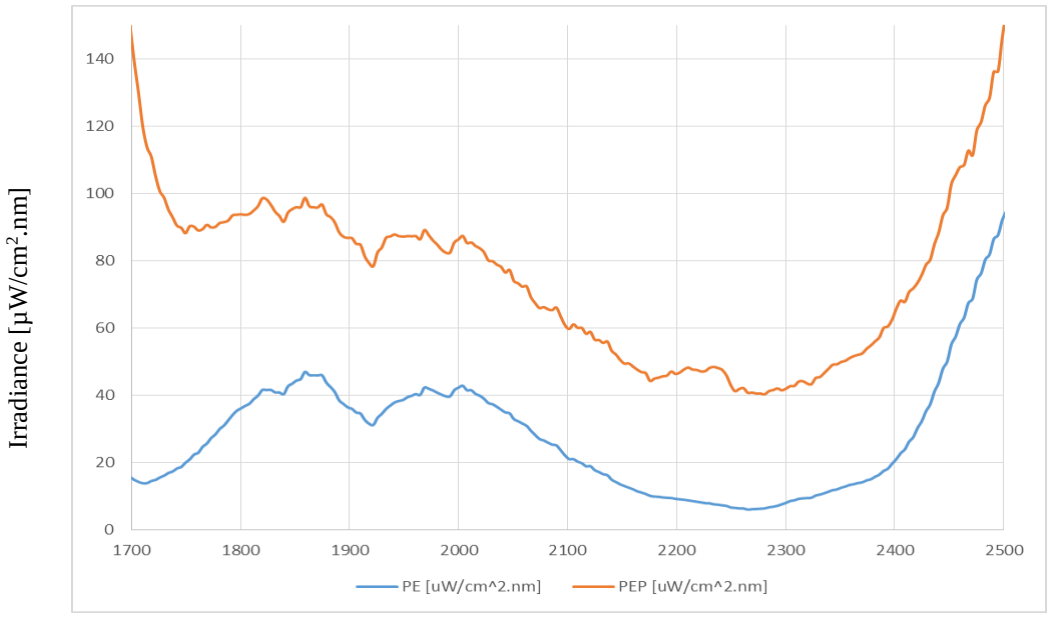

Figure 3-18 Spectra collected at 6 cm by InGaAs detector spectrometer as a function of wavelength.

Figure 3-17, 18 show the spectra detected at longer wavelength up to 2500 nm. The spectra at that range still show a significant influence for the plasma radiation which may perturb the temperature measurement process. The gain after introducing the particles from 1700 nm to 2000 nm is significant. Part of that is attributed to the thermal emissions directly detected from the particles and the other portion is related to the non-thermal signals present in the detected signal.

Chapter 4

Temperature measurement and future developments

4 TEMPERATURE MEASUREMENT AND FUTURE DEVELOPMENTS

According to the previous analysis to the collected spectra, it is reasonable to start to introduce the temperature measurement process. The precedent discussion in chapter 3 defined the road map for temperature measurement. In the literature view, several researchers used the two color pyrometer principle to measure the temperature of in-flight particles while assuming that they are behaving as grey body Eq. 1-2, 3. In other words, by assuming that their emissivity is constant as function of wavelength. This principle though it is not very accurate; however, it still provides a good approximation to the temperature of in-flight particles.

The temperature measurement process is relatively complicated and to reach 100 % confidence level needs a more detailed understanding to the physics of the process; this is attributed to the presence of the non-thermal signals in the field of view of the detection system. In that context, the approach considered in this study is measuring the temperature for a cloud of particles detected at the field of view by the optical head (approximately 1 mm^3).

One of the non-thermal signals affecting the temperature measurement of in-flight particles is related to the plasma radiation generated in the core of the plasma torch and scattered by the particles in-flight. In the next section, a detailed discussion will be presented to investigate the influence of this phenomenon on temperature measurement.

4.1 PLASMA RADIATION SCATTERED BY IN-FLIGHT PARTICLES

The plasma radiation scattered intensity by the in-flight particles can be calculated by knowing the incident power density on the particles. To do so firstly, the plasma plume which is the main and dominant source of radiation was considered to be a point source. Then to quantify the amount of the incident power density on the particles at the position of interest which is 10 and 8 cm far from

the plasma torch, the intensity of the plasma only was measured at different axial locations (80, 60, 40 and 20 cm) from the front direction to generate the corresponding attenuation factors relative to the intensity detected at 80 cm while moving from closer to longer distances. Furthermore, a second order polynomial was used to extrapolate the power incident on the particles at 10 and 8 cm.

The attenuation factors to the plasma radiation as a function of distance were calculated by taking the ratio between the intensity measured at a specific distance and the intensity measured at 80 cm for the three wavelengths of interest 995, 877 and 785 nm. It was important to develop such factors at each wavelength, as the plasma radiation power density increase as a function of distance was found to be wavelength dependent. Those three wavelengths were chosen because they are commonly used for the commercial diagnostic sensors.

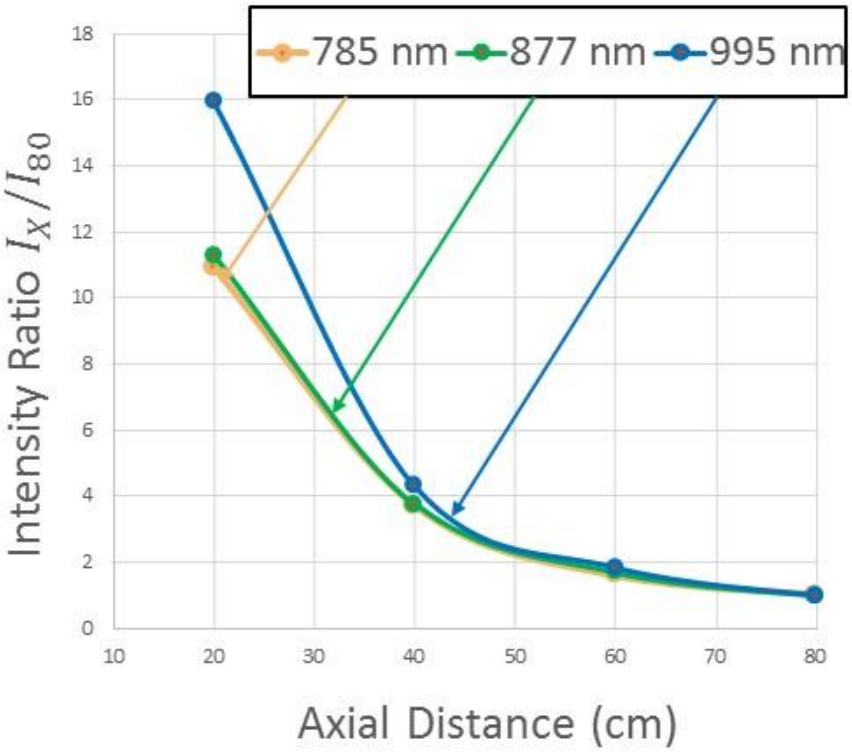

Figure 4-1: Intensity attenuation factors as a function of axial distance.

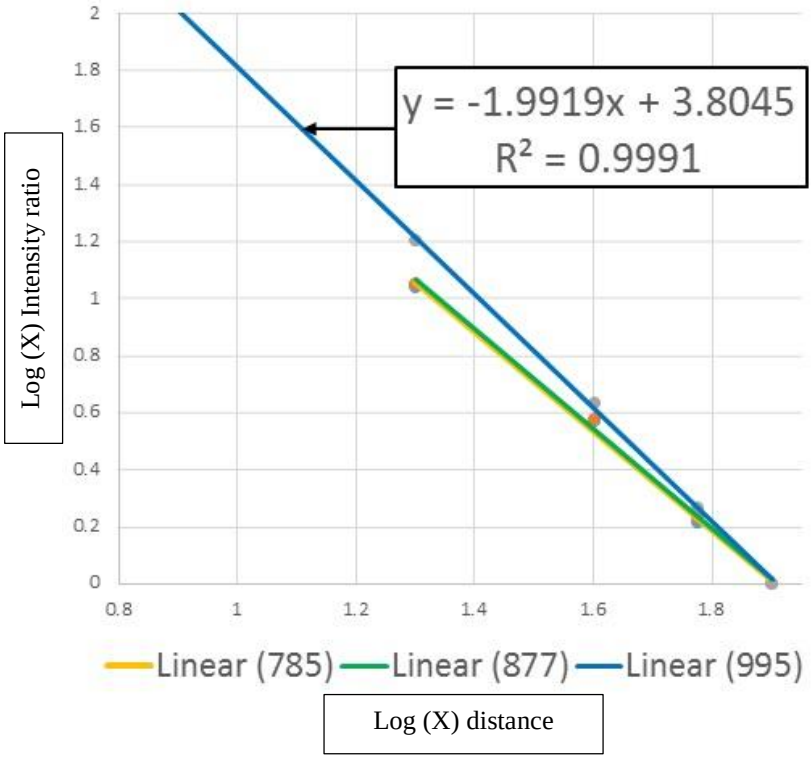

Figure 4-2: Log-Log scale to extrapolate the factors at 8 cm.

The developed factors were plotted as function of distance for each wavelength as illustrated in Figure 4-1. These factors were converted to a Log-Log scale to extrapolate the attenuation factors at the locations of interest which is 8 cm using a first order polynomial. Figure 4-2 is describing the conversion to a Log-Log scale, and the first order polynomial used to extrapolate the required values. The calculated factors were then multiplied by the spectrum collected at 80 cm. Table 4-1 is summarizing those factors.

Table 4-1: The implied factors at each wavelegnth and at different distances.

Distance in cm	785 nm	877 nm	995 nm
10	39	38	63
9	44	50	70
8	56	56	100

The scattered intensity of the reflected radiation described by Mie scattering is not isotropic and depends on the particle's size and the wavelength of the incident beam.[18] In the Mie solution, the

particles are considered to be perfectly spherical, and the medium surrounding the particles is assumed to be non-absorbing. The sphericity of the particles is a very valid assumption, as the molten particles are dominated by the surface tension forces because of their small size.

Therefore, the scattered radiation was calculated using Mie. Plot software at scattering angle of θ = 90° and λ = 785 nm, 877 nm and 995 nm. [31] The refractive index of YSZ particles was taken to be $n = 2.18 - 0.02i$. On the other side, the mean particle size distribution was taken to be 1.5 µm with 20 % standard deviation.

According to Mie solution, the scattered radiation at the three wavelengths of interest was calculated as a function of the scattering angle while assuming that the incident radiation is unpolarized. The scattered intensity at one wavelength as a function of the scattering angle is depicted in the following Figures 4-3, 4, 5 at 10 cm.

The value of scattered intensity was taken at 90 °. For two color pyrometer calculations, it is always important to consider a window while dealing with the signal and to ingrate over the whole band pass. Therefore, the scattered intensity was calculated over 785 nm ± 25, 877 nm ± 25 nm and 995 ± 25 nm.

Moreover, it was assumed that the factor between the power incident on the particles at the intermediate wavelength of each window, and the scattered intensity to be constant on the totality of the window. In other words, the ratio does not change from wavelength to another. The latter assumption was found to have minimal effect of the calculations, as we were more concerned with the order of magnitude rather than the exact number.

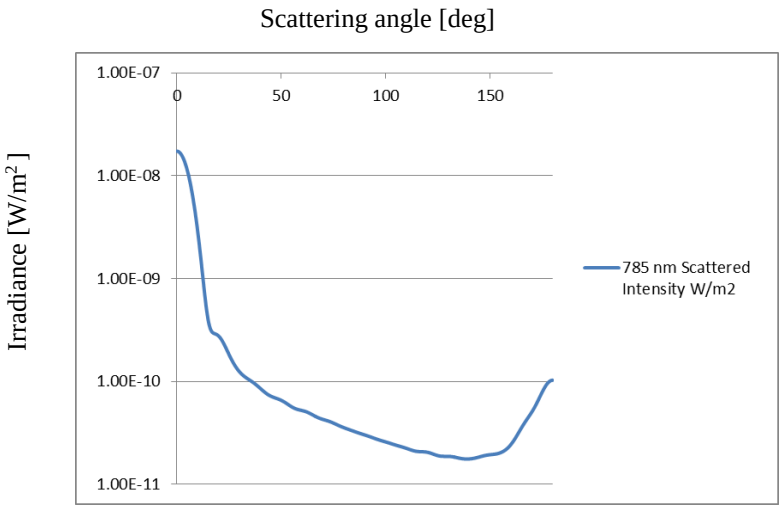

Figure 4-3: Scattered plasma radiation as a function of scattering angle at 10 cm and 785 nm.

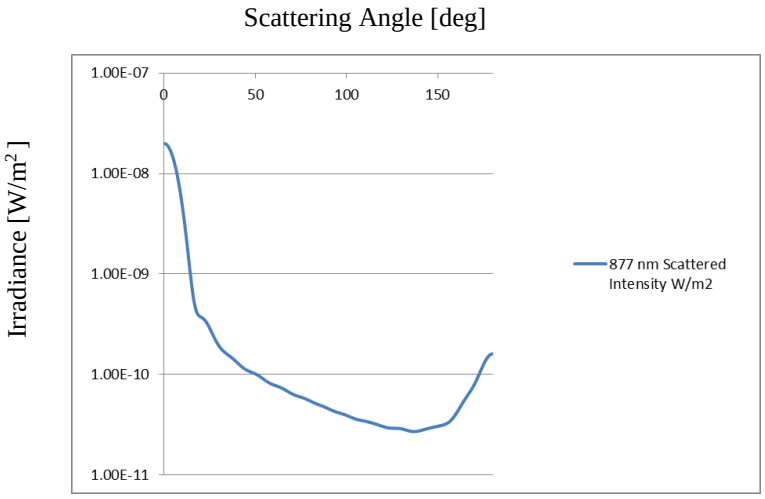

Figure 4-4: Scattered plasma radiation as a function of scattering angle at 10 cm and 877 nm.

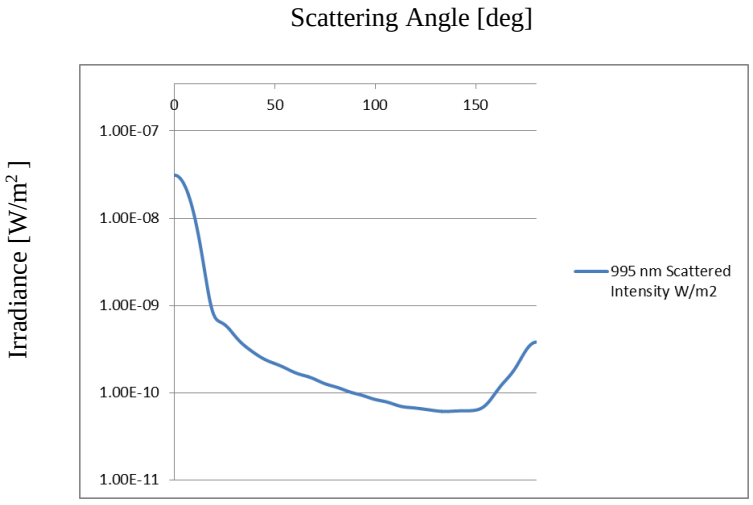

Figure 4-5 : Scattered plasma radiation as a function of scattering angle at 10 cm and 995 nm.

4.2 TWO-COLORS PYROMETER CALCULATION TO DETERMINE THE TEMPERATURE OF IN-FLIGHT PARTICLES

The temperature of in-flight particles can be obtained by taking the ratio between two intensities from the spectra collected radially, where the thermal radiation of the particles is detectable by the pyromteric system. Undoubtedly, the presence of the non-thermal signals still deviates the calculated values of the temperature from their exact values. However, the methodology followed in this research still provides a very good level of confidence to the temperature of the particles; particularly that the values obtained are consistent to the general understanding to the physics of the process and the location of detection.

$$T = \frac{C_2(\lambda_1 - \lambda_2)}{\lambda_1 \lambda_2} \cdot \left[ln\, R + 5\, ln \frac{\lambda_1}{\lambda_2} \right]^{-1} \qquad \textit{Equation 4-1}$$

$$R = \frac{I_{\lambda 1}}{I_{\lambda 2}} \qquad \textit{Equation 4-2}$$

The temperature of in-flight particles is a function of the ratio between the two integrals of intensities at two different wavelength ranges as mentioned in Eq. 4-1, 2. Figure 4-10, 11 are illustrating the total spectra collected at 8 cm and 10 cm from the radial direction. The ratio between the two integrals was calculated Eq. 4-2, and plugged into Eq. 4-1 after subtracting the reflections in the spraying booth.

The temperature of in-flight particles were calculated, and the results are mentioned in Table 4-3. The calculated temperature was decreasing as a function of distance increase as depicted in the table. These values are reasonable, as at 8 or 10 cm the particle's temperature should have been decreased, and they are most probably in a solidified state, and no longer at their melting point which is 2700 °C.

Another valuable remark is that while repositioning the windows integrated in the calculation from 995/785 ± 25 nm to 995/877 ± 25 nm, an increase in the temperature value was obtained. The values obtained at the latter windows are more reasonable and logical because at 995/785 ± 25 nm

there two peaks integrated at the windows which is considered as a non-thermal signal. Therefore, the temperature values calculated at 995/877 ± 25 nm were found to be more realistic.

Table 4-2: Temperature of in-flight particles as a function of distance.

	995/785 ± 25 nm	**995/877 ± 25 nm**
Particle's Temperature 8 cm °C	2396	2498
Particle's Temperature at 10 cm °C	2181	2183

4.3 SCATTERING EFFECT ON TEMPERATURE MEASUREMENT

In that section, it was important to assess the influence of plasma radiation scattered by the in-flight particles on temperature measurement. It was assumed that the particles are behaving as grey bodies and by implying the relation mentioned below in Eq. 4-3. Where; I_{em} is the intensity emitted by a black body in W/Sr, λ is the wavelength in m; T is the particle's surface temperature in K; C_1 = 9.352 x 10 $^{-17}$ W.m^2; C_2 = 1.439 x 10^{-2} m. K; and d is the diameter of the particle in m; ϵ is the emissivity of YSZ was assumed to equal to be 0.7 The influence of the emissivity variation (±) with the particle diameter is neglected in this work. The particles were assumed to be behaving as grey bodies, and their emissivity does not change as a function of wavelength and temperature.

The intensity radiated by a blackbody was calculated on a temperature range from 1100 °C to 2700 °C at two bands 995/785 ± 25 nm and 995/877 ± 25 nm. This step was carried out in order to obtain the intensity integral of the particle's radiation at the desired wavelength range.

$$I_{em}(\lambda, T) = \varepsilon \frac{C_1}{\lambda^5} d^5 \frac{1}{\{exp\frac{C_2}{\lambda T} - 1\}} d\lambda \qquad \textit{Equation 4-3}$$

The influence of plasma radiation scattered by in-flight particles was found to have no effect on the temperature measurement. As, the ratio between two intensities was considered according to Eq. 4-4.

$$R = \frac{I_{\lambda 1}}{I_{\lambda 2}} = \frac{I_{p\lambda 1} + I_{S\lambda 1} + I_{pS\lambda 1}}{I_{p\lambda 2} + I_{S\lambda 2} + I_{pS\lambda 2}} \qquad \textit{Equation 4-4}$$

Where; $I_{pS\lambda 1}$ represents the plasma radiation scattered by the particles, and $I_{p\lambda 1}$ is the thermal radiation directly generated by the particles, and they were assumed to be behaving as grey bodies. The influence of the plasma radiation scattered by the particles on temperature measurement was found to be negligible at the melting point of Zirconia.

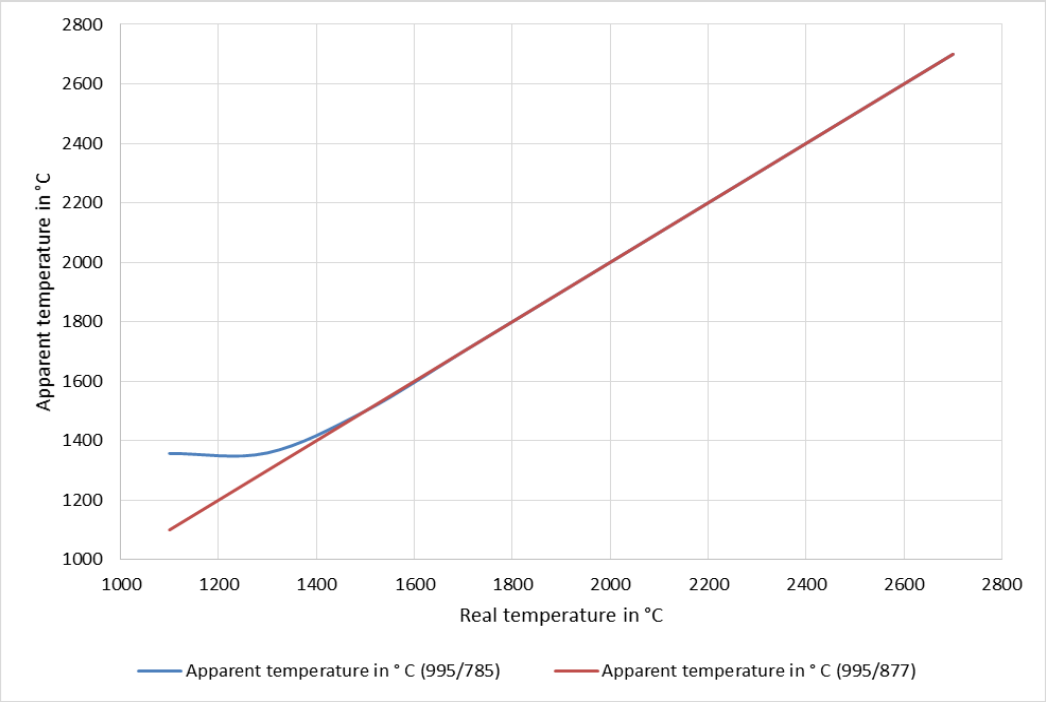

Figure 4-6: Real particle's surface temperature vs apparent particle's surface temperature in °C.

The error started to be considerable at 1300 °C, as it was calculated to be 59 °; while implying 995/785 ± 25 nm optical windows. Interestingly, if the two windows are positioned at 995/877 ± 25 nm the influence of the intensity scattered was found to be negligible on the whole temperature range even if at low temperatures. Figure 4-6 illustrates the true particle's temperature as function of the apparent temperature which depicts significant error on temperature measurement when the particles are at relatively cold conditions because of the scattering effect.

4.4 PLASMA RADIATION COMPARED TO THE PARTICLE'S THERMAL RADIATION

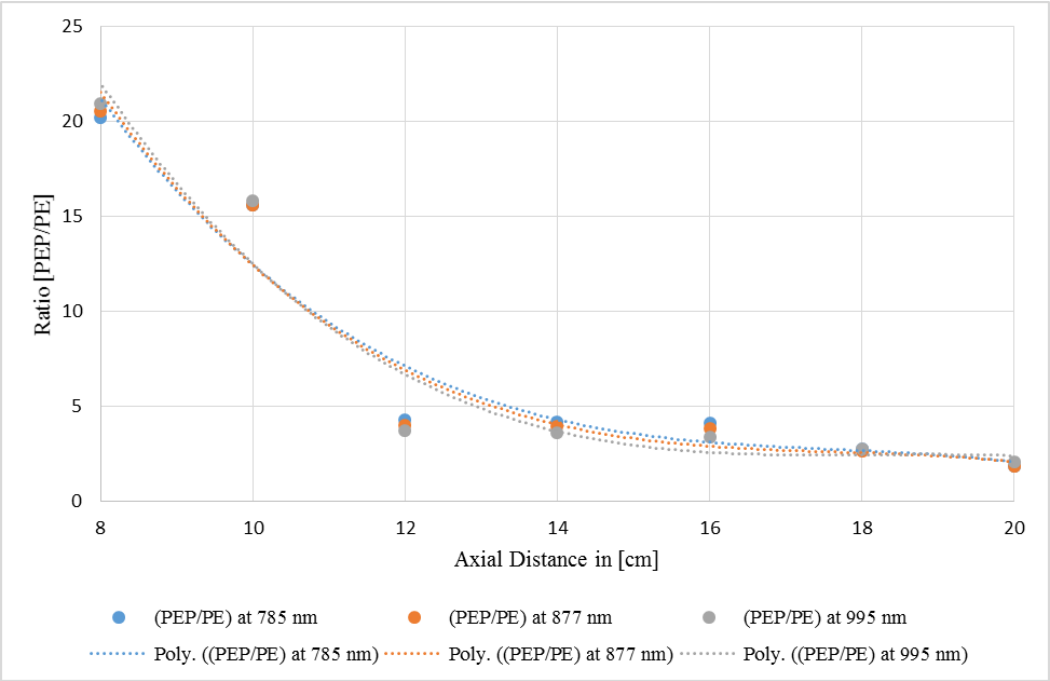

Figure 4-7: The ratio between PEP and PE as a function of distance to show the gain after introducing the particles to the plasma.

At 4 cm from the plasma torch which is most commonly used as a stand-off distance for spraying in SPS. The radiation of *Zr* particles was represented by a blackbody, so the peak should be around 1 µm. Therefore as depicted in Figure 3-12, the gain as a result of introducing the particles to the plasma is significant (PEP) spectrum compared to the plasma with ethanol (PE) spectrum while taking into consideration that the plasma conditions are changed when the particles are injected.

Figure 4-7 illustrates the ratio between the two signals obtained by the spectrometer at 3 different wavelengths 785, 877 and 995 nm. The first signal represents the power density collected by the detection system for the plasma with suspension spectrum [PEP], and the second signal represents the plasma with ethanol [PE]. The developed ratios illustrate a significant gain at shorter distances which favors better positioning to the optical head at shorter distance to the plasma torch because of the more thermal radiation detected from the particles.

4.5 SENSITIVITY ANALYSIS

Table 4-2 shows a steep temperature gradient as a function of distance. Positioning the two optical bands at 995/877 ± 25 nm gives more reasonable values for temperature measurement compared to 995/785 ± 25 nm because of the presence of atomic lines at the latter window. The obtained temperature values shows a temperature gradient with 15 degrees/mm while assuming a linear decrease. The temperature gradient in SPS is higher compared to APS. As in air plasma spray the temperature gradient can reach 50 degrees/cm. [1]

Therefore at 3 mm distance far from the point of detection, the temperature is expected to decrease with 45 degrees. The separation between two points of detection with a certain distance to filter the two wavelengths was made according to the current optical design of the Accuraspray which adopts the filtration of the two colors at two different location separated by a certain distance almost 3 mm.[1] The relative intensity of 1.5 µm *Zr* particle diameter with the same optical properties mentioned previously in Ch. 4.3 is calculated at the two different locations while changing the wavelength, and taking into consideration the effect of thermal gradient. Table 4-3 shows the results of those calculations;

Table 4-3: The intensity of 1.5 µm Zr particle at different wavelengths calculated at two different locations 8 cm and 8.3 cm

Wavelength in [nm]	**Intensity at 8 cm (2500 °C) in [W/Sr]**	**Intensity at 8.3 cm (2455 °C) in [W/Sr]**
785 nm	0.95	0.85
877 nm	1.095	0.98
995 nm	1.17	1.07

The ratio between the two intensities at two different colors at the same location (8 cm) is 1.07 (995/877) and 1.23 at (995/785). However if the two colors are filtered at two different locations,

the effect of the thermal gradient on temperature measurement in SPS becomes very significant. If it was assumed that the optical window is positioned at (λ_1 = 995)/ (λ_2 = 877), then the calculated temperature using Eq. 4-1 was 2407 ° K, if λ_1 was in the hotter location. Also, the error in the obtained value is quantified to be -246 °. On the other hand, if λ_2 was in the hotter location the calculated temperature was 3200 ° K, and the error in the obtained value is quantified to be +547 °.

In the same context, if we assumed that the optical window was positioned at (λ_1 = 995)/ (λ_2 = 785), then the calculated temperature using Eq. 4-1 if λ_1 was in the hotter location was 2571° K, and the error in the obtained value is quantified to be -82 °. On the other hand, if λ2 was in the hotter location the calculated temperature was 2966 ° K, and the error in the obtained value is quantified to be +313°.

Table 4-4: Error in temperature measurement because of the effect of the thermal gradient on the filtration of the two colors

	(λ_1 = 995)/(λ_2 = 877)	**(λ_1 = 995)/(λ_2 = 785)**
Δ T (λ_1 in the hotter location)	-246°	-82°
Δ T (λ_2 in the hotter location)	+547°	+313°

In that reflection, In APS filtering the two colors at two different locations seems to be reasonable because the particles are relatively large, and they do not lose their temperature rapidly as a function of distance. The thermal gradient is around 50 degrees/cm. [1] However in SPS, the thermal gradient is steeper. Therefore, the probability to have a bias in temperature measurement because of this phenomenon increases. In that sense, it is more rational to filter the two colors at one location.

4.6 FUTURE DEVELOPMENT

The current optical configuration to the Accuraspray sensor is not ideal because of the separation between the two signals detected by a certain distance. Therefore, the two thermal signals at the two different wavelengths are filtered at two different temperatures for the particles which will lead

to significant error in temperature measurement, as the particles are relatively small in SPS, and they will lose their heat energy very quickly as function of distance as mentioned in the previous section.

Figure 4-8 illustrates a configuration designed before by Bourque et al. This design is more appropriate compared to the current configuration, as the filtration of the two colors is carried out at the same location of detection. Therefore, it gives a better confidence for the obtained values. The signal detected by the first optical fiber [1] is split into two signals, and then filtered at two different colors by two filters F1 and F2. Consequently, these two signals are transmitted to a computer for fast two color pyrometer calculations to obtain the temperature. [14]

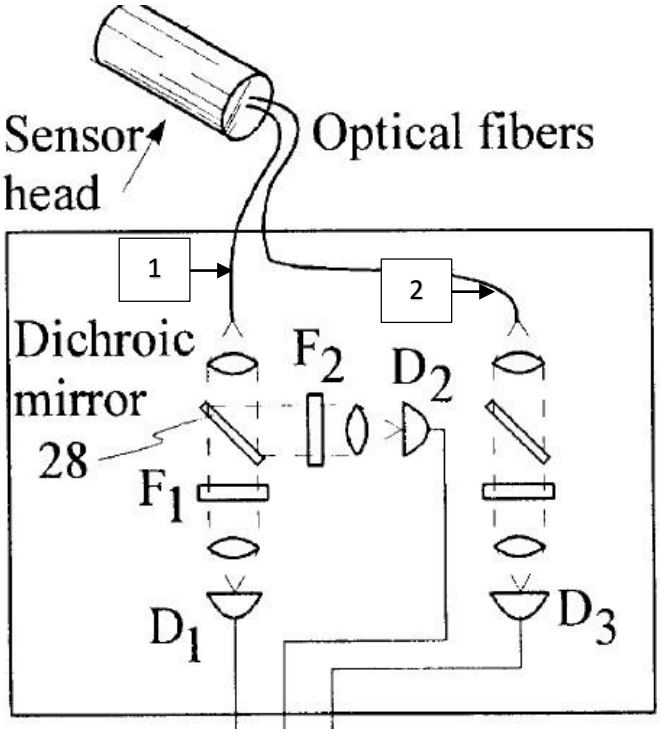

Figure 4-8 Recommended design for temperature measurement in SPS with 3 detectors configuration. [14]

On the other hand, the two optical filtration windows of the Accuraspray are positioned at two different wavelength 785 nm ± 25 and 995 nm ± 25. The first one (785 nm ± 25) is integrating two

atomic argon lines which is typically a non-thermal signal. Therefore, a potential development for that sensor is repositioning this optical window at different wavelength range.

Additionally as illustrated in Figure 3-12, the wavelength range from 950 nm up to 1050 nm is very promising for several reasons. Firstly, the presence of atomic lines start to decrease significantly. Secondly, the thermal radiation peak of *Zr* particles at their melting temperature is around 1 μm which means that repositioning the two optical windows for the pyrometeric system around that wavelength will guarantee more thermal radiation from the particles. The proposed, development is positioning one window around 890 nm, and the other window at longer wavelength 990 nm.

In the same context, the silicon detectors seem to be no longer appropriate for going to that range because of their low sensitivity at the near infrared range. A suggested solution to overcome this problem is using enhanced Silicon pin photodiode with MEMS structure which is manufactured of two different conductive elements to have better sensitivity at the wavelength range 360 nm to 1140 nm. Or, the other proposition is using InGaAs pin photodiode with MEMS structure too which covers a wavelength range from 0.9 μm to 1.6 μm. However, the difference between the detectivity of the two photodetectors should be taken into account in order to assess their capability to collect enough radiation for fast two colors pyrometric sensors.

Finally, it is important to depict the favorable axial distance of detection for diagnostics. The minimum distance of detection should not be less than 4 cm, as below that distance the plasma radiation becomes very intense, and overwhelmingly dominant compared to the thermal radiation coming from the particles which will bias the temperature measurement process. Also for longer distances more than 12 cm, the particles will lose their energy, and they will become relatively cold, therefore, the thermal radiation coming from the particles will not be sufficient for the temperature measurement process.

CONCLUSION

This research introduces a methodology to assess the feasibility for two-color pyrometer in order to calculate the temperature of in-flight particles based on their spectroscopic emissions. This route was found to be challenging because of the presence of non-thermal signal. Moreover, the influence of plasma radiation scattered by in-flight particles on temperature measurement was found to be negligible. Therefore, the main source of error on temperature measurement for in-flight particles is related to the plasma radiation. As introducing the suspension to the plasma volume changes radically the plasma conditions for the reasons depicted earlier.

On the other hand, the current two optical windows used in the Accuraspray are integrating two atomic lines which perturb the temperature measurement because they are considered as basic non-thermal signals. The steep temperature gradient for the particles because of their small sizes as a function of the axial distance introduces a new development chance for the current configuration of the sensor.

If the two colors collected by the temperature sensor are separated with a specific distance (in other words, the signal is detected by the sensor at two focal points separated by a specific distance which is the case for the Accuraspray), this separation leads to a significant error in the temperature measurement process quantified by 380 ° C because the second detected signal will be at a different particle temperature compared to the first one. Therefore, the two color intensities are not taken at the same temperature for the same particles.

Finally, NIR range was scanned at the range of 1100 nm to 2500 nm. The results showed that the gain after introducing the suspension to the plasma jet is not significant. However, further investigations should be carried out at that range while trying different photodetectors.

REFERENCES

1. Fauchais P, Etchart-Salas R, Rat V, Coudert J, Caron N, Wittmann-Ténèze K. Parameters controlling liquid plasma spraying: Solutions, sols, or suspensions. *J Therm Spray Technol*. 2008; 17(1):31-59.

2. Multiphase Flow and Thermal Spray Labatories. Schematic of suspension plasma spray process. http://users.encs.concordia.ca/~dolat/Research-TS-Processes.html#Atmospheric_Plasma_Spray_(APS). Updated 2016.

3. Fauchais PV,Armelle. Solution and suspension plasma spraying of nanostructure coatings. In: Salimi H, ed. *Advanced plasma spray applications.* ; 21 March, 2012:150-188.

4. Fauchais PL, Heberlein JV, Boulos MI. Overview of thermal spray. In: *Thermal spray fundamentals.* Springer; 2014:17-72.

5. Kassner H, Siegert R, Hathiramani D, Vassen R, Stoever D. Application of suspension plasma spraying (SPS) for manufacture of ceramic coatings. *J Therm Spray Technol*. 2008; 17(1):115-123.

6. Fauchais P, Montavon G, Vardelle M, Cedelle J. Developments in direct current plasma spraying. *Surface and Coatings Technology*. 2006; 201(5):1908-1921.

7. Mauer G, Vaßen R, Stöver D. Plasma and particle temperature measurements in thermal spray: Approaches and applications. *J Therm Spray Technol*. 2011; 20(3):391-406.

8. Moreau C, Bisson J, Lima R, Marple B. Diagnostics for advanced materials processing by plasma spraying. *Pure and applied chemistry*. 2005; 77(2):443-462.

9. Vardelle M, Vardelle A, Fauchais P. Spray parameters and particle behavior relationships during plasma spraying. *J Therm Spray Technol*. 1993; 2(1):79-91.

10. Bisson J, Gauthier B, Moreau C. Effect of plasma fluctuations on in-flight particle parameters. *J Therm Spray Technol*. 2003; 12(1):38-43.

11. Gaona M, Lima RS, Marple BR. Influence of particle temperature and velocity on the microstructure and mechanical behaviour of high velocity oxy-fuel (HVOF)-sprayed nanostructured titania coatings. *J Mater Process Technol*. 2008;198(1):426-435.

12. TECNAR. Acuraspray G3C. http://www.tecnar.com/index.php/accuraspray-g3c. Accessed 12/11, 12/11.

13. Mauer G, Vaßen R, Stöver D. Comparison and applications of DPV-2000 and accuraspray-g3 diagnostic systems. *J Therm Spray Technol*. 2007; 16(3):414-424.

14. Fauchais PL, Heberlein JV, Boulos M. *Thermal spray fundamentals: From powder to part.* Springer Science & Business Media; 2014.

15. Bourque G, Lamontagne M, Moreau C. *Method and apparatus for on-line monitoring the temperature and velocity of thermally sprayed particles*. 1999.

16. Oseir. http://www.oseir.com/. Updated 2015. Accessed 3/2015, 2015.

17. Hollis K, Neiser R. Analysis of the nonthermal emission signal present in a molybdenum particle-laden plasma-spray plume. *J Therm Spray Technol*. 1998;7(3):383-391.

18. Salhi Z, Gougeon P, Klein D, Coddet C. Influence of plasma light scattered by in-flight particle on the measured temperature by high speed pyrometry. *Infrared Phys Technol*. 2005;46(5):394-399.

19. McGee TD. *Principles and methods of temperature measurement.* John Wiley & Sons; 1988.

20. Alaruri SD, Bianchini L, Brewington AJ. Emissivity measurements for YSZ thermal barrier coating at high temperatures using a 1.6-μm single-wavelength pyrometer. *Optical Engineering*. 1998; 37(2):683-687.

21. Sakuta T, Boulos MI. Novel approach for particle velocity and size measurement under plasma conditions. *Rev Sci Instrum*. 1988; 59(2):285-291.

22. Hollis K, Neiser R. Analysis of the nonthermal emission signal present in a molybdenum particle-laden plasma-spray plume. *J Therm Spray Technol*. 1998; 7(3):383-391.

23. Gougeon P, Moreau C. In-flight particle surface temperature measurement: Influence of the plasma light scattered by the particles. *J Therm Spray Technol*. 1993; 2(3):229-233.

24. Salhi Z, Guessasma S, Gougeon P, Klein D, Coddet C. Diagnostic of YSZ in-flight particle characteristics under low pressure VPS conditions. *Aerospace science and technology*. 2005; 9(3):203-209.

25. Singhal SC. Solid oxide fuel cells for stationary, mobile, and military applications. *Solid State Ionics*. 2002; 152–153(0):405-410.

26. "PhotonControl". Spectrometers. http://www.photon-control.com/spectroscopy.html. Updated 2015.

27. Hamamatsu. Back-thinned type CCD area image sensor S11071-1106. http://www.hamamatsu.com/us/en/S11071-1106.html. Updated 2015.

28. THORLABS. Adjustable lens tubes. https://www.thorlabs.com/newgrouppage9.cfm?objectgroup_id=4109. Updated 2015.

29.AvaLight-HAL-CAL-mini and DH-CAL calibrated light sources . http://www.avantes.com/products/light-sources/item/947-avalight-hal-cal-mini-dh-cal-calibrated-light-source.

30. Kramida A, Reader J, NIST T. *NIST atomic spectra database* (ver. 5.2). http://physics.nist.gov/asd. Updated 2014. Accessed 4/12, 2014.

31. Workman Jr J, Weyer L. *Practical guide to interpretive near-infrared spectroscopy*. CRC press; 2007.

32. Philip Laven. MiePlot. . 2014.